Università degli Studi di Padova

Dipartimento di Scienze Chimiche

Scuola di Dottorato in Scienze Molecolari

CICLO XXXII

The interaction of biomolecules with gold nanoparticles: from amine-driven binding to covalent capture

Direttore della Scuola: Ch.mo. Prof. Leonard J. Prins

Supervisore: Ch.mo. Prof. Paolo M. Scrimin

Dottorando: Yanchao Lyu

Table of contents

Table of contents

Table of contents

Abbreviations

NMR	Nuclear magnetic resonance
TOAB	Tetraoctylammonium bromide
$NaBH_4$	Sodium borohydride
LSPR	Localised surface plasmon resonance
ESI-MS	Electron spray ionization mass spectrometry
GAP	D-Glucosamine-6-phosphate sodium salt
HR-MS	High resolution mass spectrometry
MS	Mass spectrometry
FT-IR	Fourier-transform infrared spectroscopy
UV-Vis	Ultraviolet-visible spectroscopy
NIR	Near infrared
NPs	Nanoparticles
TEM	Transmission electron microscopy
TGA	Thermal gravimetric analysis
TLC	Thin layer chromatography
DLS	Dynamic light scattering
THF	Tetrahydrofuran
DMAP	4-(Dimethylamino)pyridine
DMF	N,N'-Dimethylformamide
DIPEA	N,N-Diisopropylethylamine
DMSO	Dimethylsulfoxide

Abstract

The aim of this PhD thesis was to study possible ways of interaction between gold nanoparticles (AuNPs) and biological molecules. I have approached this problem in two ways: a) by addressing the interaction of non-functionalized nanoparticles with a molecule through the Au-N "bond" formation; b) by functionalizing AuNPs with proper ligands able to "covalently capture" a target protein.

In spite of the fact that most protein interact with "naked" AuNPs through the amino groups present on their surface, very little is known about the nature of this interaction. The Au-N interaction is much weaker than the most popular Au-S one. Because of this, I have set up experiments aimed at addressing i) how the Au-N interaction correlates with the properties of an amino group (its pKa, level of substitution); ii) the possible mode of bindings of amino groups to the nanoparticles and its dependence on the AuNPs size; iii) the kinetics of these processes. I have used ethanol as the solvent throughout most of my experiments because, being a less competitive solvent than water, it allowed me to more precisely tune the strength of the Au-N interaction. Of course, this choice will require, at a later stage, to check the transferability of the information acquired to the natural biological solvent. The results showed that there is a very good correlation between amine pKa and its affinity to the AuNPs surface and that there are at least three different modes of binding of the amines. They are characterized by quite different kinetics and percentages of amines bound to the gold nanoparticle surface. The Brönsted plots of the logarithm of the apparent affinity constants of the amines for the AuNPs surface vs their pKa were linear with slopes in the -0.4 - -0.6 interval indicating that the same properties that control the interaction of an amine with a proton control also that with the surface Au atoms.

The ability of amines to interact with the AuNPs surface has prompted me to study the interaction of peptides presenting free amines at their termini. Thus, I have discovered that peptide sequences functionalized with primary amines at the N- and C-terminus are able to induce the aggregation of AuNPs in ethanol following their folding into a helical conformation. Random coil peptides are unable to induce such an aggregation process. I have observed that the aggregation can be monitored spectrophotometrically by following the shift of the surface plasmon resonance (SPR) band of the nanoparticles and confirmed

by transmission electron microscopy and dynamic light scattering analyses. Partial denaturation of the peptides results in diminished crosslinking ability. I then examined how the helicity parameter $\theta_{222}/\theta_{208}$ correlates with the shift of the SPR band to longer wavelength and I found a reasonably good linear correlation. All the date I have obtained support the existence of a relationship between the amount of helical content of a peptide sequence and its ability to induce aggregation of the AuNPs. These results have already been published (Y. Lyu, G. Marafon, Á. Martínez, A. Moretto, P. Scrimin, Oligopeptide Helical Conformations Control Gold Nanoparticle Cross-Linking. *Chem. Eur. J.* **2019**, *25*, 11758-11764).

I also have tried to find mild passivating agents, soluble in an aqueous solution, that could be easily replaced by more stable ones in a controlled way. The most obvious choice was to rely on the Au-N bond in view of the expertise I had acquired on the matter. By using glucosamine phosphate (GAP) as a natural and inexpensive passivating agent, quite serendipitously, I discovered that this compound was leading to the formation of nanowires. Indeed, in an aqueous solution devoid of any surfactant, I was able to obtain, under aerobic conditions and substoichiometric nanoparticle passivation (i. e. the concentration of passivating agent is lower than the concentration of surface Au atoms), Au-nanowires of controlled length and reasonably narrow dimensional distribution starting from AuNPs. Since the challenge of obtaining plasmonic nanosystems absorbing light in the near infrared is always open because of the interest that such systems pose in applications such as nanotherapy or nanodiagnostics, I explored more in detail the initial results I had obtained. I discovered that oxygen was required to induce the process and that glucosamine phosphate was oxidized to glucosaminic acid phosphate and H_2O_2 was also produced. I could establish that the process leading to the nanosystems comprises nanoparticles growth, their aggregation into necklace-like aggregates, and the final fusion into nanowires. Control experiments in an anaerobic environment confirmed that the fusion requires the consumption of H_2O_2. I could passivate the nanowires with an organic thiol, lyophilize and resuspend them in water without losing their dimensional and optical properties. By adjusting the length of the nanowires, I could also tune the position of their broad surface plasmon band in the range 630 to >1350 nm. These results, too, have been already published (Á. Martínez, Y. Lyu, F. Mancin, P. Scrimin, Glucosamine Phosphate

Induces AuNPs Aggregation and Fusion into Easily Functionalizable Nanowires, *Nanomaterials* **2019**, *9*, 622).

Finally, I have started investigating the way to functionalize AuNPs with a suitable targeting agent to obtain the "covalent capture" of an enzyme. The strategy requires the preparation of a thiolated molecule featuring an irreversible inhibitor of the target protein. I have selected as my target Urokinase, also called urinary plasminogen activator (uPA or u-PA), a serine protease. Elevated expression levels of urokinase have been found to be correlated with tumor malignancy. This makes urokinase an attractive drug target, and, so, inhibitors have been sought to be used as anticancer agents. Based on published results, concerning the structure of the irreversible inhibitor, I have designed and synthesized the thiolated molecules shown in Fig. I (Ligand 2).

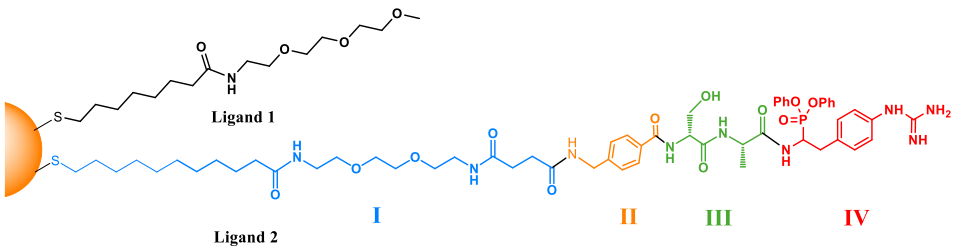

Figure I. Thiolated molecule (Ligand **2**) and solubilizing unit (Ligand **1**) prepared for the covalent capture of uPA with AuNPs.

The chemical structure of Ligand **2** can be divided into four parts: 1) the hydrophilic oligo(ethylene glycol) moiety (blue) bearing thiol, as a water soluble linker to be anchored on the nanoparticles surface; 2) general linker (orange), which acts as a building block for coupling the capture unit; 3) inhibitor unit, which ensures high selectively for the target protein; 4) capture unit that leads to phosphorylation of serine. I have also used Ligand **1** assuming that it should be able, when used to co-passivate the AuNPs to tune their solubility in water and prevent, in a biological fluid, unspecific interactions with plasma proteins. I have synthesized both molecules and fully characterized Ligand **1**. Ligand **2** shows the correct ESI-MS mass but still needs full characterization by ^{1}H- and ^{13}C-NMR. After the completion of the characterization, the functionalized AuNPs will be prepared and the test with uPA will be carried out.

Chapter 1. Introduction

Gold nanoparticles (AuNPs) are in general referred to stable gold colloid, typically less than 200 nm in diameter down to 1 nm, which means the number of gold atoms ranges from hundreds to hundreds of thousands per nanoparticle. At this length scale the surface area to volume ratio, quantum size effect and electrodynamic interactions of the nanomaterials are exceedingly large, which is different from bulk gold materials.[1]

Besides as an object of fascination in enamel and glasses since ancient times, AuNPs have been emerging as an excellent scaffold for the interaction with biological molecules because of their unique chemical and physical properties.[2, 3] To begin with, the well-established synthetic methodology makes the preparation of AuNPs pretty easy and reproducible.[4, 5] In addition, the size, shape, stability, solubility, aggregation state and surface properties of nanoparticles can be precisely modulated,[6] which make AuNPs particularly suitable for targeting biological molecules in various scenarios (Figure 1-1).[7] Second, the high surface to volume ratio endows AuNPs with strong surface chemistry which renders them excellent systems for binding biological molecules.[8] Third, the AuNPs possess intrinsic optoelectronic properties, such as localized surface plasmon resonance (LSPR),[9] fluorescence,[10] conductivity [11] and so on.[3] All of these properties can be influenced by the nanoparticle's size, shape, surface-attached molecules, and local environment. This means they can be employed to amplify the binding-event signal when in the presence of analytes.

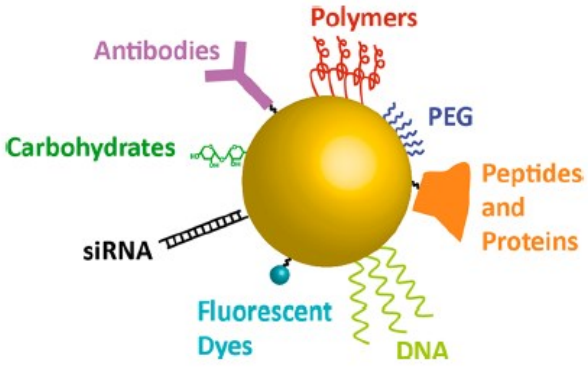

Figure 1-1. The interaction of AuNPs and different passivating agents (Reprinted from A. G. Kanaras *et al*., 2019[7]).

For instance, a monodispersed AuNPs solution (of diameter > ca. 3 nm) typically display a ruby-red color, while the formation of AuNPs aggregates shows a blue color. If this phenomenon is associated with a binding event between the analytes and the gold surfaces, it can be used for analytical purposes. Such detectable response signal is strongly relying on the SPR property.[11, 12] Fourth, the well-developed measuring techniques make the investigation of the nature of binding process between AuNPs and biological molecules much more efficient. Indeed, the effective response of these interaction processes may be not as easily obtained due to the complex molecular structure of the AuNPs surface or the passivating molecules. This requires to carry out the investigation in a rigorous way to make the understanding of the nature of binding behaviour meaningful.

1.1 Preparation methods

Various methods, including chemical reduction method, sonoelectrochemical, physical method and biological method, have been reported for the synthesis of AuNPs in the past 80 years. The most commonly used and simplest method to obtain different shape and size of AuNPs is the reduction of gold(III) salt that yield colloidal gold in an aqueous medium. The size, shape, functionalization and stability of the resulting AuNPs are the result of the use of specific additives as well of physical conditions. A suitable routine for the development of a synthetic protocol, requires the control of key factors such as the reaction medium (water, organic solvent), the category of capping agent (amine, thiol, DNA, protein…), the category of the reducing agent (citrate, $NaBH_4$), temperature, raw material ratio, reaction time. and rate of stirring.

It should be pointed out that freshly prepared, not passivated nanoparticles are not thermodynamically stable due to their small size and large surface area. For this reason, a stabilizing agent to passivate the nanoparticles is required to maintain a stable dispersion for a time long enough to allow their practical application. Surface stabilizing molecules to efficiently cap the nanoparticles should have higher affinity than the solvent for the nanoparticle surface thus preventing their aggregation. This can be done, for instance, by repulsions between nanoparticles due to electrostatic forces.

1.1.1 Turkevich method

One of the earliest methods used for the preparation of colloidal gold is based on the reduction of tetrachloroauric acid by sodium citrate in aqueous solution, which was reported in the textbook *Experiments in Colloid Chemistry* by E. A. Hauser and J. E. Lynn in 1940.[13-15] In this method, they described the formation of gold colloids through the reaction of tetrachloroauric acid and trisodium citrate, where the sodium citrate acts both as a reducing agent and a stabilizing agent to protect the AuNPs from aggregation by providing negative charge to the surface of particles. J. Turkevich and co-workers referred to these results and published the well-known synthetic technique in 1951, which made Turkevich method a landmark for the synthesis of AuNPs. They prospectively built the particles growth model and gave an explanation of the molecular reduction mechanism in their method. Later, the Turkevich method was further refined by G. Frens in 1970s,[16] to produce monodisperse particles with diameters ranging from 5-150 nm operating in an aqueous phase by tuning the ratio of sodium citrate to gold salt. Until today, the synthetic protocols have been further modified but all rely on the original Turkevich-Frens method.

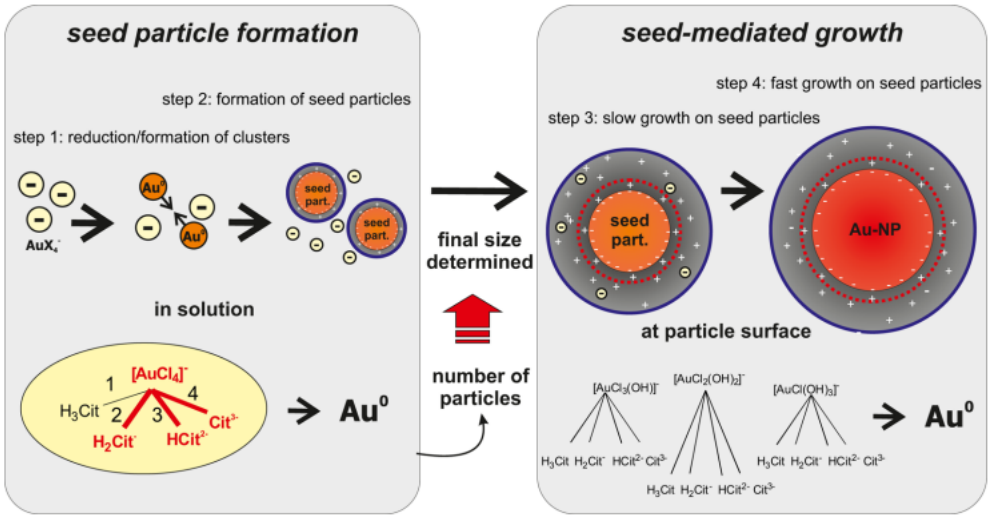

Figure 1-2. Schematic representation of the growth mechanism for gold nanoparticles of the Turkevich method (Reprinted from J. Polte *et al*., 2015[17]).

However, the mechanism of the particles growth process still contains an initial chaotic state due to lack of an effective technique to control it. Recently, J. Polte and co-workers have extensively reviewed an implemented seed-mediated growth mechanism (Figure 1-

2).[15, 17] In their systematic investigation, the particles growth mechanism was dissected into four-steps, which can be applied to a wide range of reaction conditions. In the first step, the gold(III) salt is partially reduced to gold(0) by the reducing agent and forms small gold clusters. In the second one, these small gold clusters continuously grow to evolve into seed particles. The remaining gold(III) ions are then attracted and attached on the electronic double layer (EDL) of the seed particles as co-ions. The final number of particles is determined by the number of seed particles in this step. In the third and fourth step, the rest of gold(III) ions are continuously reduced to gold(0) and grow on the top of the seed particles, first slowly and then fast, with no further particles growth until all the gold precursor is fully consumed.

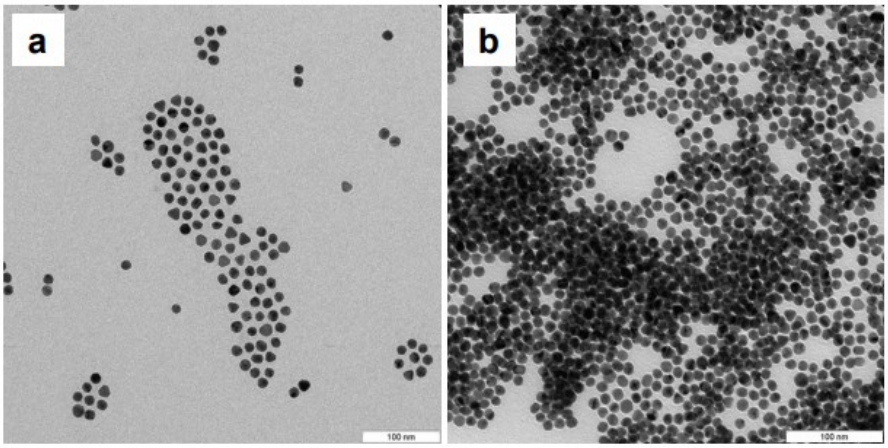

Figure 1-3. TEM images of gold nanoparticles obtained by the Turkevich method in the absence of Ag^+ (a); in the present of Ag^+ (b) (Reprinted from D. Wang *et al*., 2010[18]).

Despite the fact that the pioneering Turkevich-Frens method has been frequently applied, it has several limitations. The prepared AuNPs by the original Turkevich method gives a high ploydispersion in size and the shape of the nanoparticles is not uniform and irregular quasi-spherical and triangular AuNPs are present (Figure 1-3a).[18] This phenomenon is attributed to the growth mechanism during the process of the formation of seed particles without effective control. D. Wang and co-workers [18] modified the method by adding a trace amount of silver nitrate in the reaction mixture to produce highly uniform spherical AuNPs (Figure 1-3b). They suggest the Ag^+ ions play a double role to narrow the particle distribution, as both catalysts of citrate oxidation and as a template to reshape the polycrystalline into a spherical particle. However, this method cannot be applied to the

synthesis of particles with a diameter smaller than 5 nm due to the fact that the reduction of $HAuCl_4$ by citrate is a slow process and only a small part of gold (I) is generated in the first step. However, D. Wang and co-workers [19] more recently reported that they have successfully produced monodispersed nanoparticles with diameter ranging from 2-330 nm. In this improved method, they utilize glutathione (GSH) to accelerate the reduction of gold(III) to gold(I) in a very short time to yield a uniform particle size of 2 nm. The fact that the method is carried out with hot water (> 80 °C) during the particles growth, however, does not fully solve the problem of controlling the nanoparticle size.[20] The addition of a further organic reducing agent has been shown to have the advantage of working at room temperature with an improved control on monodispersity.

1.1.2 Brust−Schiffrin method

The two-phase Brust-Schiffrin method [21, 22] for the synthesis of surface monolayer protected AuNPs is another milestone in the history of nanoparticles preparation method after Turkevich-Frens method (Figure 1-4). When this major breakthrough was published in 1994, it has opened up the road for important applications in the nanomaterials world. The fact that the passivated AuNPs sample can be dried, purified, and redispersed, like an organic compound, in common organic solvent without aggregation undoubtedly constitutes an important advantage in AuNPs manipulation.[23, 24]

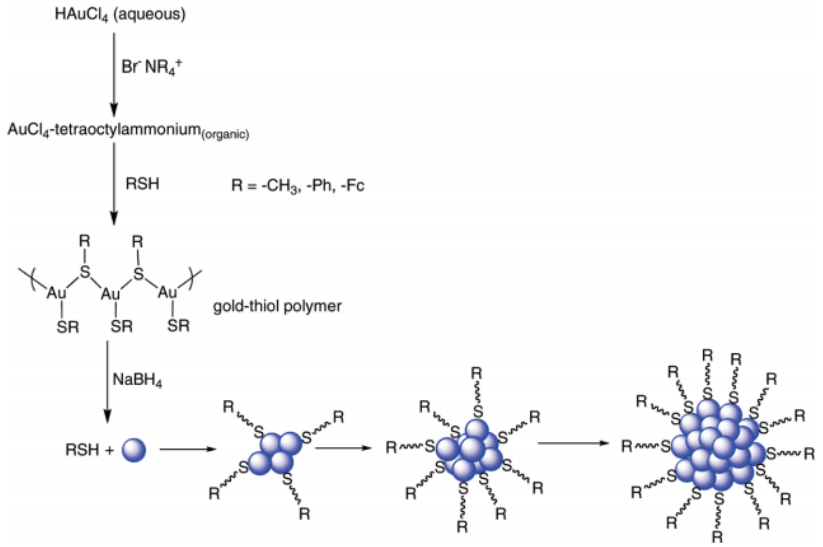

Figure 1-4. Schematic representation of the gold nanoparticles preparation using the Brust-Schiffrin method (Reprinted from R. Murray *et al*., 2009[22]).

Unlike the widely used citrate reduction protocols performed in an aqueous medium, the one devised by Brust-Schiffrin provides extraordinary stability to the AuNPs and gives access to small size (1-5 nm) particles protected by thiol ligands. This is due to the fact that the Au-S interaction is much stronger than the COO-Au.[25] In this two-phase method, the $HAuCl_4$ is first transferred by tetraoctylammonium bromide (TOAB) from an aqueous phase to an organic phase (toluene). Subsequently, a reduction of gold(III) species in the presence of sodium borohydride ($NaBH_4$) and an alkane thiol is performed in the organic phase to yield thiol-protected AuNPs.

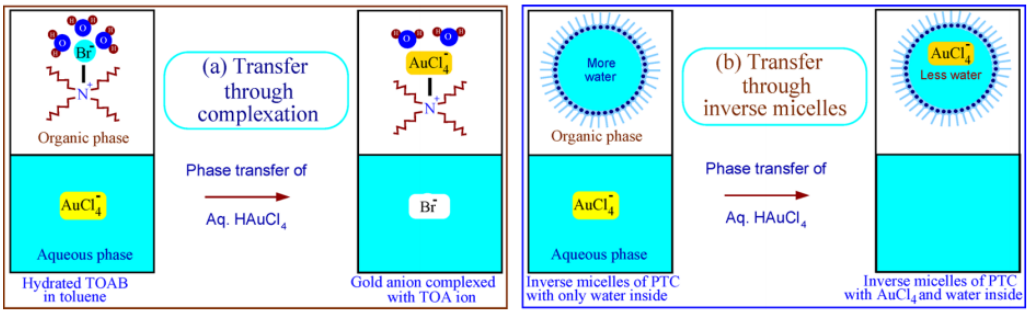

Figure 1-5. Schematic representation of the mechanisms for phase transfer of water-soluble ions into organic phase by TOAB through (a) ion-pair complex formation and, (b) encapsulation of ions in water cores of inverse micelles of TOAB (Reprinted from S. Kumar *et al*, 2013[26]).

What happens in the first step, is still a matter of discussion in the scientific community among those who believe that the TOAB and gold precursor form an ion-pair complex during the phase transfer and those who propose the gold precursor is encapsulated by inverse micelles, which are generated by TOAB with a water core (Figure 1-5).[26] YuYe J. Tong and co-workers [27] concluded, on the bases of an ^1H NMR investigation, that the phase transfer through the inverse micelles mechanism to activate the particles synthesis reaction is the most likely one. However, S. Kumar and co-workers [26] hold a different point of view. They reported that the results of ^1H NMR and Karl-Fischer titrations measurement cannot discriminate between these two mechanisms. They maintain that their results support the ion-pair model bringing in support additional measurements such as interfacial tension and small-angle X-ray scattering. Also the formation of [Au(I)SR]n-like polymers generated by the reduction of gold(III) to gold(I) by addition of alkane thiols was questioned. R. B. Lennox and co-workers [28] have formulated another interpretation. By using ^1H NMR spectra, they have demonstrated that before the addition of the reductant (sodium borohydride), the ion-pair complex formation is $[TOA][AuX_2]$ even in the presence of

thiols, and not [Au(I)SR]n-like polymers. Later, YuYe J. Tong and co-workers [27] supported this hypothesis stating that the Au-sulfur (S) bond is formed after the addition of sodium borohydride (Figure 1-6), when the reduction of gold(I) to gold(0) occurs. Overall, the preparation protocol is carried out under mild conditions. As stated above the Brust-Schiffrin method can be used to produce nanoparticles with diameters ranging from 1 to 5 nm with a narrow size distribution by controlling the ratio of alkanethiol to gold precursors.

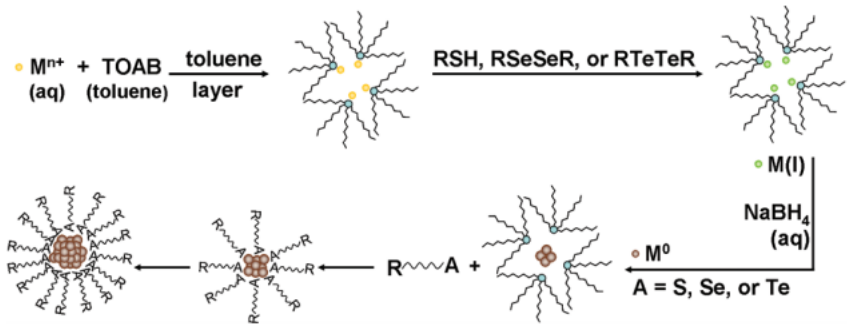

Figure 1-6. Schematic representation of the mechanisms for the formation of Au-S bond by the Brust-Schiffrin Method (Reprinted from YuYe J. Tong *et al*., 2011[27]).

Single-phase synthesis methods [29, 30] have been also studied since the Brust-Schiffrin method has the problem of contamination from the remaining TOAB. The presence of this impurity can affect several applications of AuNPs. To overcome the shortcomings of the two-phase protocol, many groups have suggested water/methanol, THF as solvents to dissolve both the gold precursor and the reducing agent. The mechanism of single-phase method follows the same principles of the two-phase Brust-Schiffrin method. Last but not least, it must be emphasized the the two-phase protocol limts the preparation to AuNPs soluble in non polar solvents.

1.1.3 Peng-Scrimin method

The increasing demand for versatile monolayer-protected AuNPs for applications in biological relevant fields, has spurred the development of procedures requiring less harsh synthesis conditions (leading to the degradation of the functionalized thiol by the strong reducing agents) and leading to water-soluble AuNPs. For instance, Scrimin and co-workers [31] proposed an alternative protocol for the preparation of AuNPs under mild conditions which is still based on the Brust-Schiffrin one (Figure 1-7). In this method, the revised procedure involves two steps, in the first step, $HAuCl_4$ is first transferred by

tetraoctylammonium bromide (TOAB) from the aqueous phase to the organic phase (toluene) with the important addition of dioctylamine. In the second step, the addition of the reducing agent completes the reduction of gold(I) to gold(0). Subsequently, milder reaction conditions are generated by removing the reducing agent and only subsequently the functionalized thiols are added to form the stable thiolated AuNPs. The major difference of this method with respect to the Brust-Schiffrin one is the addition of dioctylamine. It acts as both a reducing agent of gold(III) to gold(I) and stabilizer of the growing cluster before the final addition of the reducing agent ($NaBH_4$) to complete the reduction process. The introduction of dioctylamine leads to two beneficial results, (i) the size of the forming AuNPs can be controlled by tuning the amount of stabilizing agent (dioctylamine); (ii) the thiol-protected AuNPs can be easily obtained by exchanging the dioctylamine, avoiding in this way the exposure of the thiols to harsh conditions. The size of the AuNPs obtained using this method is well controlled by the amount of dioctylamine added and the preparation of water soluble AuNPs is possible through phase transfer, which largely promotes the development of AuNPs.

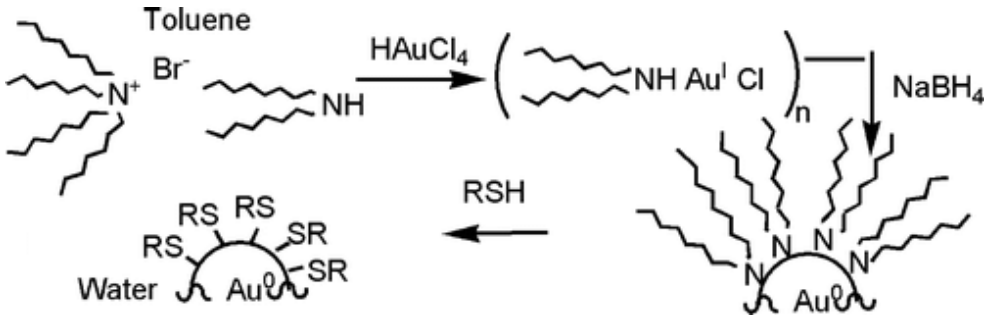

Figure 1-7. Schematic representation of AuNPs preparation using the Scrimin's method (Reprinted from P. Scrimin *et al*., 2008[31]).

1.2 Size-dependent optical properties

1.2.1 Localized surface plasmon resonance (LSPR)

Many examples have been reported of beautiful colors obtained by introducing Au colloids into stained glass to produce church windows, art and crafts. They represent the earliest applications of manmade nanomaterials although the nanostructured nature of these materials was unknow at that time. The first who reported ground-breaking scientific evidence that the beautiful ruby-red color was associated with "fine particles" (today we

know they are the typical AuNPs) has been M. Faraday.[32] However, because of the lack of scientific knowledge, the reason why such finely divided gold produced color remained unsolved during that time. Later, the first theoretical explanation of the red color of the AuNPs in solution was put forward by G. Mie [33] who solved the problem of small spherical particles interacting with an electromagnetic field by using Maxwell's electromagnetic equation in 1908. The author revealed that the ruby-red color displayed by sample solutions could be expected from the light scattering and absorption of the AuNPs. Following G. Mie discovery, many scientists studied these fine particles and eventually made localized surface plasmon resonance (LSPR) known.[34, 35]

From the physical point of view, the surface plasmon phenomenon is related to a collective oscillation of conduction electrons at the surface of metal nanoparticles impinged by the incoming photons (Figure 1-8).[36-38] When the frequency of incoming photons matches the frequency of metal particles surface free electrons, the electric field induces a polarization of the free electrons which oscillate in resonance with respect to the lattice of positive ions, thus for AuNPs, a distinctive absorption peak in the visible range can be observed.[39] In addition, the properties of SPR, such us the peak intensity and position, the ratio of absorption and scattering, are influenced not only by nanoparticles' size, shape but also by aggregates state, as well as the local environment.[5, 40, 41]

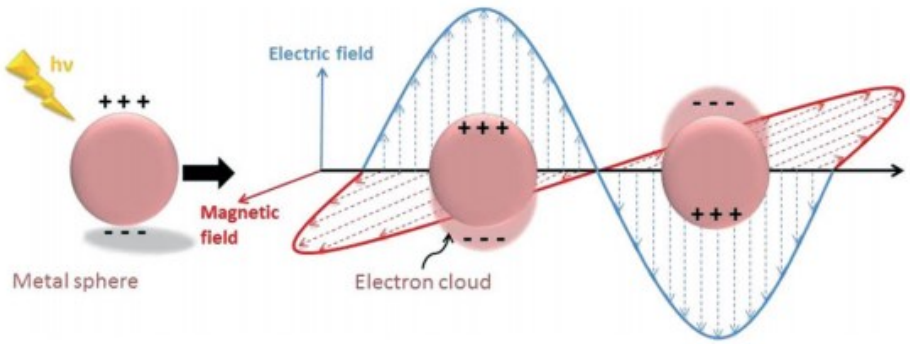

Figure 1-8. Schematic illustration of a localized surface plasmon resonance (Reported from H. Zhu *et al*., 2016[38]).

1.2.2 SPR response to the aggregation of AuNPs

As mentioned previously, the SPR phenomenon in AuNPs, which is responsible for their light extinction properties, is size- and shape-dependent. Accordingly, the position, shape,

and intensity of the SPR band should reflect the AuNPs morphology state. The aggregation of AuNPs into clusters is a well-known phenomenon that can be induced by crosslinking agents.[42, 43] For the aggregation event, AuNPs come into close proximity to adjacent nanoparticles. This induces interparticle surface plasmon coupling, resulting in a significant red-shift from 515 nm to 600 nm and broadening in the SPR band, as well as a visible solution color changing from ruby-red to blue. Therefore, SPR-based probe for the AuNPs bioconjugation is probably one of the most simple, sensitive yet reliable analytical tool.[44] This approach features several advantages. Firstly, the absorption spectrum of AuNPs in an aggregate state can provide information concerning the increase of the average size, ascribed to AuNPs agglomeration, the change of AuNPs morphology from monodispersed spherical to various aggregate forms. K. Ariga and co-workers [45] described that the different optical response of aggregated AuNPs can provide information on the formation of packed (almost spherical) or chain-like aggregates through theoretical and experimental perspectives. The experimental and simulation results revealed that the adsorption spectra for either highly dispersed AuNPs or globular aggregates (Figure 1-9) only exhibit one distinct peak in the visible wavelength range 450-800 nm. Linear aggregates (or linked AuNPs pairs), on the contrary, show two peaks in the same region. The intensity and positions of the band(s) are dependent on the degree of aggregation. In other words, the property of the SPR band(s) is determined by the aggregate size.

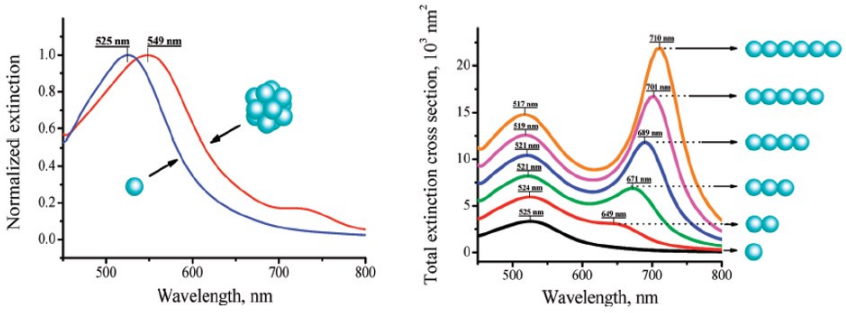

Figure 1-9. Schematic representation of the optical properties of the different aggregates formed (Reprinted from K. Ariga *et al*., 2012[45]).

For the linear aggregates, as depicted in the Figure 1-9, the first peak was observed at a wavelength close to the adsorption peak of isolated AuNPs. This is ascribed to the quadrupole plasmon excitation in coupled spheres, while the second peak located at longer wavelength is due to the dipole plasmon resonance of AuNPs. A. Gedanken and co-workers have also investigated the plasmonic coupling of AuNPs pairs by simulations and

experiments.[46] In their investigation, they mainly focused on the frequency and position of plasmon band as a function of the distance between the AuNPs. The results indicated that as the interparticle spacing decreases, the intensity of first peak becomes weaker while the second peak shifts to longer wavelengths and shows higher absorption intensity (Figure 1-10). The maximum peak shift is observed when the interparticle distance approaches zero, at which point the electrodynamic interaction between the nanoparticles is at a maximum.

Secondly, both the operating and processing are simple and can be performed with a UV-visible spectrometer and even with the naked eye. Because of the absorption peaks for both globular and linear aggregates are red-shifted with respect to the peak of an unaggregated system this is accompanied, as said above, by significant color changes of solutions. This implies that the optical response of an aggregated AuNPs can not only provide detailed information on aggregates morphology but also endow the AuNPs with the ability to detect cross-linking analytes as colorimetric sensing probes.[47-49] Last but not least, the size of the AuNPs can be easily tuned to explore various binding modes with selected biomolecules. This opens the road for the design of proper functional groups to target biomolecules and follow the process via AuNPs aggregate formation. For the above reasons, the SPR response of the aggregates of AuNP is the strategy choice for analysing the interaction of biomolecules and AuNPs. The process will be discussed in more detail in a subsequent section.

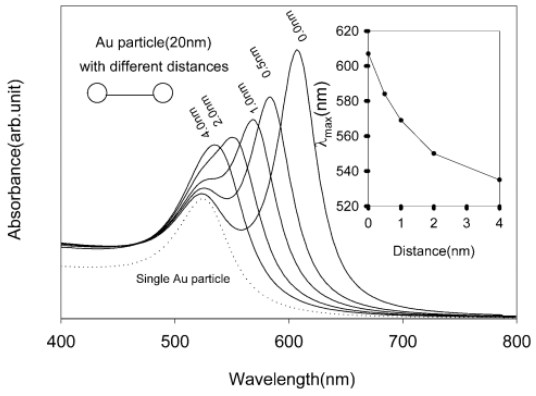

Figure 1-10. Schematic representation of the interparticle distance control of plasmonic coupling and its effect on the band position and intensity (Reprinted from A. Gedanken *et al*., 2004[46]).

1.2.3 Fluorescence quenching

Fluorescence quenching is another common phenomenon for AuNPs-based fluorescence sensing applications when fluorophores are attached onto the AuNPs surface. Metallic nanoparticles like AuNPs are typically high efficient fluorophore quenchers due to their extraordinary high molar extinction coefficients and broad energy bandwidth.[50-52] In addition, fluorescence resonance energy transfer (FRET) is widely used in the sensing application, which is a nonradiative process whereby an excited fluorophore donor transfers energy to an organic/inorganic acceptor in the ground state through long-range dipole-dipole interactions.[53] AuNPs are intensively exploited as FRET acceptor considering the above reasons. The rate of energy transfer is critically dependent on the distance between the donor and acceptor. Besides the standard FRET considerations, the overlap of the fluorophore's emission with the nanoparticle's absorption spectrum renders the FRET process strongly size- and shape- of AuNPs dependent.[54] Furthermore, the quenching event can also be attributed to photoinduced electron transfer (PET) from fluorophores to nanoparticles, thus the quenching efficiency can be modulated by charging/discharging the AuNPs.[55, 56] Therefore, whatever for FRET-based or PET-based quenching strategies, the fluorescence of a donor (usually is the fluorophore) will be quenched when linked to AuNPs. When the analyte, such as an amine-based small molecule, an amino acid, a peptide or a protein, binds to the AuNPs surface, it replaces the AuNPs-bound fluorophore releasing it into the bulk medium restoring totally or partially its original fluorescence. Accordingly, the fluorescence intensity can be used as a reference parameter to quantify the analyte. Taking advantage of the fast and sensitive response of this strategy, AuNPs-based fluorescence quenching assays, not only provide a wealth of information for studying molecular recognition but also further expand the scope of applications in the field of affinity of biomolecules to AuNPs.

On the basis of the above discussion, the fluorescence quenching ability of the AuNPs provides the basis for the design of an indicator-displacement assay (IDA).[57-60] The IDA is a popular technique for monitoring host-guest binding event, determining binding constant, and of course sensing and discriminating various types of molecules. Unlike the traditional chemosensors in which the indicator is attached by an irreversible covalent bond, the

indicator in the IDA is connected to a host via a reversible interaction leading to a quantitative fluorometric determination of its concentration (Figure 1-11). Taking advantage of this strategy, many sensing systems have been developed for studying the interactions of biomolecules, such as amino acids and proteins.[61]

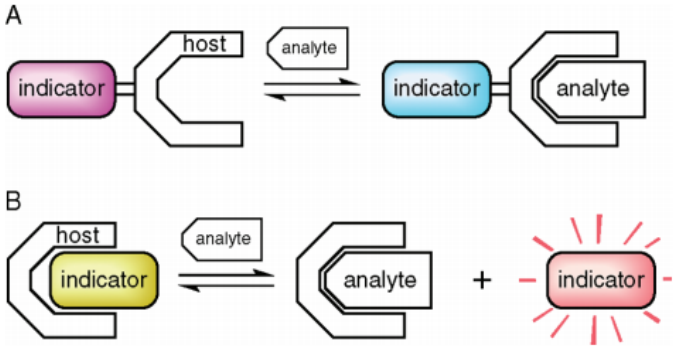

Figure 1-11. Schematic representation of the mechanism of indicator displacement assay (Reprinted from V. Anslyn *et al*., 2010[57]).

1.3 AuNPs crosslinking aggregation by functional biomolecules

Crosslinking aggregation of AuNPs as a simple yet reliable analytical strategy for detecting binding events, useful for studying and analyzing specific biomolecules adsorbed to AuNPs, has attracted increasing interest in present days.[62, 63] Using biomacromolecules or small biomolecules bearing functional groups as AuNPs cross-linkers, can be a more efficient method to control and design the interparticle properties and the geometrical structure of Au clusters.[64-67]

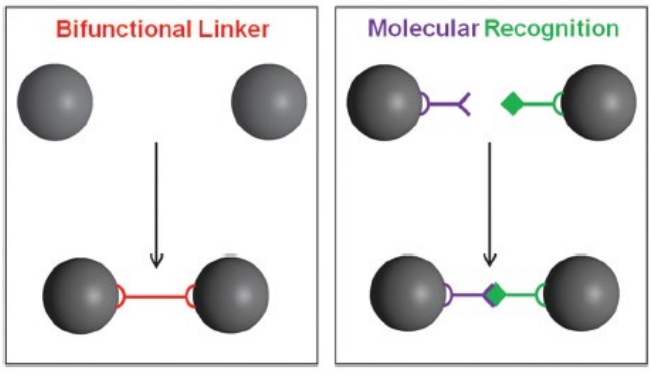

Figure 1-12. Schematic description of the two main different classes of molecular linkers (Reprinted from D. Graham *et al*., 2012[68]).

According to the mechanism of interaction, in this case, the molecular linkers could be classified into two major categories: i) Bifunctional molecular linkers able to interact directly with the AuNPs surface. The expression "molecular linkers" refers to small molecules or oligomers (usually less than 2 nm in length) that are comprised of at least two binding sites placed at opposite ends of the molecules, respectively, each capable to attach to an Au surface by chemisorption to form a strong or weak bond, such as dithiol, diamine. ii) Molecules as bridge or with selective recognition ability. In this scenario, AuNPs surfaces are usually engineered with functional units endowed with the ability of interacting with other functional groups (hydroxyl, carboxyl, amine) present on the molecular bridge through hydrogen bonding or coordination of transition metal (Figure 1-12).[68]

Recently, biomolecules-triggered aggregation of AuNPs is also rapidly receiving intensive attraction as a promising strategy for studying the catalytic activity of enzymes as a mean to control the aggregation state of AuNPs.[69, 70] For instance, DNA-, protein- or peptide-functionalized nanoparticles aggregates are particularly useful systems since triggered changes in their aggregation state may be readily monitored following the solution color change from blue to red. Due to such properties, AuNPs aggregates system would allow, in principle, to use any molecular anchor as a bioresponsive nanomaterials.

1.3.1 Biomolecular linker-mediated aggregation of AuNPs

As discussed above, the crosslinking of AuNPs driven by interparticle and thermodynamic forces [71-74] may lead to the formation of ordered or unordered nanostructures. The use of a proper linker, however, may lead to a better control of the aggregate formed even using a very small amount of it. Concerning the study of molecules that crosslink the AuNPs via direct interaction with the gold surface, the choice of suitable functional groups is rather limited. So far, the most common choice has been a dithiol, which can bind AuNPs with a strong covalent bond.[75-77] One of the earliest work in this context was reported by Brust and co-workers (Figure 1-13).[78] They utilized alkyl dithiols to functionalize the AuNPs instead of monothiols. The results of TEM revealed that superclusters were formed. Several evidences indicated that these features can be

interpreted as a process initiated by the crosslinking between AuNPs mediated by the short chain dithiol followed by the collapse of the cluster to inglobate more AuNPs.

A. Gedanken and co-workers [46] have shown that the crosslinking of spherical AuNPs with dithiol crosslinkers can be regulated or "tuned" by pH and, to some extent, by tuning the length of the dithiol linkers. D. Vaknin and co-workers [79] reported that a nanostructure was obtained by AuNPs aggregation in the presence of short dithiol ligands. In his investigation, the interparticle distance can be controlled by increasing the length of the dithiol linker (Figure 1-14).

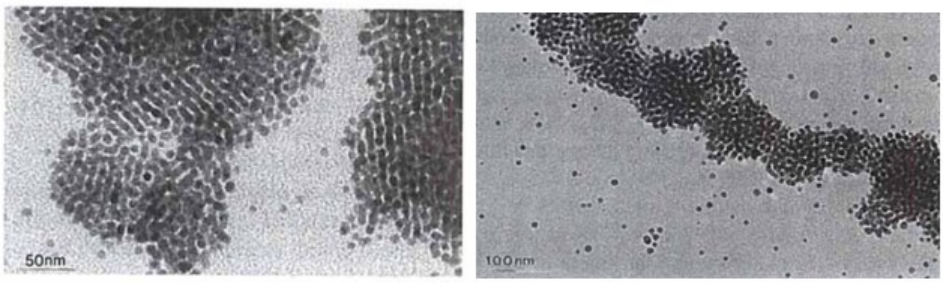

Figure 1-13. TEM micrograph of AuNPs cross-linked with 1,9-nonanedithiol by Brust (Reprinted from Brust *et al*., 1995[78]).

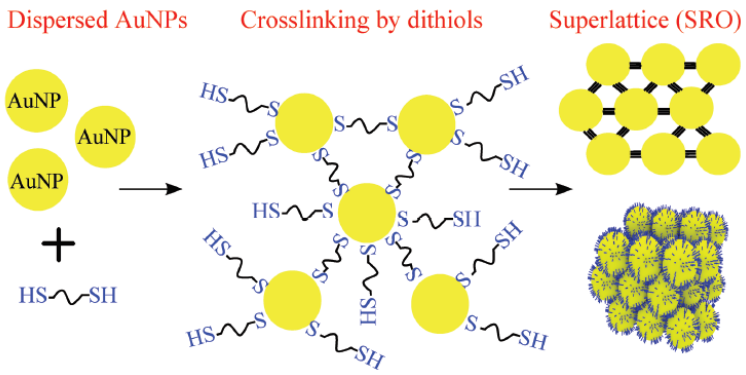

Figure 1-14. Scheme of the process leading to the obtainment AuNP-dithiol aggregates (Reprinted from D. Vaknin *et al*., 2018[79]).

Another different crosslinking strategy is based on the oxidative coupling of monothiols anchored on the nanoparticles surface. Based on this principle, B. Vercelli and co-workers reported a crosslinking system, where the AuNPs were functionalized with pyrrolethiol or thiophenethiol.[80] This enables the coupling between the neighbouring AuNPs, when the thiol-capped AuNPs are treated with both reductive and oxidative capacitance-voltage. Following the redox reaction, the monolayers are irreversibly oxidized and form a molecule

bridge resulting in the plasmonic coupling (Figure 1-15). It can be speculated that the irreversible crosslinking process limits the versatility of the approach reducing the scope of the application.

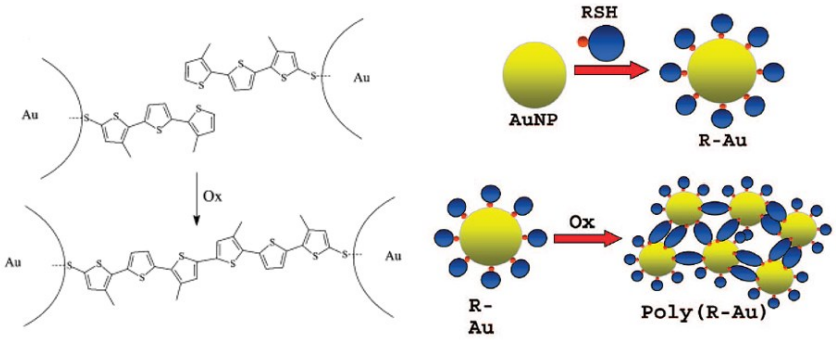

Figure 1-15. Schematic representation of the mechanism of indicator displacement assay (Reprinted from B. Vercelli *et al*., 2008[80]).

Many evidences demonstrate that the process of reversible aggregation is more difficult to obtain due to the fact that aggregated nanoparticles have the tendency to collapse to larger, insoluble materials.[81, 82] Reversible crosslinking, however, has huge potential for producing bioresponsive nanomaterials. On the basis of this consideration, our group has developed a reversible crosslinking protocol (Figure 1-16).[83] In this method, the colloidal nanoparticles were firstly treated with a dithiol which featured two ester bonds, whereby a transformation from monodispersed AuNPs to aggregates was observed. Afterwards, the deaggregation process can be realized by breaking the tethers with hydrazine, which is capable of cleaving the ester bonds of the dithiol. Further addition of the dithiol induces the aggregation again. The strategy of molecule-responsive control of reversibility, indeed, can be applied to the sensing of very specific and, most important, effective cleaving agents such as biological catalysts.

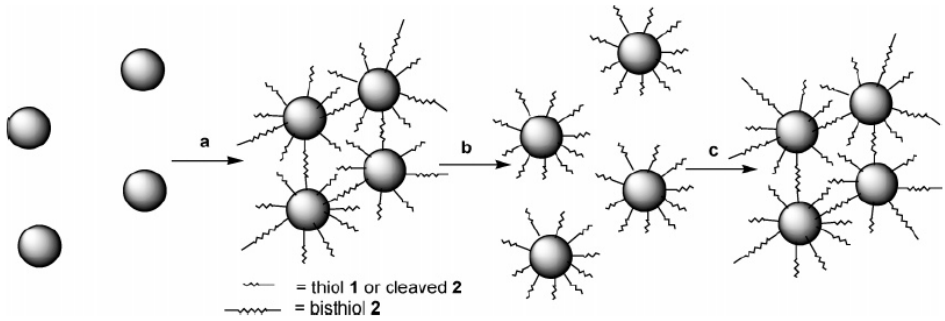

Figure 1-16. Schematic representation of the aggregation/deaggregation processes (Reprinted from P. Scrimin *et al*., 2005[83]).

Recently, this idea has been applied by exploiting the catalytic action of enzymes to control the aggregation state of AuNPs. The biomolecules trigger the dispersion of AuNPs aggregates (Figure 1-17). In a recently reported study,[84] the group has designed two C- and N-terminal cysteinyl derivatives of peptide substrates specific to thrombin and lethal factor. In this strategy, the dithiol peptides were first treated with the specific protease. Subsequently, the solution was incubated with citrate stabilized AuNPs. Interparticle aggregation occurred (with resulting color change) only by the intact peptides (i.e. in the absence of target proteases). On the contrary, the protease-cleaved peptides were not able to bridge the AuNPs. In this case no color change was observed making the detection of proteases possible. This nanoparticle-based assay does not require nanoparticles functionalization or any specific instrumentation to implement for the qualitative detection of proteases. Later, M. Stevens and co-workers [85] further described a simpler approach to protease-responsive AuNPs (Figure 1-18). In their study, Fmoc-protected peptides that bear a cysteine anchor, were used to passivate AuNPs and monitor a protease-responsive event. The crosslinking occurred by control of Fmoc groups that can interact with each other through π-stacking. Then when thermolysin, which can specially catalyse the cleavage of the amide bond of peptides, was added to the system, the peptide ligands could be cleaved and lead to AuNPs dispersion in the solution along with a blue to red color change.

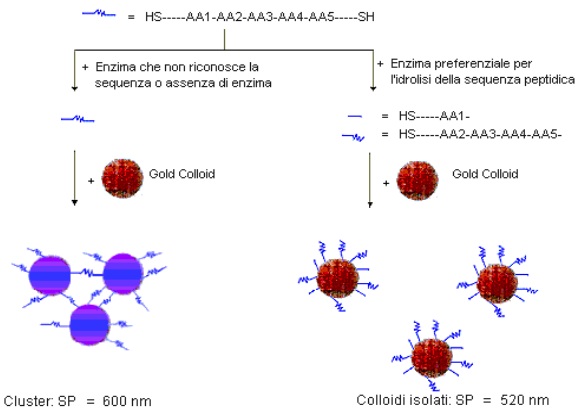

Figure 1-17. Schematic representation of the protease-triggered NPs dispersion approach (Reprinted from P. Scrimin *et al*., 2006[84]).

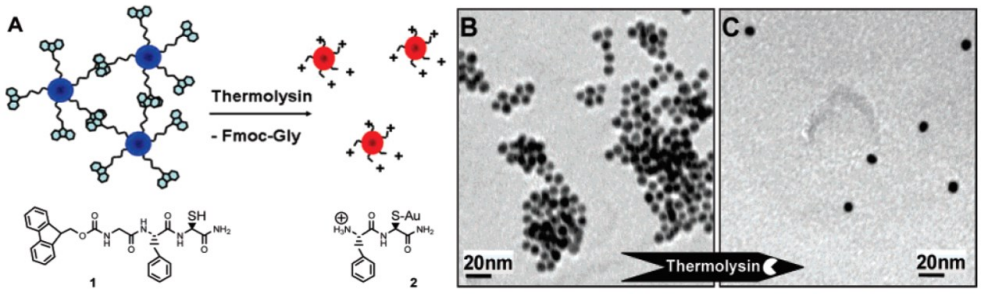

Figure 1-18. Schematic representation of the protease-triggered NPs dispersion approach (Reprinted from M. Stevens *et al*., 2007[85]).

The tendency of molecules bearing amine and carboxyl groups to bind and induce interparticle aggregation is an attractive and important topic because the amines and carboxylate exist in biological molecules like amino acids, oligopeptides and the surface of proteins.[86, 87] Therefore, the exploration of the cooperative behaviour of amines and carboxylate in binding to AuNPs makes the investigation of biomolecules interaction to AuNPs very interesting. It is well known that monoamine-containing molecules can bind and stabilized AuNPs through the weak Au-N interaction, which has been reported in the literatures.[88-90] By introducing at both ends of short spacers two of these functional groups aggregation of the AuNPs can be induced. This is of great interest for the induction of an amino acid-, and peptide-linked aggregation/deaggregation process. To demonstrate this point, the interaction of AuNPs with biomolecules featuring different length scale of diamines and ploy-amines were systematically studied.

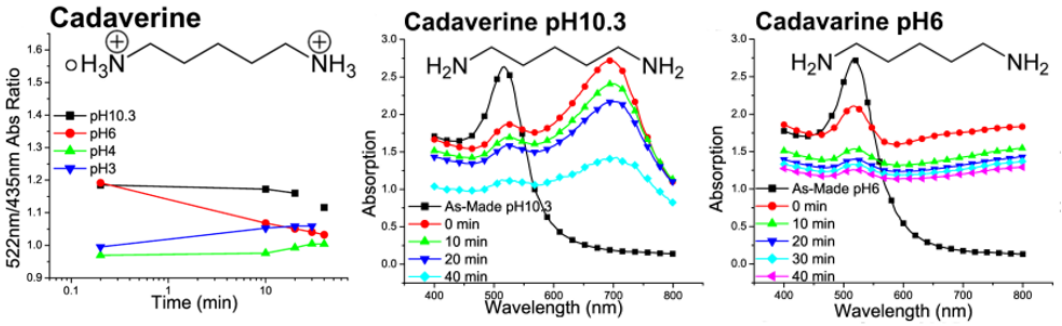

Figure 1-19. Schematic representation of the aggregation of AuNPs induced by diamine in different pH values (Reprinted from M. E. Reeves *et al*., 2013[87]).

In the first example, cadaverine bearing amine groups on opposing ends of the molecule was added to the AuNPs solution (Figure 1-19),[87] a color change was observed, indicating the binding event had occurred with the AuNPs leading to aggregation. This happens because cadaverine acts as an interparticle bridge binding two adjacent nanoparticles

through the attachment of its two primary amines. What is more interesting, the aggregation occurs at all pH values, although at a different extent. For instance, the decrease in the 522 nm/435 nm absorbance ratio at acidic pH suggests that the process of amine-induced aggregation is less efficient under these conditions. In addition, the ability to sensitively and selectively crosslink "naked" AuNPs with spermine in urine was also confirmed by P. Campíns-Falco and co-workers (Figure1-20).[91] It is noteworthy that putrescine hardly affect the position of SPR band, an indication that the conformation in solution of the two molecules that differ for a single carbon in the spacer between the two NH_2 plays a relevant role. It can be speculated that putrescine is more likely to bind to the same AuNPs.

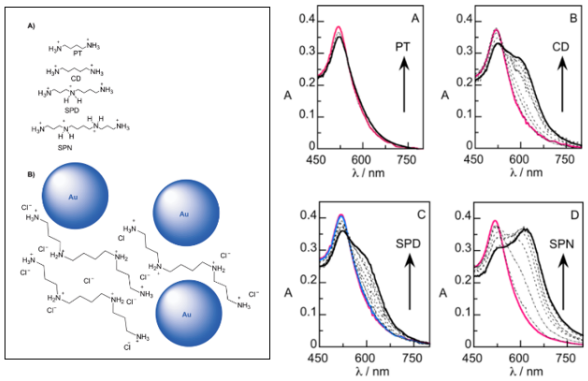

Figure 1-20. (Left) chemical structure of the polyamines used. (Right) AuNPs aggregation approach (Reprinted from J. P. Prieto *et al*., 2014[91]).

Since the plasmonic coupling phenomenon is highly dependent on interparticle distance, a SPR-based colorimetric sensor can also be designed by modulating the space between the pairs of AuNPs. P. Kuo and co-workers [92] reported a series of poly(oxypropylene)diamines to control the AuNPs aggregation (Figure 1-21). In their study, the AuNPs were treated with different chain length crosslinkers. They found that the plasmonic coupling becomes stronger with the decrease in the linker length. Following a different approach, B. Liedberg and co-workers [93] reported a reversible crosslinking process of polypeptide functionalized AuNPs using the polypeptide as a linker (Figure 1-22). Aggregates occurred when the peptides folded into two disulphide-linked four-helix bundles. When the disulphide, which is a linker-controlling unit by regulating the formation of the four-helix bundle, was reduced by tris(2-carboxyethyl)phosphine (TCEP) the redispersion of the aggregates particles easily occurred. Taken together, these reports on

the linker-mediated AuNPs crosslinking reveal that both the molecular structure and chain length play a crucial role in the plasmonic coupling process.

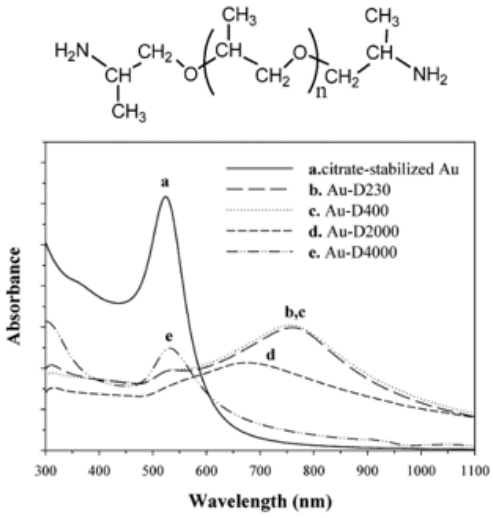

Figure 1-21. Absorption spectra of the citrate-stabilized AuNPs and treated with different ligands (Reprinted from P. L. Kuo *et al*., 2005[92]).

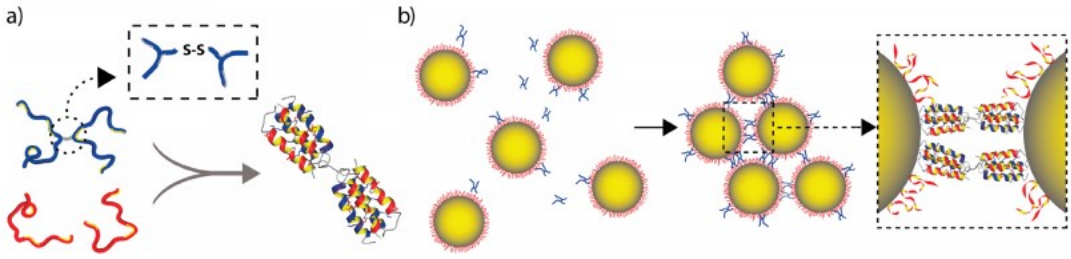

Figure 1-22. Schematic illustration of the aggregation/deaggregation of peptide-coated AuNPs induced by the ordered/unordered formation of crosslinker (Reprinted from B. Liedberg *et al*., 2008[93]).

Besides the examples mentioned above, there are other biomolecules that have been considered for connecting the AuNPs. It is well known that all amino acids are comprised of a primary amine, a carboxylic acid, and a side chain bearing or not other functionalities able to interact with the surface of AuNPs. In the absence of such functionalities the side chain is generally considered to be inert to gold binding, therefore in the interaction with AuNPs only carboxyl and amine groups are at play.

On the contrary when such functionalities do exist, they may be involved in crosslinking processes. For instance, T. Li and co-workers [94] studied the formation of small peptides (two amino acid)-linked aggregates of AuNPs (Figure 1-23). In their investigation, L-lysine

was firstly attached on the AuNPs surface by the Au-N bond between the ε-amino group of L-lysine and the AuNPs at a pH of 10.69, leading to no significant aggregation. This implies that the terminal carboxylate on lysine prevents aggregation at high pH value, which was also confirmed by M. E. Reeves [87] who studied the crosslinking ability of molecules terminated by two carboxyl groups at various pH environments. In their study, they found that crosslinking ability of carboxyl groups is strongly pH dependent and amino acids are able to bridge AuNPs through zwitterionic electrostatic interactions at low pH values. The effect of the shielding amino acid is therefore providing an interesting scenario for the scientific community. For instance, in Li's study,[94] they added a condensing agent (EDC) to the lysine-coated AuNPs. The dipeptides formed by condensation between the amino group and carboxyl group of another lysine acted as linker molecules resulting in a three-dimensional AuNPs network. Nicely enough, K. Assaf and co-workers [95] have reported that the AuNPs can be used to readily monitor amino acid decarboxylase activity (Figure 1-24). Under the experimental conditions used for the experiment, amino acids, such as lysine and histidine, did not cause any aggregation. Once the carboxylate group, however, was eliminated by decarboxylases, the produced diamines can trigger AuNPs aggregation, leading to a significant color change.

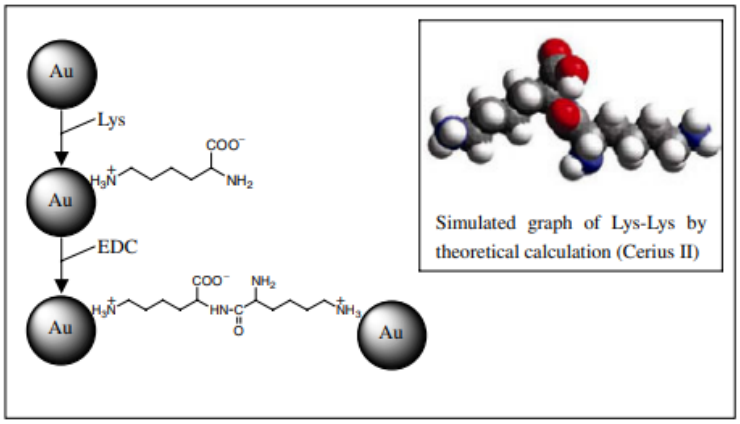

Figure 1-23. Schematic representation for the formation of dipeptide between AuNPs (Reprinted from T. Li *et al*., 2002[94]).

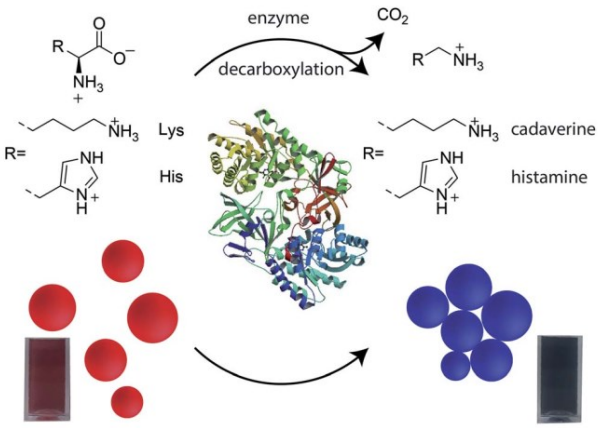

Figure 1-24. Assay principle illustrating the colorimetric response of AuNPs in the course of the enzymatic decarboxylation reaction (Reprinted from K. I. Assaf *et al*., 2017[95]).

1.3.2 Molecular bridges controlling the aggregation of AuNPs

Recently, a novel type of binding system is also receiving considerable attention as a promising strategy for studying the biological activity. The approach relies for linking the AuNPs, on host-guest chemistry [96] and molecular recognition [97] and is distinct from the traditional crosslinking processes discussed so far and characterised by some important features. The major advantage of this approach is the versatility. AuNPs can be easily functionalized by tuning the structure of the coating ligands (host), thus making the tailored design of the proper receptor for binding various analytes possible. A host-guest system was employed in the crosslinking of AuNPs by H. Chen and co-workers (Figure 1-25).[98] They studied diamine oxidase activity with AuNPs coated with *p*-sulfonatocalix[6]arene. The UV-visible spectrum revealed that 1,6-hexane diamine as a guest molecule can bind to two *p*-sulfonatocalix[6]arene of different AuNPs leading to the formation of aggregates. In the presence of diamine oxidase, the crosslinking is, on the contrary, prevented. In this case, this supramolecular binding system can be used in the monitoring of enzyme activity.

Another different crosslinking strategy is based on the hydrogen bonding or coordination of a transition metal by a linker bearing hydroxyl groups. For example, when dopamine, which is known to have a high affinity for binding to AuNPs, was added to the system, it can act as a molecular bridge for pairs of AuNPs (Figure 1-26), leading to their aggregation via hydrogen bonding interactions.[99] On the other hand, the crosslinking can also be performed by introducing Cu^{2+} ions into the dopamine-coated AuNPs solution.[100]

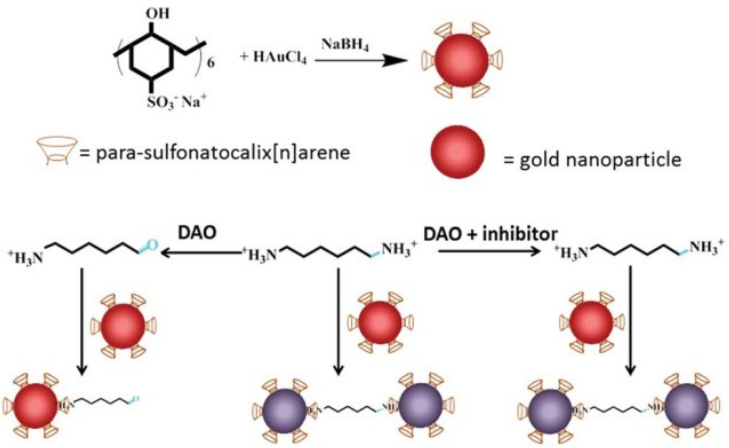

Figure 1-25. Schematic presentation of the detection of Diamine oxidase and its inhibitor (Reprinted from H. Chen *et al*., 2017[98]).

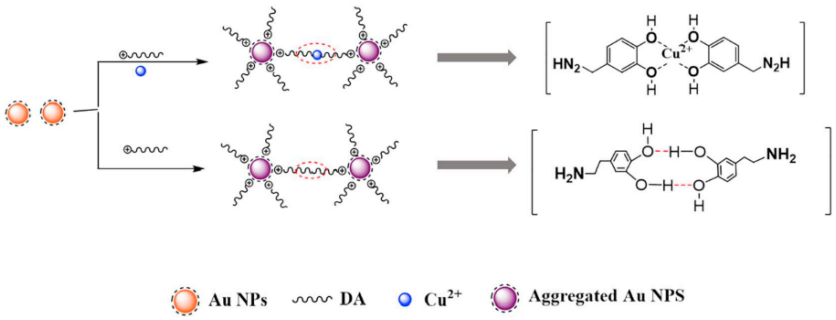

Figure 1-26. The mechanism for the colorimetric determination of dopamine (Reprinted from J. Di *et al*., 2019[99]).

1.4 Affinity of biomolecules for AuNPs

It is generally accepted that the interaction of AuNPs with biomolecules is influenced by various factors as mentioned above. However, the strength of this binding affinity is often overlooked, yet integral part of all strategies because of all the binding event, such as crosslinking aggregates, ligand exchange,[101] and protein "corona",[102] are at the basis of the specific binding of the biomolecules on the surface of AuNPs. It is well known that the surface of AuNPs is imperfect and characterized by flat regions and edges, and these different regions can interact with molecules in different ways.[103-105] These binding sites, indeed, typically show different electron densities and steric properties, leading to different chemical affinity. It has been also reported that the ratio of these different regions can be modulated by changing the AuNPs dimensions whereby controlling the binding affinity.[103] Of course, there are other aspects to be considered to govern the binding strength, such as

the ligand structure, the local environment, and acidity/basicity. For this reason, understanding the binding principles of molecules to the AuNPs surface is becoming very important for understanding and tuning their interaction with biomolecules for several applications. Recently, approaches taking advantage of techniques, such as fluorescence spectroscopy, FT-IR, XPS have been reported.

1.4.1 The binding of ligands and the effect of multivalency

For surface modification of the AuNPs, to create an organic monolayer on their surface, as mentioned previously, one of the preferred choices is constituted by organic thiol derivatives featuring different kinds of functional groups to enhance AuNPs stability, functionality, and target specificity.[106] To introduce novel functionalities or produce mixed-monolayer AuNPs, exchange of thiol ligands on the Au surface is a simple and widely exploited way which was first pursued by Murray and co-workers.[107] This strategy has been extensively used to obtain AuNPs with a controlled composition of different thiols (mixed monolayer). However, the results are often disappointing because the exchange efficiency (resulting from binding affinity and/or kinetic of exchange) is still not fully understood. Obviously being able to master it would result in the obtainment of novel nanomaterials, and would also unveil the affinity of different thiols to the AuNPs surface. Obviously, the interaction is not limited to thiols, because, as it has been shown above, other functional groups, like amines, for instance, are able to conjugate organic molecules to the AuNPs surface. Consequently, studying the ligand binding affinity to the AuNPs surface constitutes an important prerequisite for the design of novel, functionalized AuNPs. It may also provide clues in understanding the interaction of proteins with AuNPs, a process that leads to the formation to the protein "corona" whenever an AuNPs is dispersed in a biological fluid.

To address this problem, one of the earliest works in this context was reported by F. Zerbetto and co-workers [108] who proposed a simple and reliable method to study the kinetics of place-exchange reactions of thiols (Figure 1-27). In their study, the concept is monitoring the release of a fluorescence indicator bound to the AuNPs surface when a competitor (like decanethiol) is added. The protocol is a simple fluorescence indicator displacement assay as described previously. Firstly, the AuNPs were functionalized with a

thiol linked to a pyrene moiety, thus the quenching of pyrene by the AuNPs was observed. Subsequently, by adding increasing concentrations of decanethiol, the thiol bearing the pyrene moiety was displaced from the AuNPs surface leading to fluorescence enhancement. The results of the kinetic studies and simulation experiments revealed that the recovery of fluorescence is time dependent with a bimodal profile which is consistent with Au surface inhomogeneity.

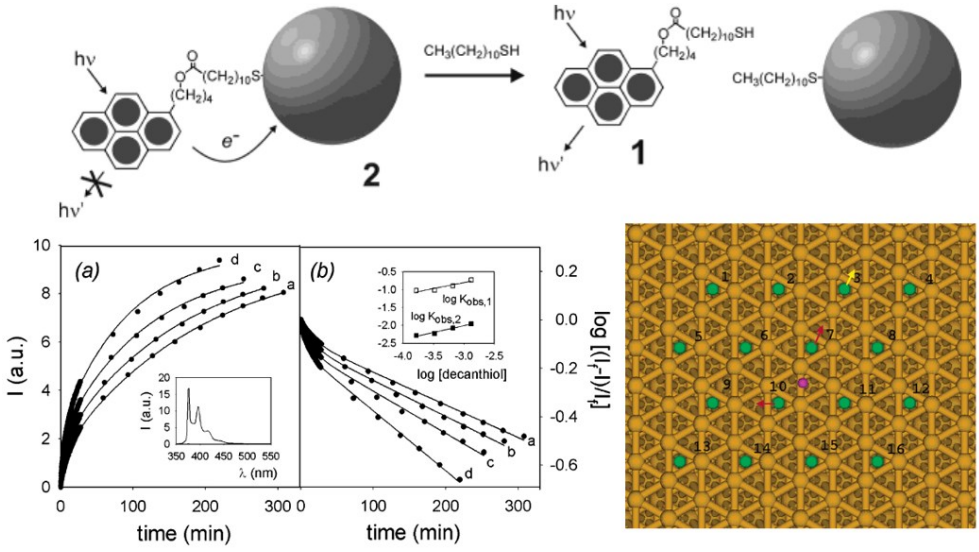

Figure 1-27. The IDA approach and theoretical simulation for the investigation of binding affinity (Reprinted from F. Zerbetto *et al*., 2003[108]).

If the molecule used for the binding to AuNPs surface bears several functionalities it is called multivalent. A multivalent interaction is generally characterized by a larger affinity than a single one. C. Graf and co-workers [109] studied the effect of multivalent ligands on binding affinity to AuNPs (Figure 1-28). Multidentate ligands have been utilized to stabilize the AuNPs and enhance particles stability in solution against aggregation with a better performance compared to that of monovalent ligands. As expected, contrary to the monovalent ligands, the multivalent ones display higher affinity to the AuNPs surface through multivalent interactions. These very multiple interactions do exist in peptides and proteins. In their study, they found that the dye-functionalized ligand can be fully exchanged by mono-, di-, and trivalent thiol ligands. Interestingly, a systematic investigation of the kinetics of the ligand exchange reactions of mono- and multivalent ligands on different-sized AuNPs revealed a significant enhancement of the reaction rate of tri- and divalent ligands compared to monovalent ones. This was attributed to a distinct

multivalency effect resulting both from the ligands and the AuNPs surface. In addition, the kinetics of short-chain thiolates, amines, and disulfides were also investigated by EPR spectroscopy.[110]

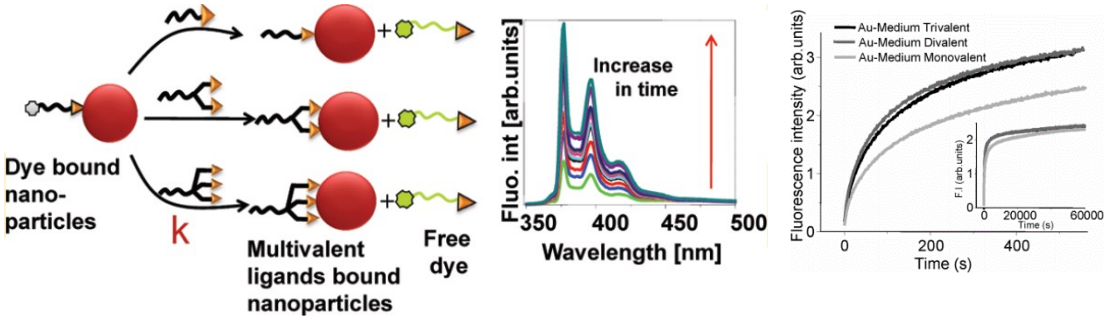

Figure 1-28. Representation of the effect of multivalent ligand in the IDA-based binding affinity assay (Reprinted from C. Graf *et al*., 2011[109]).

1.4.2 The binding event on protein corona

Nowadays it is generally accepted that when AuNPs are exposed to plasma or other biofluids, which contain myriad of proteins and other biomolecules, several proteins spontaneously adsorb onto the AuNPs surface forming the so-called protein "corona" through the protein-NPs interactions.[111, 112] However, the composition of protein corona is extremely complex and typically can change dynamically due to factors like the concentration of the different proteins, their composition and differences in the kinetic of binding versus the real equilibrium binding affinity of each of them in the environment. This last aspect is known as the Vroman effect. It says that more abundant proteins could dominate adsorption first (soft corona), but after longer times, those proteins can be displaced by less abundant ones with higher affinity (hard corona). In the overall process, not only covalent bonding between cysteine thiols and AuNPs is involved, but amines also may play a role.[113] Interestingly, the new "biological identity" of the AuNPs can contribute to improve their biocompatibility for various biological applications, such as cellular uptake, targeting of specific cellular receptors and drug delivery. They may, however, also mask them altering the functions for which they had been originally designed. Therefore, a comprehensive understanding of this dynamic process at the AuNPs surface is portal to the determination of the corona composition and the design of safe nanomedicines and biomaterials.

It is well known that binding events of proteins to AuNPs are often associated with electron or energy transfer, size or shape alterations, which makes the determination of binding affinity of proteins to AuNP possible by use of spectroscopy, dynamic light scattering (DLS), isothermal titration calorimetry (ITC) and other techniques.[114] To demonstrate this point, a study of the binding affinity of plasma proteins adsorbed on AuNPs was reported by S. Yu and co-workers.[115] In their investigation, nine type of plasma proteins, human serum albumin (HSA), trypsin (TRP), hemoglobin (Hb), myoglobin (MB), immunoglobulin G (IgG), carbonic anhydrase (CA), fibrinogen (FIB), chymotrypsin and r-globulin, were used to study the interaction with AuNPs whereby addressing the binding affinity according to ITC, DLS and fluorescence quenching (Figure 1-29). They found that the binding affinity is not only governed by the nature of the protein (the more surface cysteine residues, the higher the binding affinity for AuNPs is), but is also dominated by the particles size (the smaller AuNPs absorb less proteins). In addition, larger proteins prefer to bind to the AuNPs more strongly than the smaller ones due to the occurrence of more electrostatic interactions in the dynamic process. This is another manifestation of the multivalent effect.

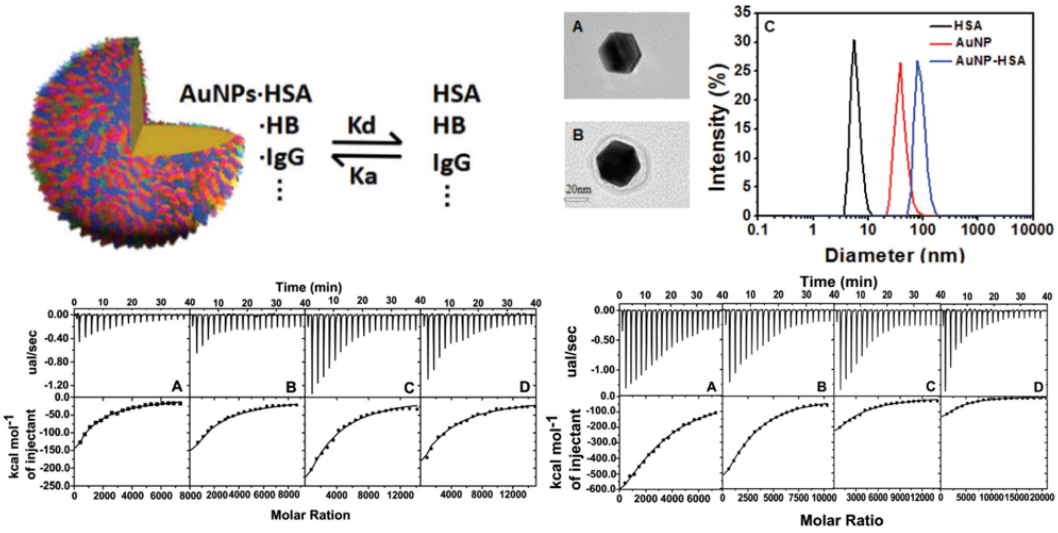

Figure 1-29. The schematic diagram of plasma proteins adsorption and dissociation on AuNPs, the DLS and ITC titration results of AuNPs and HAS. (Reprinted from S. Yu *et al*., 2017[115]).

1.5 The functionalized AuNPs to target proteins

Many diseases, such as tumor or Alzheimer's, are usually associated with the presence of certain biomarker proteins or abnormal protein concentrations.[116] Detecting this biomarkers (protein) at the early stage of the disease is the preferred approach for a successful cure or for a more efficient control of its effects. For proteins, however, the nonspecific binding, such as that leading to the protein "corona", has been a serious issue for long time since it may prevent specific interactions for target proteins not forming the corona. Furthermore, relying on an aspecific binding process is pointless. In fact, proteins have multiple binding sites, with positive or negative charges on the several residues present on their surface, they have hydrophobic or hydrophilic regions, which makes specific binding events extremely challenging.[117] As mentioned previously, the strategy of aggregation and disaggregation of AuNPs, which can lead to the dramatic change of the surface plasmon resonance property, has proven to be an effective read-out system for monitoring the enzyme or protein activity. However those experiments had been performed in vitro in a non-challenging environment. Because of this, non-functionalized (naked) AuNPs have severe limitions. It is, for instance, highly probable that the protease-triggered AuNPs dispersion reported previously may fail in a biological fluid because the interactions with the AuNPs that are at its basis may be fully lost due to the surrounding environment. It is generally accepted that non-functionalized (naked) AuNPs are more prone to adsorb proteins on their surface to form a protein "corona" in *vivo* or in *vitro* assays. Accordingly, the crosslinking ability of linkers can be masked by those proteins with high affinity in biofluid. In addition, it is well recognised that many crucial protein biomarkers are present at ultralow concentration at the early stage of the disease, therefore, the investigation of novel approaches for ultrasensitive detection, which has great strategic significance before symptoms in the clinical diagnosis appear, could be seriously hampered.

From the above considerations it appears unsuitable to use nanoparticles for proteins targeting without a proper functionalization for two reasons: first, the selectivity would be dictated by the intrinsic affinity and concentration in the biological milieu, second, even in the presence of a targeting molecule, interactions with unwanted proteins masking the AuNPs, must be strictly avoided. Because of this one must consider two aspects: AuNPs

targeting and making them stealth to unwanted proteins. For protein targeting, Cravatt and co-workers [118] have reported a powerful method, that takes advantage of the activity of enzymes in complex proteomes. The protocol is called activity-based protein profiling (ABPP). The strategy is mainly based on covalently labelling the active site of proteins by using a specific probe that will react with the protein (mostly enzymes) of interest. Later, proteins are separated by gel electrophoresis and mass spectrometry analysis, which is the direct ABPP. An alternative approach is two-step labelling, in which the protein is first labelled with a small chemical group and subsequently modified with fluorescent tags or azide moieties for a click-functionalization step (Figure 1-30).[119] However, in spite of the fact that the ABPP strategy provides an easy way to target specific classes of enzyme or to quantify protein levels in many environments, it still presents one important drawback due to the fact that labelled proteins must be separated from the complex mixture to allow their identification and quantification. This is significantly time-consuming and very dependent on the sample complexity itself.

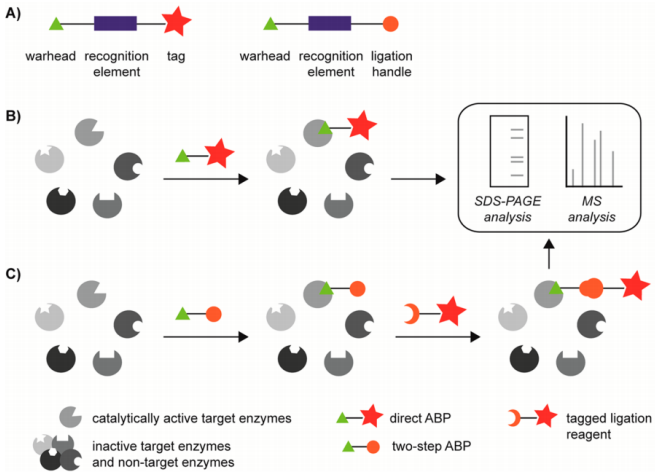

Figure 1-30. Schematic representations of one- and two-step ABPP strategies (Reprinted from S. I. Kasteren *et al*., 2014[119]).

Thus, one alternative that emerged recently is that based on the monolayer protected AuNPs for the specific binding of a single protein or discriminating a proteome in situ. One of the earliest work in this context is based on biotin-avidin chemistry for conjugation.[117] Avidin-biotin binding is a very much exploited strategy to connect molecules and macromolecules via a non-covalent bond that has the strength of a covalent one. Du Vigneaud and co-workers [102] have well described how the avidin-biotin system has a huge

potential as a tool for various biological applications. This strategy was employed to modify AuNPs for the ligation of specific binding functionality. X. Huang and co-workers reported (Figure 1-31) AuNPs that were modified with a mixed monolayer constituted by a tri(ethylene glycol) thiol and tiopronin.[117] They found that no binding event occurred with streptavidin, their target protein, because of the lack of a specific capture unit. By further derivatizing tiopronin with a biotin group a strong binding event was observed. In addition, the biotin coated AuNPs didn't show binding with other biomolecules, such as BSA, or lysozyme. The above is a simple example that highlights the concept of specific targeting of a protein. However, as said above, the biotin-avidin interaction is mostly used for the conjugation of biomolecules. Papers exploiting this approach for the binding of AuNPs to various proteins or enzymes have been reported. For instance C. Mirkin and co-workers [120] reported the detection of a protein (prostate-specific antigen) based on the biotin-polyethylene glycol (biotin-PEG) coated AuNPs. V. Rotello and co-workers [121] reported a "plug-and-use" system for binding biotin-HRP (horseradish peroxidase): the AuNPs were functionalized with a carboxybetaine zwitterionic headgroup, to which was covalently linked avidin allowing the system to form conjugates with any biotin functionalized biomacromolecule.

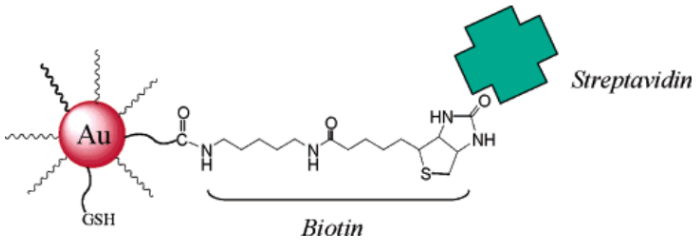

Figure 1-31. Schematic Illustration of the interaction of biotin coated AuNPs with a treptavidin molecule (Reprinted from X. Huang *et al*., 2004[117]).

Specific surface modification of AuNPs have been reported for targeting several proteins. M. Kogan and co-workers [122] reported a peptide CLPFFD-NH_2 protected AuNPs which can selectively bind β-amyloid fibrils (Aβ). A diverse range of functionalized AuNPs have been prepared for the detection of proteome by V. Rotello [123] The group has developed a highly sensitive array-based sensor system for identification of protein in serum based on FRET-based "chemical nose" strategy using the "green" fluorescent protein (GFP) for detection (Figure 1-32). In their study, the AuNPs were functionalized

with thiolated ligands terminating with five cationic groups and different flanking chains, each featuring different groups (hydrophobic, aromatic and providing hydrogen bonding ability). Afterwards, the cationic AuNPs interact with the anionic GFP through electrostatic interactions resulting in fluorescence quenching. In the presence of analyte proteins, a competitive binding process occurs, where the different binding affinity of analyte protein to the AuNPs allows a positive or negative fluorescence response. This fluorescence-based chemical nose sensor array has been successfully used to identify unknown protein samples and discriminate different concentrations of the same protein in a mixture of proteins.

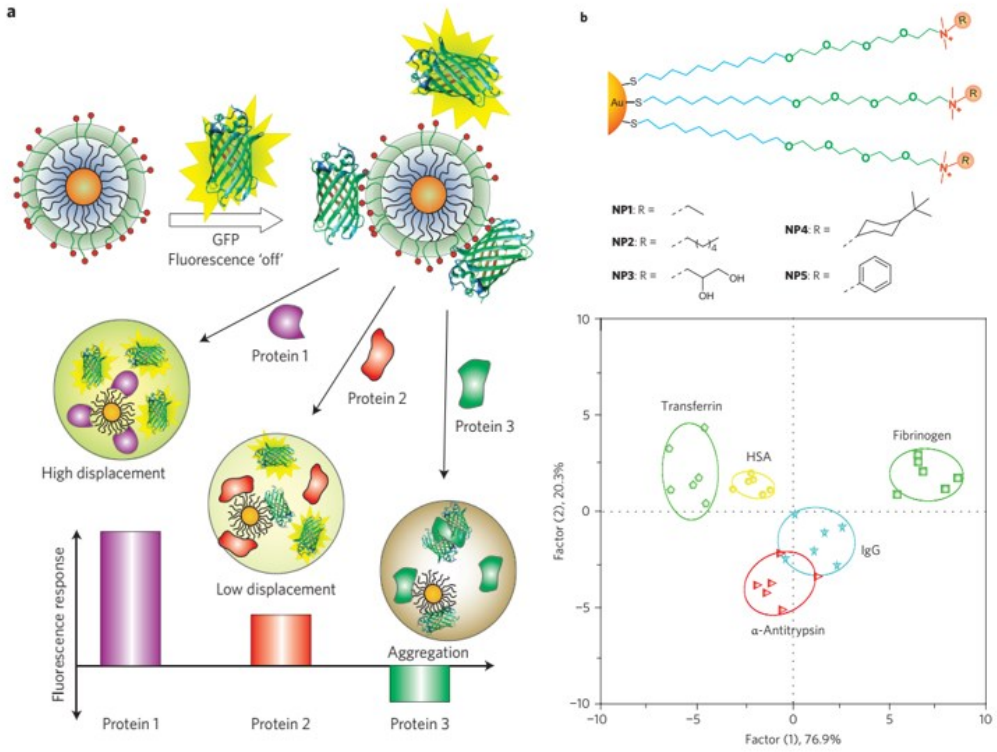

Figure 1-32. Representation of the mechanism of chemical nose sensing array (Reprinted from V. M. Rotello *et al*., 2009[123]).

In summary, AuNPs have attracted the interest of the scientific community because they are easy to obtain and have unique physical and chemical properties. The fact that they can also very easily be modified through the passivation with a monolayer of organic molecules constitutes a very important property. The investigation of the interaction of biomolecules and AuNPs constitutes an important prerequisite for their application in biomedicine, drug delivery, diagnostics and therapeutics. There is no doubt that the distinctive features of the AuNPs will allow to continue to expand their use in the field of biological applications.

1.6 Aims and objectives

As I have tried to show above gold nanoparticles are nanomaterials that are becoming more important every day particularly for their use for biological applications such as imaging, sensing or drug delivery. Nevertheless, studies addressing the basic aspects related to the interactions of AuNPs with biological molecules are still scarce. In particular, the interaction of one of the most important functional group presents in biomolecules, the amino group, with the gold surface is still poorly understood. Furthermore, although strategies for targeting proteins have been developed, there is still plenty of room for developing new and more efficient ones. This PhD thesis aims to address specifically these problems.

It focuses on the following aspects:

1) The investigation of the affinity and the binding mode of amines to the surface of AuNPs.

2) How amine-driven interactions may control nanoparticle aggregation and morphology by studying:

    a) the crosslinking of AuNPs controlled by the helical conformation of oligopeptides;

    b) the aggregation and fusion into nanowires of AuNPs induced by glucosamine phosphate.

3) The functionalization of AuNPs with irreversible enzyme inhibitors for the covalent capture of target proteins.

Chapter 2. Affinity of amines for the surface of AuNPs

2.1 Introduction

Determination of biomolecules binding affinity for the AuNPs surface is of fundamental importance in nanoparticle research and to study the interaction between biomolecules and AuNPs. Once the surface of AuNPs has been engineered with proper functionalities like thiols, amines and phosphorus derivatives, they are endowed with new properties changing the identity of the nanomaterials.[2, 4] Approaches for the synthesis and stabilization of AuNPs have been devised. One of the most commonly used method, which takes advantage of the strong, almost "covalent" bond RS-Au, utilizes the capping with functionalized alkyl-/aromatic-thiols of the AuNPs surface.[77] When these capping molecules are functionalized with proper functional groups the AuNPs can be used for specific applications as, for instance, for targeting tumor cells and tissues or other biomolecules thus acting as specific biomarkers for cancer therapy.[118] Thiol chemistry as the main approach for surface functionalization of AuNPs has been extensively investigated in the last decades. The point of fact is that the nature of the Au-S bond and the mechanism of place replacement of thiolate species on the AuNPs surface is mostly understood. However, the interaction between the AuNPs and natural biomolecules does not rely mostly on the strong "covalent" S-Au bond. Weak connections are instead governing the interaction between the gold surface and biomolecules like amino acids, peptides or proteins, and they rely on the presence of amino groups on these molecules.[87]

The presence of amines on these biomolecules is overwhelmingly more relevant than that of thiols and, accordingly, the interaction they may establish with the gold surface is completely different from that constituted by thiols or thiolate species. It is surprising that this problem has not been addressed properly so far with a thorough analysis of the nature of the N-Au bond. For this reason, there is not a clear binding mode accepted by the scientific community for amine binding to AuNPs. Questions concerning how the structure of the molecules, their acidity and basicity, for instance, affect their role as passivating agents of the surface of AuNPs are still unanswered. Nevertheless, several studies have been performed concerning the crosslinking of AuNPs induced by amino acid as well as oligopeptides.[67, 93] For instance, I will discuss in the next chapter that by placing two amino

groups at the C- and N-terminus of a peptide sequence, folded into a helical conformation, efficient crosslinking of AuNPs in ethanol is observed. Recently, we have also found that the mode of aggregation of the AuNPs is not only related to the secondary structure of peptides but also to the particle size. In the case of small size AuNPs, they prefer to aggregate in a globular conformation, on the contrary, bigger size AuNPs prefer to assemble through a necklace-like conformation leading to a network of nanoparticles. Thus, we also speculated that the binding affinity will be affected by the dimension of AuNPs.

The dependence between an amine adsorption to AuNPs and its nature calls for a better understanding of the thermodynamics and kinetics of the process in order to establish a correlation between the properties of the amines and that of AuNPs surface. Once this property will be assessed defining the different interaction ability, the passivation of AuNPs can be tuned for designing tailored AuNPs to be used as a versatile nanomaterial for technical and biological applications. Thus, we set up experiments aimed at understanding how amine-based ligands interact with the AuNPs surface through ligand exchange reactions. Our idea was that this could guide us in formulating a binding model and to control the introduction of novel functionalities on nanoparticles. It should be remembered that the AuNPs surface is imperfect which results in an uneven distribution of gold atoms that may cause different local chemical reactivity. Several reports have shown how the binding sites of AuNPs are affected by the particles size,[108, 109] but systematic studies of how the pKa of ligands and the size of the AuNPs affect the thermodynamics and the kinetics of ligands exchange on AuNPs of different size have not been reported. The key problem is that the ligand exchange reaction is difficult to follow. However, optical methods like fluorescence spectroscopy have the capability to probe these exchange processes in a reliable way. An example of this approach concerning the study of the Au-SR interaction has been already discussed in the Introduction.

On the basis of above discussion, in this chapter I will discuss the use of non-covalent AuNP-dye conjugates to quantify the binding affinity. I have selected primary, secondary and tertiary amines capable of replacing the indicator by ligand exchange reactions. In spite of the different chemical structures, amine-based molecules share the presence of the amine headgroup, which is one of the most important binding functional groups when amino

acids, peptides and protein interact with AuNPs. The rationale behind the choice of these three class of amines was to build an interaction model for the protein-AuNPs binding system. Thus, I focused my attention on primary, secondary and tertiary amines as competitors to quantify their binding affinity to AuNPs in an indicator displacement assay on nanoparticles of 10 nm, 15 nm, and 25 nm diameter. A primary amine functionalized with a pyrene unit was used to completely passivate the AuNPs surface. Its fluorescence is fully quenched when bound to the AuNPs and it is restored when it is released. Accordingly, it acts as an indicator to probe the ligands replacement on the surface of AuNPs. The relative binding affinity was obtained by titration with increasing amounts of entering amine following the resulting fluorescence enhancement. The obtained relative binding constants were then correlated with their pKa in ethanol, the solvent used.

2.2 Indicator displacement assay

2.2.1 AuNPs design

I first addressed the problem of what sort of nanoparticles I had to consider, the presence of possible passivating agents and the solvent of choice for my experiments. The AuNPs were synthesized with the Turkevich method as discussed in the introduction. However, with this synthetic protocol citrate is present in large excess and it acts as a passivating agent of the AuNPs.[124] Thus, I decided to prepare citrate-depleted AuNPs (9 nm in diameter), removing the maximum amount of passivating agent that was leading to a system still stable in solution at the concentration used. Accordingly, AuNPs were washed 5 times with MilliQ water and were eventually investigated by TGA analysis before and after citrate depletion. The results showed that, although citrate (and possibly its oxidation products as dicarboxyacetone) was still present, ca. 1/3 of (Table 2-1 and Figure 2-1) of the gold atoms on the surface of the nanoparticles was not passivated. This was the minimum amount of citrate I could remove being still able to manipulate the AuNPs without observing aggregation and/or precipitation phenomena. Although water should be the solvent of choice for studying the interaction of AuNPs with biomolecules, I eventually opted for using ethanol instead.[125] Ethanol is a good compromise: on one side it is still a protic solvent like water, on the other it prevents the aggregation of less polar amines that I would have to use in my study. It is well known that lipophilic amines passivating the

surface of AuNPs in water lead to their aggregation, a process that would have compromised my studies. The protocol described here for the preparation of the AuNPs as well as the solvent utilized were also used for all studies that I have performed and described in the subsequent two chapters.

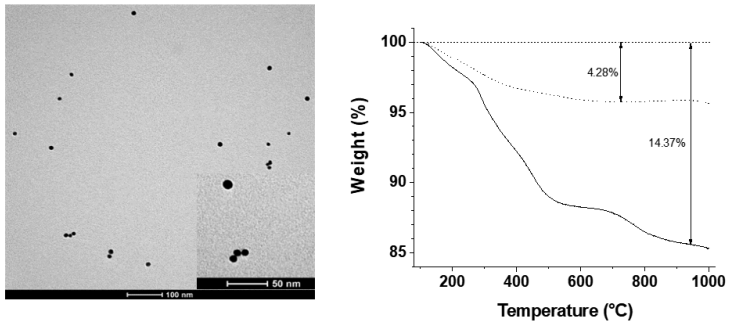

Figure 2-1. TEM image of the AuNPs used for the experiments after the washing and dissolution in ethanol, size bar is 100 nm. Inset: magnified picture, size bar is 50 nm. Thermogravimetric graph of the "as-prepared" AuNPs sample (solid line) and after washing (dotted line). Arrows indicate decrease in weight with respect to 100% (dashed line).

Sample	"As-prepared"	Washed
% Organic	14.37	4.28
mg citrate	0.1437	0.0428
mg Au	0.8563	0.9572
µmol citrate	0.74795	0.22277
µmol Au	4.34758	4.84987
µmol Surface Au	0.591752	0.66148
Citrate / Surface Au	1.26	0.34

Table 2-1: Thermogravimetric analysis of "as-prepared" and washed nanoparticles. 1 mg of nanoparticles taken as an arbitrary value for the calculations.

It should also be mentioned that, compared to water, ethanol is known to magnify the interactions between putative ligands and the AuNPs surface. It could also enhance aggregation processes between the nanoparticles, a phenomenon that, luckily, did not affect the studies performed in this chapter.

In the introduction I have discussed how the interaction of the AuNPs with thiols depends on the presence of edges, flat surfaces and defects that can be modulated by changing the size of AuNPs.[108] Taking this into consideration, we decided to investigate three different sizes of AuNPs to quantity the binding affinity. The citrate-stabilized AuNPs (10, 15, 25 nm) were purified and resuspended in ethanol before any further study. Since

the percentage of gold atoms on the surface with respect to the total amount of gold of the nanoparticles is changing with the particles size, the concentration of AuNPs used was different for the different sizes studied.

2.2.2 Surface saturation concentration (SSC)

As mentioned above, the determination of affinity of the amines to the AuNPs was carried out taking advantage of the displacement of a fluorescent indictor from their surface. For this type of displacement, the concentration of the indicator should be equal to the surface saturation concentration (SSC), which is the maximum number of fluorescent indicator molecules that can be simultaneously absorbed on the surface of the AuNPs. This avoids having non-passivated surface Au atoms at the beginning of the experiment on one died and free, unbound fluorescent indicator, on the other. The value of SSC can be influenced by several factors, such as the particles size, the concentration of AuNPs, and the distance between the fluorescent unit and AuNPs. In order to choose the best fluorescent indicator and conditions I performed explorative studies with AuNPs of all three sizes and two type of fluorescent indicators (**1** and **2**) featuring the same fluorescent probe (pyrene), different spacers and two amines of different basicity (Scheme 2-1). The SSCs of the indicators for the AuNPs were assessed by adding increasing amounts of indicators to the solutions of AuNPs (10-25 nm, [Au] = 30 μM) at different temperature. The adsorption of amines to the surface of AuNPs could reach equilibrium following a kinetically slow process. Therefore, I have recorded the evolution of the fluorescent spectra for times long enough to ensure the adsorption event had reached the equilibrium. Afterwards, the final fluorescence intensity was plotted as a function of the concentration of the fluorescent indicators.

The values of SSC between the AuNPs and fluorescent indicators are reported in Table 2-2. For each titration, the SSC is determined via extrapolation of the linear part of the titration curve (Figure 2-2). The curves are flat with almost no fluorescence observed at low indicator concentration because the fluorescence is quenched for the interaction with the nanoparticles. Once the surface of the nanoparticles is saturated, no more indicator can bind to it and the fluorescence starts increasing in a linear way. Concentrations of AuNPs were properly selected to avoid aggregation and precipitation. Inspection of the titration

data revealed that different values of SSC were obtained when different size of AuNPs were explored. In general, a little bit higher values of SSC were observed for bigger nanoparticles in comparison with the smaller ones. This observation is consistent with our calculations. The presence of the amide group in the chain of the indicator **2** does not affect the number of indicators binding to the surface of AuNPs for all three types of them when compared to indicator **1**.

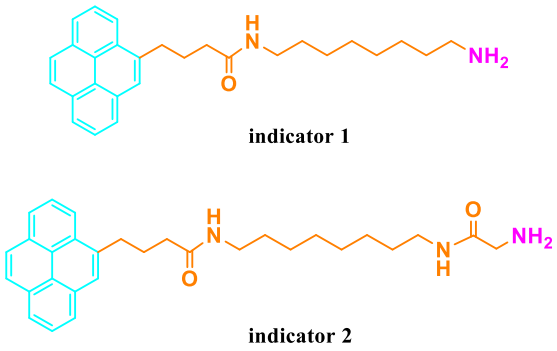

Scheme 2-1. The chemical structure of indicators.

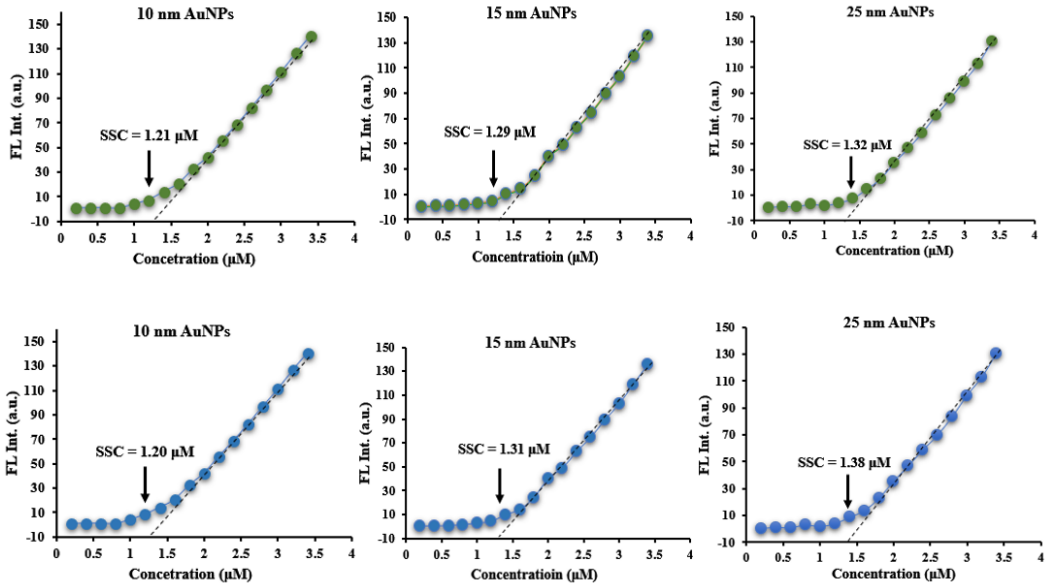

Figure 2-2. Fluorescence intensity as a function of the amount of indicator **1**(upper), indicator **2** (lower) to a solution of AuNPs in 10 nm, 15 nm, and 25 nm diameter in ethanol. λex/em = 328/395 nm, slit 10/10 nm. (Note: All the experiments were repeated three times and obtained the final average data at 25-40 ℃).

AuNPs	SSC[a]	
	Indicator 1	Indicator 2
10 nm AuNPs	1.21 μM	1.20 μM
15 nm AuNPs	1.29 μM	1.31 μM
25 nm AuNPs	1.32 μM	1.38 μM

a: All values were obtained at 25-40 °C and were the average of at least three measurements. [Au] = 30 μM.

Table 2-2. The vales of SSC obtained for the two indicators and the different AuNPs.

2.2.3 Binding affinity of amines to AuNPs

On the basis of above results, which confirmed that indicator **1** and **2** are good reporters for the displacement assay because of the high intensity of the fluorescence of the pyrene unit, I set up an indicator displacement assay to monitor the specific response of AuNPs to the various competitors. Indeed, there are several types of non-covalent bond potentially involved in the interaction between the AuNPs and incoming molecules, such as electrostatic, van de Walls, and hydrogen bonding. Here, we speculated that the interaction of the binding molecules bearing amine group with AuNPs occurs through the lone electron pair on the N atom. In order to understand how the nature of the different amines generates the different response patterns, we selected primary-, secondary-, and tertiary-amines competitors on the basis of their pKa and structure (Table 2-3).[126] I had in mind to determine if a correlation exists between amine basicity (and hence its pKa) and its affinity constant for the gold surface.

Primary	**pKa,** EtOH calc	**Secondary**	**pKa,** EtOH calc	**Tertiary**	**pKa,** EtOH calc
Heptylamine (**P1**)	9.15	Pyrrolidine (**S1**)	9.06	3-Quinuclidinol (**T1**)	8.29
3-Methoxypropylamine (**P2**)	8.77	Piperidine (**S2**)	8.94	1-Methylpyrrolidine (**T2**)	7.69
2-Methoxyethylamine (**P3**)	8.50	Morpholine (**S3**)	7.21	N-Methylphenethylamine (**T3**)	7.48
2-amino-N-pentylacetamide (**P4**)	7.80	N-Methyl-2-phenylethylamine (**S4**)	8.25	N-Dimethylhexylamine (**T4**)	6.57

Table 2-3. The pKa of competitors for displacement assays, the pKa values are calibarated properly in EtOH at 25 ℃

To begin with, the competition experiments were carried out in the presence of AuNPs (9 nm) fully covered by the fluorescent indicator **1** or **2**. The indicator concentration was selected to reach 98% of its SSC to guarantee full fluorescence quenching in the absence

of added competing amine. In order to assess the affinity of the indicators for the AuNPs, amine (P1) was chosen as a competitor in a preliminary investigation. I recorded the fluorescence spectra in the 350-700 nm interval (upon excitation at 328 nm) for several minutes until the ligand exchange reaction had reached the equilibrium. In these preliminary experiments the competitor was added to the AuNPs exploring the 50-500 μM concentration interval. The resulting data are reported in Figure 2-3. In the analysis of the data, a low exchange efficiency and some precipitation of AuNPs was observed when indicator **1** was employed. Since the pKa of **1** is higher than that of **2** (9.15 and 7.61, respectively in water), this suggested that the binding affinity to the AuNPs of **1** and **2** somehow correlated with the pKa of the two different amines. The precipitation observed also suggested that **1** is less soluble than **2** in the conditions used for the experiments. The increase of fluorescence intensity depends not only on the concentration of added amine but also on time, which means that the exchange equilibrium is relatively slow.

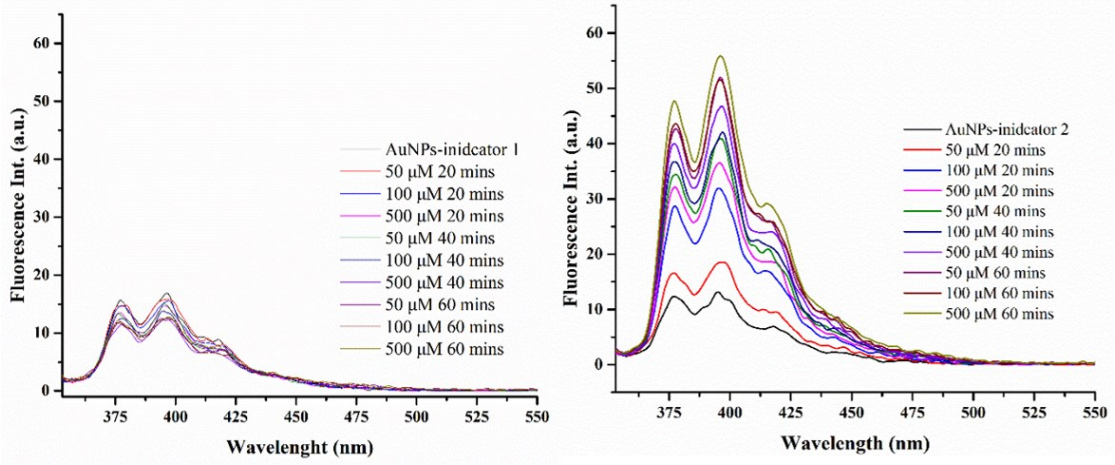

Figure 2-3. Fluorescence spectra of displacement assays to assess the affinity of the indicator 1 (left) and indicator 2 (right) for the AuNPs in EtOH at 25 °C, [Au] = 30 μM, λex/em = 328/395 nm, slit 10/10 nm.

With these preliminary results in hands, I selected indicator **2** as my choice for all subsequent exchange experiments because, being more weakly bond to the AuNPs surface, it could be more easily exchanged also by amines with lower affinity. Before exploring the effective displacement ability of the entire set of amines considered I have analysed in detail the kinetics of the exchange process, by studying representative amines P1, S1 and T1 (a primary, a secondary and a tertiary one). Figure 2-4 reports the fluorescence increase at 395 nm (λ_{ex}=328 nm) in the course of one hour following their addition. Analysis of the curve reveals that, after a fast increase in fluorescence intensity at the initial stage, the

process continues but at a much slower rate as also shown in the inset of Figure 2-4. Such a behaviour indicates that there are two different binding modes of the fluorescent amine to the AuNPs surface, which are characterized by two different exchange kinetics: a fast and a slow one. It should be pointed out that a third fraction of dye could not be removed even at the highest concentration of competing amine added even after waiting for long times (days). This fraction could only be removed by addition of a strongly competing thiol. Thus, we should infer that there is a third population of dye bound very strongly to the gold surface. The kinetic processes related to the first two detachment events could be fitted very well by using a biexponential equation (eq. 2-1 and Table 2-4).

$$I(t) = A_1(1-e^{-k_1 t}) + A_2(1-e^{-k_2 t}) \qquad \text{eq 2-1}$$

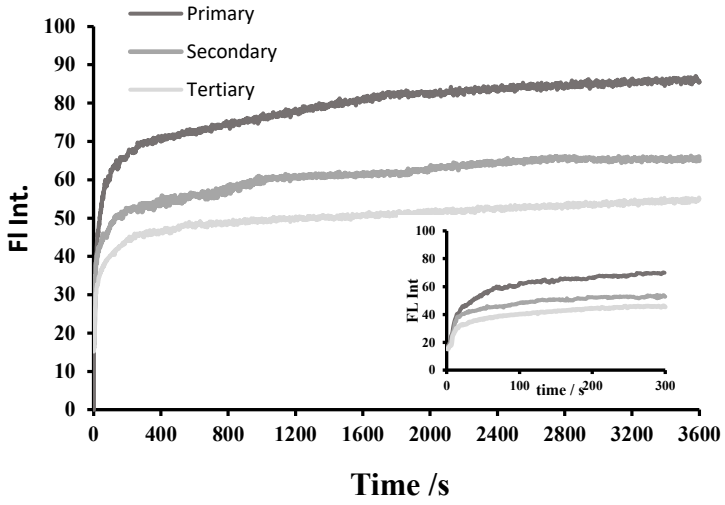

Figure 2-4. Changes in fluorescence intensity at 395 nm as a function of time for a wider time interval of the ligand exchange of primary, secondary and tertiary amine against the pyrene on AuNPs surface. The inset shows the kinetic of rapid exchange for the initial stage. (Note: The kinetics experiments were performed in ethanol at 25 ℃ for 1 hour, λex/em = 328/395 nm, slit 10/10 nm)

Type of amine ligands	$k_1 \times 10^{-2}$, (s^{-1})	$k_2 \times 10^{-4}$, (s^{-1})
P1	2.9	8
S1	4.6	9.1
T1	1.5	3.8

Table 2-4. The rate constants of the ligand exchange of primary, secondary and tertiary amines P1, S1 and T1 using a biexponential fit function.

The rate constant k_1 stands for the initial stage of ligand exchange, it's a fast process, meanwhile, k_2 is the rate constant of the slower process that occurs at a second stage. Graf et al.,[109] studying a similar phenomenon occurring during thiol exchange reported that the ratio of the amplitudes A1 and A2 varies significantly following the geometry of the AuNPs surface. In their model, they assumed that the number of gold atoms on the edges and vertices, were related to the faster process (numerically related to A1), while the number of gold atoms on the flat surfaces were related to the second amplitude (A2) and the slower process. Following this way of reasoning they formulated a hypothesis for predicting the geometry of gold nanoparticle surfaces according to the ratio of the amplitudes. Since the ratio edges and vertices vs flat surfaces changes following the size of the AuNPs, I performed preliminary experiments also with AuNPs of 15 and 25 nm diameter. The experiments were performed under identical conditions as above (λ_{ex}=328 nm, λ_{em}=395 nm). As shown in Figure 2-5 there seems to be some dependence from size but not as big as expected. As reported in Figure 2-5, the rate constants and A1/A2 ratio of small, medium, big nanoparticles are not much different one from the other. Such observation could indicate that the explanation provided for the binding of thiols to AuNPs is not true for the binding of amines. These experiments are, however, only preliminary and a better investigation is needed.

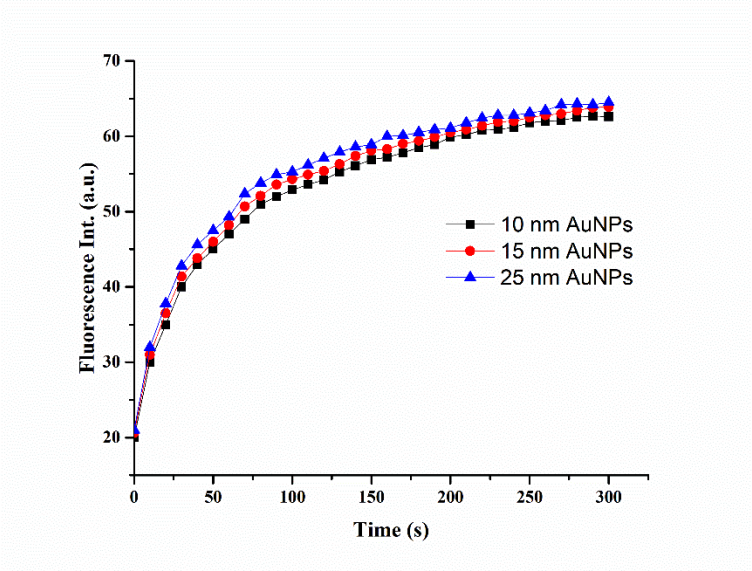

Figure 2-5. Changes in fluorescence intensity at 395 nm as a function of time for the ligand exchange of primary amine (P1) against pyrene probe **2** on AuNPs surface (10, 15, and 25 nm). (Note: The experiments were performed in ethanol at 25 °C for 5 minutes, λex/em = 328/395 nm, slit 10/10 nm)

Next, I turned my attention to the role played by the temperature in the ligand exchange reaction. Therefore, I run exchange kinetics of amines (P1, S1, T1) at different temperatures for better understanding how the temperature possibly affects the exchange behaviour. Ligand exchange reactions were carried out at 25, 30, 35, 40 °C, respectively. The resulting data are reported in Figure 2-6. Inspection of the kinetic data reveals that, as expected, the saturation states of the exchange process were reached faster at a higher temperature for all amines while the exchange reaction process is slower at low temperature.

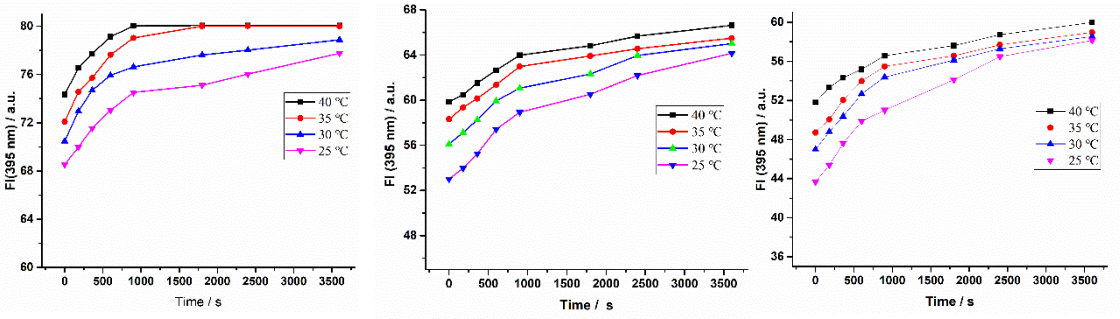

Figure 2-6. Changes in the fluorescence intensity at 395 nm as function of time for the P1, S1 and T1 at different temperature. (Note: The experiments were performed in ethanol at 25-40 °C for 1 hour, λex/em = 328/395 nm, slit 10/10 nm)

2.3 The role of pKa

The above experimental results indicate that the exchange reaction of amines on the AuNPs surface follows a time- and temperature-dependent multimodal pathway. Apart the preliminary results with the fluorescent indicators **2** that suggested a possible correlation of the amine pKa and its affinity for the AuNPs surface, I had not precise indication if such a correlation does in fact exist. Indeed, I was very curious to know if the relative affinity constants determined with the displacement experiments reported above, once extended to the full set of amines, could correlate with their basicity. The set of amines was selected in such a way to explore a relatively large pKa interval. Since I was working in ethanol, I wanted to use the correct values for this solvent. Experimental pKa in EtOH for all of them are not available. However, B. E. Ivanov *et al.*,[126] have reported an equation to correlate the pKa in water with that in EtOH for primary, secondary and tertiary amines. The values for the pKa of all amines studied determined using this equation are reported in Table 2-3.

Displacement experiments were hence carried out using 10 nm AuNPs loaded with indicator **2**. The experiments were performed at 35 °C to ensure a reasonably fast exchange rate. As expected, when the AuNPs/indicator **2** complex was treated with competing amines of different pKa, the system displayed a different response to the incoming molecules. Such differential response was the fundament for the quantification of relative affinity. Figure 2-7 (left) shows that by following the increase of fluorescence at 395 nm, reasonably well-behaved binding isotherms could be obtained. The apparent binding constants obtained by interpolation of these binding isotherms for all amines studied are reported in Table 2-5. For the most weakly binding ones for which only partial displacement of the fluorescent dye was obtained, the values reported represent approximate estimates. It must also be pointed out that the binding constants reported refer to the first two exchange processes (as discussed in the kinetic section above) as the full depletion of the fluorescent dye was never observed even with the most strongly binding amines.

Priamry	Apparent binding constant / M^{-1}	Secondary	Apparent binding constant/ M^{-1}	Tertiary	Apprent binding constant / M^{-1}
Heptylamine (**P1**)	0.55×10^{-3}	Pyrrolidine (**S1**)	0.42×10^{-3}	3-Quinuclidinol (**T1**)	4.46×10^{-3}
3-Methoxypropylamine (**P2**)	1.00×10^{-3}	Piperidine (**S2**)	0.60×10^{-3}	1-Methylpyrrolidine (**T2**)	5.82×10^{-3}
2-Methoxyethylamine (**P3**)	1.44×10^{-3}	Morpholine (**S3**)	1.00×10^{-3}	N-Methylphenethylamine (**T3**)	3.98×10^{-2}
2-amino-N-pentylacetamide (**P4**)	4.07×10^{-3}	N-Methyl-2-phenylethylamine (**S4**)	3.89×10^{-3}	N-Dimethylhexylamine (**T4**)	4.47×10^{-2}

Table 2-5. The relative binding constant determined for all the competing amines to the gold surface of 10-nm AuNPs.

I have then plotted the estimated pKa in ethanol of the different amines against the Log of the relative binding constants obtained from the exchange experiments. As revealed by the Figure 2-7 (right), the displacement experiments clearly show that the relative affinity to the surface of AuNPs correlates reasonably well with the pKa of all amines we used, in particularly, for the primary and secondary ones. For the tertiaries the points are more scattered. I hypothesize that for these amines some other parameter should be taken into consideration. The most obvious one appears to be the steric hindrance. In addition, for each class of amines, the affinity constant decreases as the pKa value increases. The slope of the three lines is -0.64, -0.49 and -0.62 for the primary, secondary and tertiary amines, respectively. The fact that the slope is lower than 1 (in absolute value) indicates that the

affinity of the amines for the proton (their basicity) is higher than that for the AuNPs surface, although the same parameters appears to influence both phenomena. The lowest value of the slope (always as absolute value) is that of the secondary amines, although it does not appear that the difference is so relevant. As a last consideration it should be pointed out that the maximum amount of fluorescent amine exchanged appears to depend on the type of entering amine used and not on their apparent affinity for the gold surface. Since on moving from primary to tertiary amines less dye is displaced from the surface, we hypothesize the removal of the last portion of it is hampered by steric hindrance as the amine of **2** is a primary amine. This is just a hypothesis that needs to be further verified with other investigations. Because of this, a theoretical simulation of the N-Au interaction on the gold surface will be performed using also data from XPS, solid-state NMR and FT-IR analysis which are in progress. With this information in hands we hope to be able to offer a more precise binding model of the amines to the gold surface. This could be useful also for biochemical applications, perhaps for correlating proteins pI with their affinity for the gold surface.

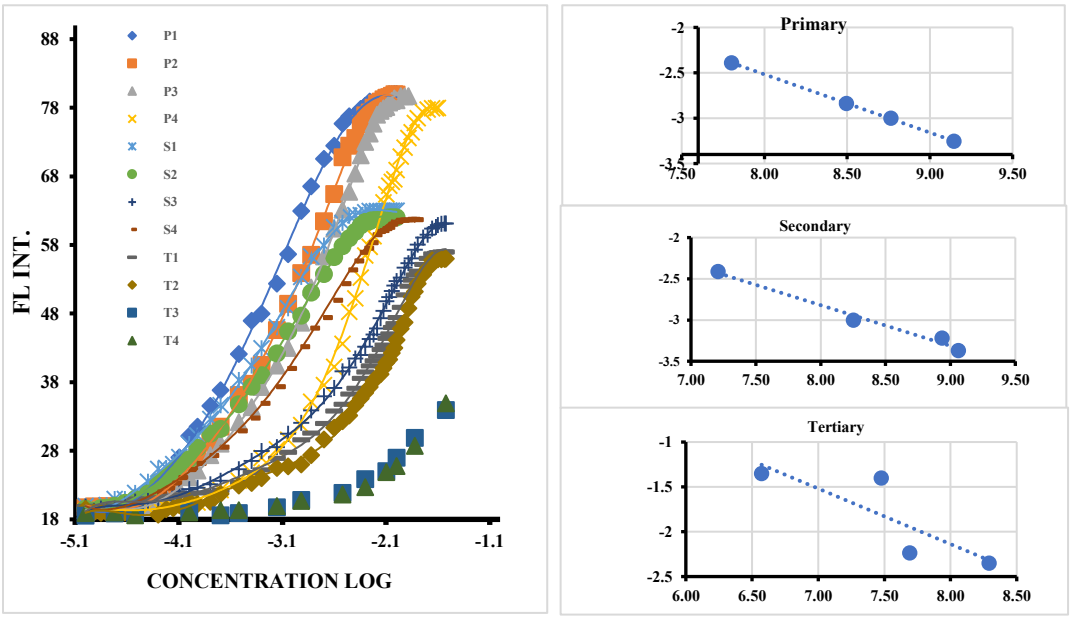

Figure 2-7. Change in the fluorescence intensity at 395 nm as a function of log concentration of competitors, the correlation between binding affinity and pKa. (Note: The experiments were performed in ethanol at 35 °C, [Au] = 30 μM, λex/em = 328/395 nm, slit 10/10 nm)

2.4 Conclusion

In summary, I have reported a convenient approach which can be used for quantifying the binding affinity occurring between gold nanoparticles and amine-based ligands. The investigation of fluorescence increase observed when a dye functionalized with pyrene (quenched by AuNPs) is exchanged by different classes of amine-based ligand provides interesting information on the nature of the Au-N interaction. The exchange efficiency is temperature dependent. Furthermore, the binding kinetics of the ligand exchange of primary, secondary and tertiary amine on gold surface reveals that there are apparently three binding modes. I was able to monitor two of them while the third one (the slowest) remains elusive. In addition, I have demonstrated that by studying the interaction of an extensive set of amines with AuNPs, a correlation between their pKa and the relative binding affinity to the AuNPs surface can be established. Other parameters appear at play, like for instance, steric hindrance, particularly for tertiary amines. The investigation is ongoing to assess the nature of the three different modes of binding of the amines to the gold surface of the nanoparticles.

Chapter 3. Oligopeptide helical conformation controls gold nanoparticles crosslinking

3.1 Introduction

As I have explained in the introduction, gold nanoparticles are known to interact with several functional groups with different strength.[127] This allows their passivation with organic molecules. Thiols form very strong bonds [77, 127, 128] but also amines interact with the gold surface as we have seen in the previous chapter,[90, 127] although much more weakly. When two of these functional groups are present on the same molecule, crosslinking may occur.[83, 129]

It should be clear from what I have reported in the introduction that when the diameter of AuNPs is larger than 3 nm the interaction between the AuNPs and functionalized molecules that can crosslink them can be easily detected even with the naked eye because of the change of the absorption spectrum in the region of the Surface Plasmon Resonance (SPR) band that red-shifts to longer wavelengths (from ca. 515 up to >600 nm, depending on the aggregate formed). The color of the solution changes from pinkish-red to bluish. This property is at the basis of several analytical applications of AuNPs.[130] Such a unique chemicophysical feature has allowed many scientists to publish important contributions also for biological applications.

As already mentioned, among biological molecules, several amino acids have been reported to act as crosslinking agents taking advantage of the presence, on the same molecule, of several functional groups [67, 131, 132] able to interact with the gold nanoparticle surface. Other systems as, for instance, ω,ω-bis-thiolated peptides have been used as reporters of proteases [84, 85] or phospholipases [93] taking advantage of the disruption of their crosslinking properties upon hydrolysis. Polymer-conformation theory predicts that, for an ideal, unordered polymer or oligomer there are more microscopic states compatible with a short end-to-end distance than those compatible with a large end-to-end one. As a consequence, an oligomer or polymer properly functionalized at both ends with functional groups able to interact with the AuNPs surface (“sticky” ends) could elicit crosslinking according to its ordered or unordered conformation (Figure 3-1). In this unordered polymer

the two "sticky" ends would likely bind to the same AuNPs. An example of such an oligomer is constituted by a peptide sequence that could assume a random coil or helical conformation depending, inter alia, on the length of the sequence, its amino acid composition and the surrounding environment.[133-135]

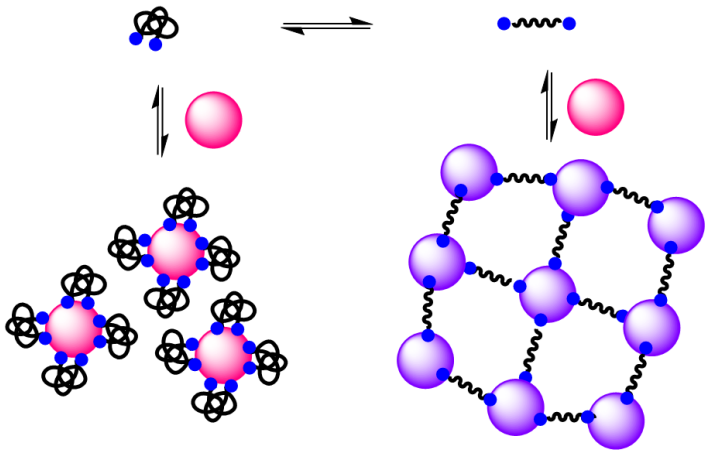

Figure 3-1. Equilibrium between a "sticky ends" polymer in an unfolded (top left) and folded (top right) conformation leading to isolated (bottom left) or clustered AuNPs (bottom right). The picture refers to an ideal polymer. The scenario may be less simple with a complex polymer like a protein.

I argued that, by exploiting two amino groups (the "sticky" ends) at the C and N-terminus of a peptide sequence, only those assuming a prevailing helical conformation would be able to cross-link AuNPs while disordered ones would have much less chances to do so. In a helical conformation, the two amino groups would be placed at opposite positions while peptides assuming a prevailing random coil one, would be much less efficient due to the closer relative placement of the two terminal amino groups. At variance with an S-Au bond, which is almost irreversible [136] (at least in the time scale of a crosslinking experiment), an N-Au interaction is in a relatively faster kinetic exchange regime. This would allow the AuNPs to report on the relative position of the amino groups through the amount of crosslinking occurring in a process governed by thermodynamics and not by kinetics.

In this chapter, I report a detailed investigation on the crosslinking of AuNPs with a series of well-designed oligopeptides, featuring primary amines both at the C- and N-terminus. Electronic circular dichroism combined with UV-visible experiments indicated that the ordered conformation of those peptides could effectively induce gold nanoparticles aggregation while disordered ones are poorly effective on this regard. Accordingly, the crosslinking of the 10-nm nanoparticles I have used is strongly dependent on the helical

content of a peptide sequence or, said in other words, helicity of the peptides controls the aggregation of the AuNPs. These findings represent the basis of the correlation between crosslinking ability of a properly functionalized peptide and its helical content, which are thus able to allow me to build a programmed crosslinking model.

3.2 Peptides design

To study the crosslinking ability of peptides, the peptide oligomers that were explored in this part were chosen among those assuming a well-defined helical conformation to compare their crosslinking abilities with those of disordered (random coil) sequences. As a general remark, the onset of such a folded conformation in short peptides comprising only proteinogenic amino acids requires at least 16 of them in the sequence to stabilize this conformation with respect to a random coil,[137, 138] depending whether the single amino acids are more or less helicogenic. However, work by several laboratories have shown that as little as 6-7 amino acids are required in a sequence comprising α,α-disubstituted amino acids to induce a helical conformation.[139, 140] It is evident that, the simplest of them is α-aminoisobutyric acid (Aib), which is a $C_{\alpha,\alpha}$ disubstituted amino acid and the Aib-rich peptides are typically assuming a helical conformation. These amino acids, although not present in proteins, are produced by microbial sources. In this way, short peptides comprising in their sequence α,α-disubstituted amino acids represent, hence, easily accessible foldamers and constitute excellent probes to validate our hypothesis.

Compound	Peptide sequence[a]
$\mathbf{A_{Ala,1}}$	H-Ala-NH$(CH_2)_2NH_2$
$\mathbf{A_{Aib,2}}$	H-Aib- Ala-NH$(CH_2)_2NH_2$
$\mathbf{A_{Ala,3}}$	H-Ala-Aib- Ala-NH$(CH_2)_2NH_2$
$\mathbf{A_{Aib,4}}$	H-Aib-Ala-Aib- Ala-NH$(CH_2)_2NH_2$
$\mathbf{A_{Ala,5}}$	H-Ala-Aib-Ala-Aib- Ala-NH$(CH_2)_2NH_2$
$\mathbf{A_{Aib,6}}$	H-Aib-Ala-Aib-Ala-Aib- Ala-NH$(CH_2)_2NH_2$
$\mathbf{A_{Ala,7}}$	H-Ala-Aib-Ala-Aib-Ala-Aib- Ala-NH$(CH_2)_2NH_2$
$\mathbf{A_{Aib,8}}$	H-Aib-Ala-Aib-Ala-Aib-Ala-Aib- Ala-NH$(CH_2)_2NH_2$
$\mathbf{A_{Ala,9}}$	H-Ala-Aib-Ala-Aib-Ala-Aib-Ala-Aib- Ala-NH$(CH_2)_2NH_2$
$\mathbf{B_3}$	H-Gly-Ala- Ala-NH$(CH_2)_2NH_2$
$\mathbf{B_6}$	H-Gly-Ala- Ala -Gly-Ala- Ala-NH$(CH_2)_2NH_2$
$\mathbf{B_8}$	H-Gly-Ala-Gly-Ala- Ala -Gly-Ala- Ala-NH$(CH_2)_2NH_2$

[a]Aib: α-aminoisobutyric acid; Ala: (L)-alanine; Gly: glycine

Table 3-1. Peptide series **A** and **B** studied in this thesis.

Based on such considerations, the series of well-designed peptides were prepared by solid-phase peptide synthesis in solution step by step. The chemical structures are reported in Table 3-1. To ensure helicity, the structure of the peptides A series is constituted by alternating Aib and alanine (L-Ala) amino acids. For the purpose of verifying the role of the helical content in inducing aggregation, we designed a series of analogues (series B) which is constituted by sequences devoid of the Aib amino acid and comprising L-Ala and glycine (Gly). On the other hand, in order to ensure the peptides grafting to the gold surface (see previous Chapter), all peptides feature a free amino group at the N-terminus while the C-terminus has been converted into an amide group by using 1,2-diaminoethane. Accordingly, they present free primary amines both at the N- and C-terminus of the sequence. It is also worth pointing out that, since all peptides have been synthesized starting from the C-terminus, peptide A sequence is characterized by two subsets of peptides: those with an Aib (even sequences: number of amino acids = 2, 4, 6, 8) and those with an L-Ala (odd sequences: number of amino acids = 3, 5, 7, 9) at the N-terminus, labelled with Ala or Aib as subscripts, respectively. The three peptides of the B series all show an L-Ala at the C-terminus and a Gly at the N-terminus. On the basis of what is known in the literature, the peptides of the A series are expected to assume a prevailing helical conformation as the sequence elongates, while for those of the B series no preferred conformation is expected because of the lack of the Aib amino acid.

3.3 Helical conformation of the peptides

Subsequently, in order to assess the conformational preference of the synthesized peptides of the A and B series, we recorded their electronic circular dichroism (ECD) spectra in ethanol at neutral pH (Figure 3-2). In the analysis of the ECD spectra, as expected, peptides A start developing the spectral features of a helical conformation with the pentapeptide [141] indicating that the NH_2 group introduced at the C-terminus does not interfere with the H-bonds network that stabilizes the folded conformation while the spectra of peptides 1 to 4 show weak negative cotton effect above 190 nm, which demonstrates that they are relatively in an unordered conformation. On the contrary, a striking difference exists between the peptides in their helicity when comparing the ECD spectra for B_3, B_6 and B_8 with the corresponding ones of the A series. In fact, the comparison of the ECD

spectra of peptides $A_{Ala,3}$, $A_{Aib,6}$ and $A_{Aib,8}$ with those of the corresponding peptides B_3, B_6 and B_8 are reported in Figure 3-3. The spectra clearly show how the intensity of the negative bands increases with the length of the peptide. Peptides of sequence B do not show the helical signature in their ECD spectra since the oligomers are more likely to exist in random coil pattern. This confirms that the differences in measured electronic circular dichroism are simply on account of the helicogenicity of Aib of peptides A sequence, increasing the amount of helical conformation. This confirms that even a short peptide assumes a helical conformation contrary to what happens with proteinogenic amino acids.

Helical sequences were expected to be the best candidates to crosslink the gold nanoparticles. It should be remembered that the plasmonic coupling of AuNPs has a relationship with the distance between the nanoparticles. The length of the as-synthesised oligomer depends on the reversible equilibrium of the peptides structure between ordered conformation and random coil. The plasmonic coupling of the gold nanoparticles can be hence modulated by changing the particles distance, as plasmonic coupling is favoured at short distance and disfavoured at long distance. Consequently, we were expecting a dependence of the plasmonic coupling on the peptide length and its helical content at the equilibrium.

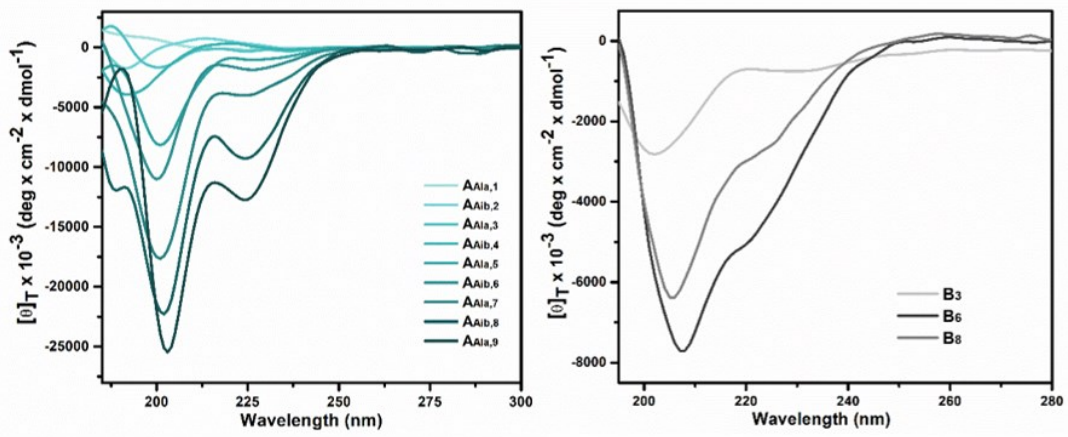

Figure 3-2. Left: ECD spectra of peptides of the A series (Peptides 1-9) in ethanol at 25 °C, Right: ECD spectra of peptides of the B series (B_3, B_6, B_8) in ethanol at 25 °C.

In general, peptides contain predominantly (not exclusively) two types of helical structures: α-helix and 3_{10}-helix, which differ for the pitch of the helix. The experimental evidence indicates that the onset of a helical conformation in an ECD spectrum is

associated with the presence of two minima at ca. 208 and 222 nm. The $\theta_{222}/\ \theta_{208}$ ratio provides an indication of the type and amount of helical conformation present: it is between 0.3 and 0.5 for a 3_{10} helix while it is close to 1 (or even higher) for an α-helix.[139] The concomitant presence of both helices in the same sequence is also possible. Figure 3-3 reports the values of the $\theta_{222}/\ \theta_{208}$ ratio for peptides of sequence A presenting a helical signature. If we take the $\theta_{222}/\ \theta_{208}$ ratio as an indication of the helical content we observe that this value is 0.12 for peptide $A_{Ala,5}$ and reaches the 0.41 value for peptide $A_{Aib,8}$ and 0.49 for peptide AAla,9 which are indicative of a fully formed 3_{10} helical conformation and the presence of the 3_{10}-helix signature for peptides $A_{Ala,5}$ and $A_{Aib,8}$ but not for those of the B series.

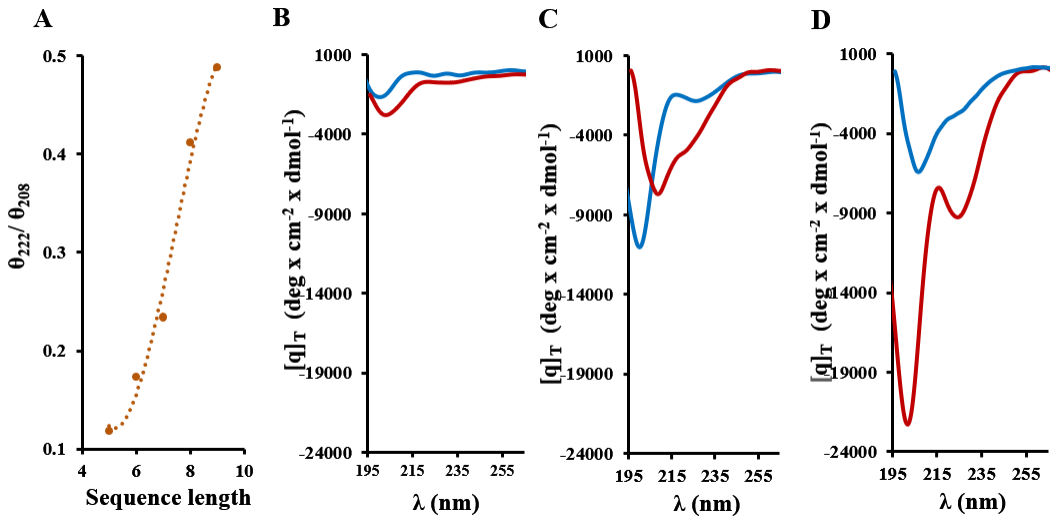

Figure 3-3. Dependence of the ellipticity ratio $\theta_{222}/\ \theta_{208}$ from the number of amino acids in the sequence (A series); the dotted line was added to guide the eye; B-D: Comparison of electronic circular dichroism (ECD) spectra of peptides $A_{Ala,3}$ and B_3 (B) $A_{Aib,6}$ and B_6 (C) $A_{Aib,8}$, and B_8 (D). The blue lines refer to the A series while the red ones refer to the B series.

3.4 Crosslinking assay

3.4.1 Crosslinking experiment

As discussed in the previous chapter, I used ethanol as the solvent for all experiments and "naked" (or citrate-depleted) AuNPs. Apart the consideration made already, this solvent allows one to work at much lower concentrations than those required to induce crosslinking in an aqueous solution and also minimizes unwanted interactions between the

peptides. This observation was confirmed by crosslinking experiment with added water. Moreover, dynamic light scattering (DLS) analysis of solutions of the peptides up to ten-fold the concentration used for the crosslinking experiments did not show any indication of their aggregation in ethanol. The crosslinking ability of the gold nanoparticles, in response to the helical conformation content of the peptides, was investigated by UV-visible analysis in ethanol. Analysis of the UV-visible gives interesting information. The result of the evolution of SPR band and the macroscopic visual results are reported in Figure 3-4. Inspection of the data reveals that a quite different behaviour, depending on the type of sequence A and B, was observed when I added the different peptides (3 μM concentration) to the above solution of AuNPs ([AuNPs] = 7.8×10^{-9} M, A_{515}=0.800). In general, an increasing ability to shift the maximum of the SPR band to longer wavelengths as the sequence elongates (Figure 3-4A) is obtained for the A sequence featuring helicogenic peptides, indicating that they form typical globular aggregates since the spectrum exhibits only one distinct peak in the wavelength range 450-800 nm. This is further supported by transition electron microscopy (TEM) and Dynamic light scattering (DLS) experiments that will be discussed in a subsequent section. Meanwhile, as a function of the number of amino acids in the different sequences, their absorbance at 530 nm and the position of the maximum of the SPR band for all peptides, respectively, are reported in Figure 3-4. On the other hand, the peptides devoid of Aib in the sequence B hardly affected the position of the SPR band contrary to what observed for sequence A (Figure 3-4B). Such observation confirms the plasmonic coupling of AuNPs was induced by helical conformation and indicate that the helical conformation can effectively facilitate the nanoparticles crosslinking. Further evidence for the crosslinking of AuNPs was obtained from the pictures of the cuvettes of these solutions, which showed the development of a violet-bluish color as the sequence elongates for the A series (Figure 3-4). This is an indication of the presence of the plasmonic coupling not observed for the B sequence. It is known that water interacts more strongly with the AuNPs surface than ethanol thus competing with the weak amine ligand.[15] To demonstrate the crosslinking is inhibited by water, an ethanol solution with just 5% (v/v) of water was used. UV-visible spectroscopic analysis showed that a much larger concentration of peptide was required to induce the crosslinking of the AuNPs (Figure 3-4 and Figure 3-5). This observation indicates the

presence of trace amount of water would remarkably hamper the aggregation of nanoparticles.

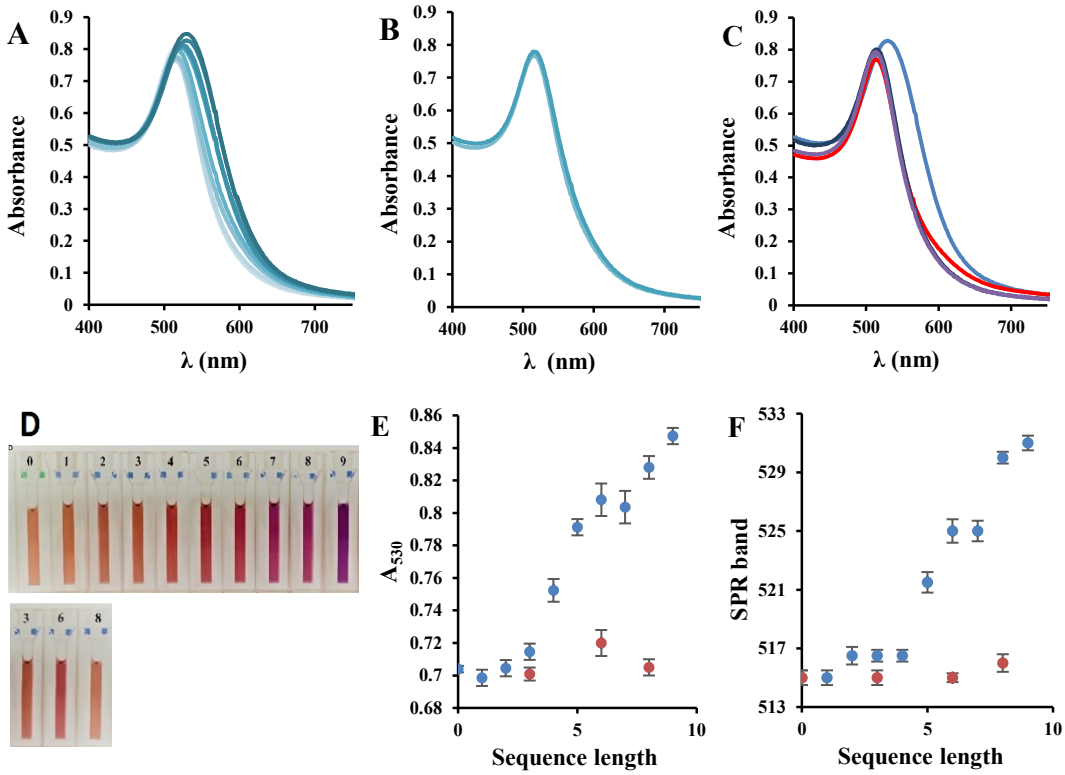

Figure 3-4. Spectra of the SPR region of AuNPs treated with the peptides of the **A** series (**A**) and **B** series (**B**) in ethanol: from lighter to darker color as the peptide length increases. **C**: spectra of the SPR region of AuNPs treated with peptide $\mathbf{A}_{\mathbf{Aib,8}}$ in ethanol, blue line, and ethanol with 5% water (red line); the violet and underneath green lines are those of the solution with only AuNPs in the two solvents. **D**: Picture of the cuvettes of the solutions of AuNPs used to record the spectra reported in A (top) and B (bottom); the number on top of each cuvette indicates the number of amino acids in the sequence. **E**: Absorbance at 530 nm of the AuNPs solutions treated with peptides of the **A** (blue) and **B** (red) series. **F**: Position of the maximum of the SPR band for the peptides of the **A** (blue) and **B** (red) series (in both cases error bars are averages of three independent measurements). For all solutions [AuNPs]= 7.8×10^{-9} M and [peptide]= 3 μM.

As a last consideration it must be noted that the differentiation in crosslinking ability of the AuNPs by peptides of the A series is, obviously, concentration-dependent and the 3 μM concentration I have used represents the optimum condition I have found for their differentiation. As the concentration of the helical peptide increases up to 3 μM so does the shift of the SPR band. However, at higher concentration (5 μM) the shift decreases (Figure 3-6). I explain this with the fact that we are approaching the saturation of the AuNPs surface. Crosslinking can only occur when the peptide finds an empty space on the surface

of another nanoparticle, a situation that does not occur when the total passivation of the surface is approaching (and beyond).

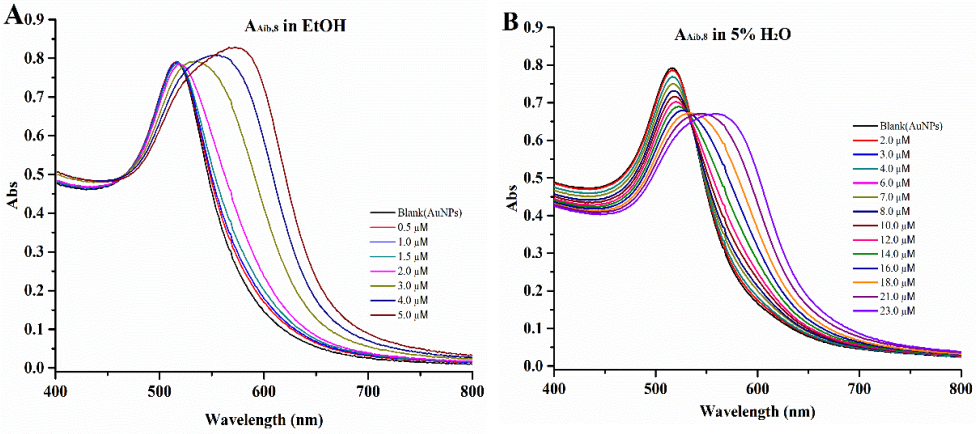

Figure 3-5. Spectra of the SPR region of AuNPs solutions recorded at increasing concentration of peptide $\mathbf{A}_{\mathbf{Aib,8}}$ recorded in EtOH (**A**, [$\mathbf{A}_{\mathbf{Aib,8}}$] = 0-5 μM) and EtOH/5%$H_2O$ (**B**, [$\mathbf{A}_{\mathbf{Aib,8}}$] = 0-23 μM).

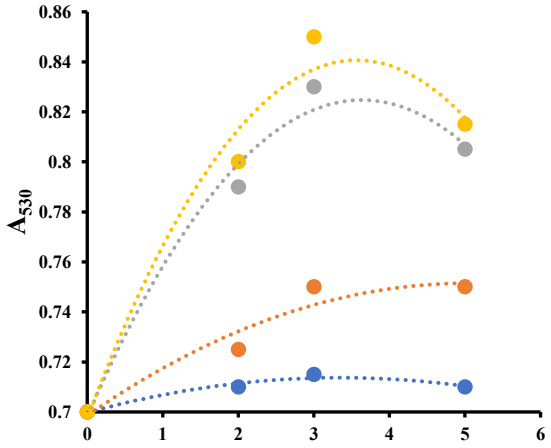

Figure 3-6. Absorbance at 530 nm of the SPR band of the nanoparticles as a function of the peptide concentration (μM). Dotted lines have been arbitrarily drawn to guide the eye. Blue circles: tripeptide; orange: tetrapeptide; gray: octapeptide; yellow: nonapeptide.

3.4.2 Characterization of the AuNPs aggregates

As a further analysis in support of the formation of aggregates, beside the spectroscopic studies, transition electron microscopy (TEM) and dynamic light scattering (DLS) experiments were carried out on all samples. The TEM analysis requires the sample to be desolvated once deposited on the carbon-coated copper mesh grid used. This may induce aggregation regardless the nanoparticles are aggregated or not in solution. DLS, on the

other side, determines the size of the particles in solution with bimodal size distributions if clusters are present. The analysis of the TEM data (Figure 3-7) reveals that, of the total nanoparticles present in the images collected for the different peptides, the averages size of the clusters is 10-20 nanoparticle for the short peptides (up to the tetrapeptide) and all non-helical peptides and becomes >130 for the octa- and nonapeptides $A_{Aib,8}$ and $A_{Ala,9}$ (Figure 3-8).

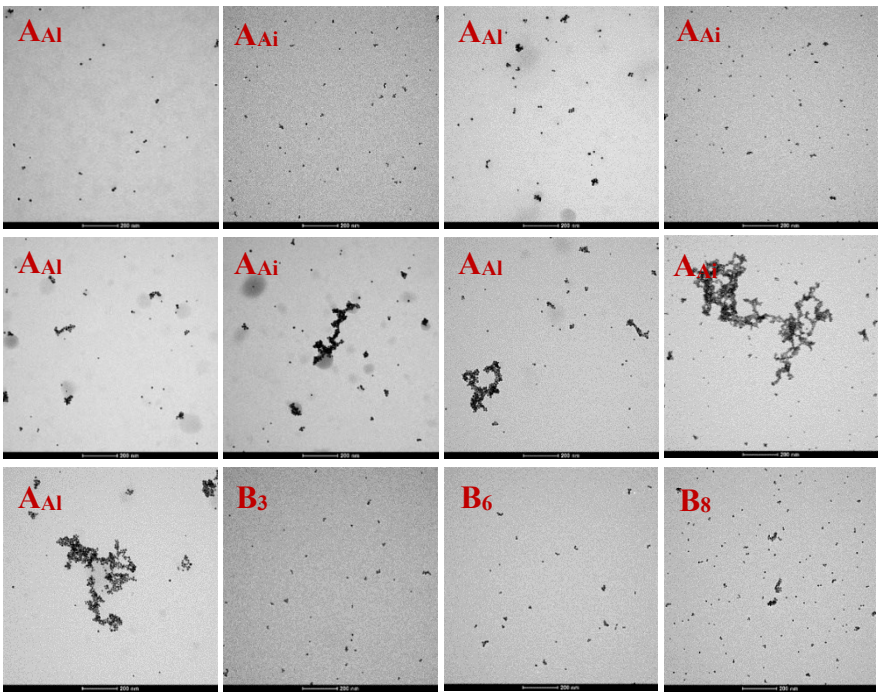

Figure 3-7. TEM images of AuNPs treated with 3 μM of peptides **A** series and **B** series in EtOH.

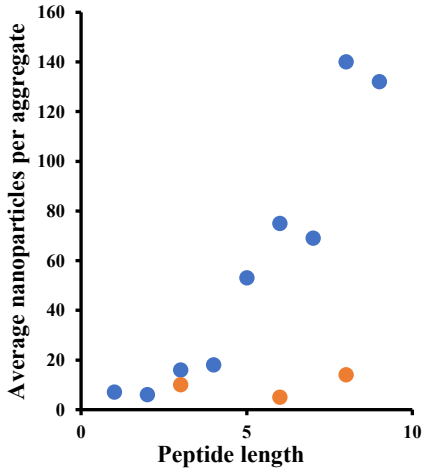

Figure 3-8. Average number of AuNPs per aggregate obtained from the TEM images (>2,500 nanoparticles counted) versus the number of amino acids in the sequence. Blue points are for the helix-folding peptides; orange points are for the random-coil peptides.

The DLS data (Figure 3-9) also indicate the formation of aggregates although much smaller than those present in the corresponding TEM pictures. For the above octa- and nonapeptides the hydrodynamic diameter is 22.6 and 27.5 nm. Assuming a globular aggregate constituted by 10-nm nanoparticles (the gold core and the crosslinking peptide) this would indicate the formation of aggregates of ca. 5 and 10 nanoparticles upon addition of the two peptides, respectively. These values are consistent with what theoretically predicted [45] on the basis of the SPR shifts observed and experimentally reported when the aggregates formed were proven to be globular.[142, 143] Clearly the TEM data reflect also the contribution of unspecific aggregation and the information they provide is only on the tendency of the different samples to aggregate but not on the real size of the aggregates formed. In any case both studies reveal that the aggregation starts becoming relevant only with the pentamer of the A-series sequence and is irrelevant when the B-series peptides are added to the nanoparticles. As discussed above, the ECD spectra indicate that a structured sequence starts forming with peptide $A_{Ala,5}$ onward. Consequently, I can safely state that the onset of a helical conformation and the shift of the top equilibrium of Figure 3-1 to the right, as the peptide sequence A becomes longer, is associated with an increase of the shift of the SPR band of the AuNPs and their aggregation.

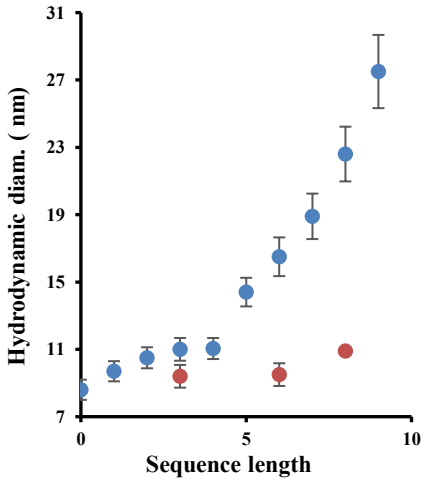

Figure 3-9. Dependence of the average hydrodynamic diameter of the clusters of AuNPs as a function of the number of amino acids in sequence: peptides A, blue symbols; peptides B, red symbols. Notice that error bars increase with the apparent size of the cluster because of the coexistence of clusters of different sizes.

3.5 Thiol-triggered reversion of aggregation

The thiol-triggered reversion of aggregation was examined using UV-visible spectroscopy and N-acetylcysteine methyl ester as a competing agent. My assumption was that the nanoparticles aggregation was driven by the interaction of the AuNPs and the amino groups present on both ends of the peptides. Accordingly, the much stronger interaction Au-S would easily replace the peptide from the gold nanoparticles surface leading to AuNPs disaggregation. The reversion experiment was performed by adding a 10-fold excess of N-acetylcysteine methyl ester to a solution of the AuNPs previously treated with 3 μM $A_{Aib,8}$ in ethanol. The UV spectra were recoded for several minutes to make sure the reversion process was complete (Figure 3-10). The solution became ruby in color from a violet-bluish and no precipitate was observed up to 6 hours. UV-visible spectra revealed that the SPR band had reverted to the original position with a slow exchange rate, which suggests that the peptide was indeed detached from the gold surface and a new Au-S bond formed. When "naked" gold nanoparticles were treated with the same amount of thiol and the solution was left standing for the same time as in the previous reaction no aggregation neither precipitation was observed, confirming the AuNPs were very stable in the presence of thiol. The slow rate of the reversion of aggregated AuNPs to monomers is well known and has been reported also with other systems.[144]

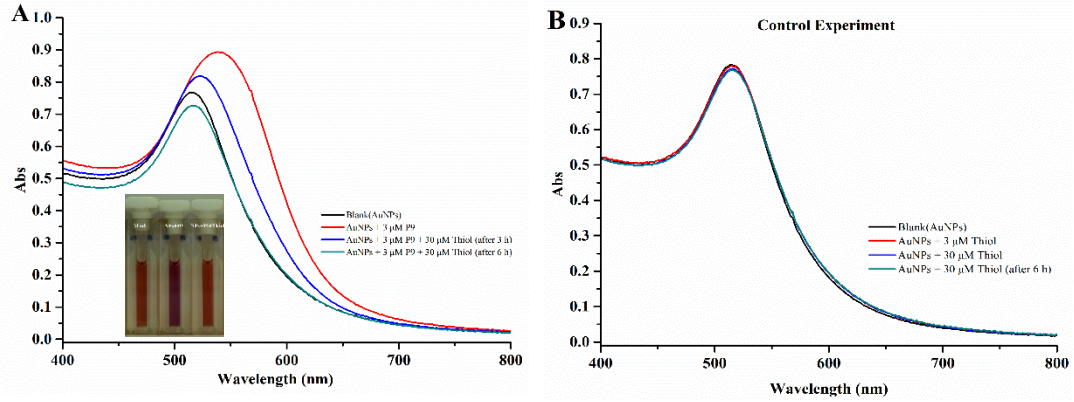

Figure 3-10. Left panel: spectra of the SPR region of AuNPs in ethanol after crosslinking with peptide $A_{Ala,9}$ and addition of N-acetyl cysteine methyl ester at different times. The inset shows the pictures of the cuvette before the addition of the peptide, after its addition and, eventually, after the further addition of the thiol (A). Right panel: Effect of the addition of the thiol to the SPR band of the AuNPs (B).

3.6 Temperature controlled aggregation

Subsequently, we investigated the ability to control, in response to the temperature, the aggregation of AuNPs. The peptide $A_{Aib,6}$ and $A_{Ala,9}$ were incubated at 65 °C for 10 minutes, after that the ECD spectroscopy at that temperature displayed dichroic signals with total ($A_{Aib,6}$) or partial ($A_{Ala,9}$) disappearance of the helical signature. However, upon cooling the solution to 25 °C the dichroic signal returned to the original shape and intensity, suggesting that at low temperature the helical conformation was established again without racemization of the amino acids at high temperature. The only partial denaturation of the nonapeptide is hardly surprising in view of the very high stability of Aib-rich sequences.[145] To obtain a further confirmation that the crosslinking was directly connected to the helical content of the peptides we performed an experiment in which the peptides were preincubated at 65°C for 30', and subsequently added to the AuNPs kept at this same temperature. UV-visible spectroscopy confirmed that crosslinking ability was significantly decreased ($A_{Ala,9}$) or fully suppressed ($A_{Aib,6}$) (Figure 3-11). Upon cooling the solution to 25°C, the original crosslinking ability was repristinated. Afterwards, another control experiment using a fluorescent-tag-labelled primary amine showed that the change of temperature does not cause the detachment of the amines from the AuNPs surface. The observations suggest that the helical/random coil conformations can reversibly be switched moving from low temperature to high temperature and vice versa. This temperature-controlled process has the ability to control the aggregation of the AuNPs.

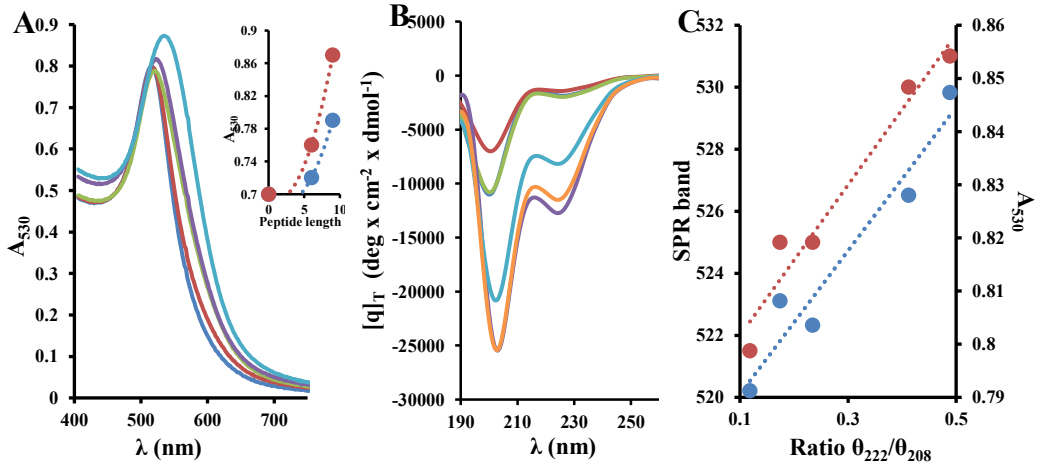

Figure 3-11. **A**: SPR band region for peptide $\mathbf{A_{Aib,6}}$ recorded at 65°C (red curve) and after cooling to 25°C (green curve, partly hidden by the violet one) and peptide $\mathbf{A_{Ala,9}}$ recorded at 65°C (violet curve) and after

cooling to 25°C (light blue curve). The blue curve represents the untreated AuNPs. Inset: absorbance at 530 nm at 65° (blue symbols) and after cooling to 25° (red symbols) for the two peptides. **B**: ECD spectra of peptide $\mathbf{A_{Aib,6}}$ (shallower bands) recorded at 25°C (blue partly hidden by the green one), 65° (magenta) and back to 25° (green) and peptide $\mathbf{A_{Ala,9}}$ recorded at 25°C (violet), 65° (light blue) and back to 25° (orange). **C**: Correlation of the shift of the maximum of the SPR band of the AuNPs in ethanol (red symbols, left axis, R = 0.955) and the absorbance at 530 nm (blue symbols, right axis, R = 0.935) with the helicity parameter $\theta_{222}/\theta_{208}$ for peptides $\mathbf{A_{Ala,5}}$, $\mathbf{A_{Aib,6}}$, $\mathbf{A_{Ala,7}}$, $\mathbf{A_{aib,8}}$, and $\mathbf{A_{Ala,9}}$. The dotted lines represent the linear fitting of each set of points.

3.7 AuNPs aggregation and helical content of the peptides

It is well known for α,α-disubstituted amino acids-containing peptides that, as the sequence elongates, the introduction of one of them increases helicity much more than what a proteinogenic one does, because of their strongly helicogenic nature.[139, 146-149] AuNPs are so sensitive to the amount of helical content of the sequence of peptides A examined that, as shown in Figure 3-4E, F, the shift of the band and the increase of the absorbance at 530 nm are relatively more pronounced for peptides $A_{Aib,6}$ and $A_{Aib,8}$ than for peptides $A_{Ala,7}$ and $A_{Ala,9}$, i.e. in concomitance with the introduction of an Aib amino acid at the N-terminus. Analogously, the shift of the SPR band by going from peptides $A_{Ala,5}$ and $A_{Ala,7}$ to the next ones ($A_{Aib,6}$ and $A_{Aib,8}$) is larger than what observed when increasing the length from peptide $A_{Aib,6}$ to $A_{Ala,7}$ and from $A_{Aib,8}$ to $A_{Ala,9}$, respectively. The correlation between AuNPs aggregation and helical conformation is impressive. Plots of the shift of the λ_{max} of the SPR band and its A_{530} show fairly good linear correlation with the helicity parameter $\theta_{222}/\theta_{208}$ (Figure 3-11B) in strong support that the aggregation process I was monitoring is related to the helical conformation assumed by the peptide as its number of amino acids increases. It should also be pointed out that, as the peptide elongates and its helical content increases (starting with peptide $A_{Ala,5}$) the distance between the two amines also increases. It is known that the effect on the shift of the SPR bands decreases as two interacting nanoparticles are more distant one from another.[45, 46] Since the pitch of a 3_{10} helix (occurring at amino acid i and i+3) is 6.3 Å, we infer that the distance between the N- and C-terminus amines would increase from ca. 0.7 nm in peptide $A_{Ala,5}$ to ca. 1.5 nm in peptide $A_{Ala,9}$ for such a helical conformation. This would result in a decrease of the shift of λ_{max} of the SPR band. The fact that this doesn't occur indicates that the increase of the distance is more than compensated by the increase of helical content of longer peptides connected to their increased crosslinking ability.

3.8 Conclusion

In summary, I have reported compelling evidence that a peptide, functionalized with primary amines both at the C- and N-terminus is able to induce the crosslinking of AuNPs in ethanol, following its helical content. Helical sequences induce aggregation while non-helical ones are poorly effective on this regard. Accordingly, the crosslinking of the 10-nm nanoparticles I have used is strongly dependent on the helical content of a peptide sequence or, said in other words, helicity of the peptides controls the aggregation of the AuNPs. Induction of helical conformation by interaction of a peptide with AuNPs has been reported as well as the use of designed peptides to induce crosslinking.[150-155] However, this is, to the best of my knowledge, the first evidence concerning the correlation between crosslinking ability of a properly functionalized peptide and its helical content. Obviously, the constituent amino acids of the peptides cannot contain lateral functional groups able to interact with the AuNPs surface by themselves. I envision the possibility that also other oligomers, in equilibrium between a properly ordered and random coil conformation, could be able to control AuNPs aggregation following their unordered or ordered state. Overall, from the above investigation, I have found that the interaction of biomolecules with AuNPs is very interesting. The binding process not only provides a wealth of information about the linker structure, but also defines the aggregates pattern, that inspired me to study how the conformation of the biomolecules controls the crosslinking. The next goal I wanted to pursue was the design of a linker capable of favouring a different shape of the aggregates with respect to the globular ones I have found here, i.e. the formation of linear crosslinked gold nanoparticles. In the next chapter I will report how this goal was successfully achieved.

Chapter 4. Glucosamine phosphate induces AuNPs aggregation and fusion into easily functionalizable nanowires

4.1 Introduction

In the previous chapter I have shown how the aggregation of AuNPs into clusters can easily be achieved by using a bifunctional crosslinker. I have also reported evidences showing that the aggregation occurs more easily in an organic solvent (like ethanol) than in water because of the higher solvation power of pure water to ions, and the higher affinity H_2O has for the gold surface of the nanoparticles.[125]

One-dimensional (1D) assembly nanostructures represent an important class of supramolecular systems, finding various application such as electronic and sensing devices. Recent developments have seen the incorporation of controllable self-assembly processes into "soluble" or dispersible nanoparticles leading to the emersion of impressive new nanoscale properties such as distinct optical, magnetic, and electrical properties. For several important applications like, for instance, surface-enhanced raman scattering (SERS) for diagnostic purposes [156] or thermal therapy in nanomedicine [157] because tissues absorb less in the near infrared (NIR) region, it would be desirable to further red-shift the SPR band of aggregated AuNPs. In the previous section we have seen that the SPR band is not much shifted when the aggregate is globular. However, a necklace aggregate (see Chapter 1) develops a new band at longer wavelengths. The extent of the shift depends on the length of the aggregate and, very importantly, on the distance between the nanoparticles, the closer they are the more red-shifted is the band.[158] The shift of the plasmon resonance band beyond 700-750 nm can only be obtained by fusing the nanoparticles into a nanowire.[159] It is well known that the plasmon band of gold nanorods red-shifts with the increase of the aspect ratio.[160] In fact, nanowires (NWs), depending on their length, absorb well within the NIR region.[157, 161]

AuNPs, as a mostly spherical particle, tends to aggregate in an uncontrolled pattern and it is a major challenge to facilitate the formation of anisotropic assemblies. Nevertheless, several groups have reported successful results in the directional assembly of AuNPs. This has helped to establish distinctive properties of these systems. Thus far, the current

strategies for 1D nanoparticle chains formation belongs to two general categories: i) the linear-template method, which is based on the use as templates of linear scaffolds like polymers, biomolecules (such as DNA), modified carbon nanotubes; ii) the template-free self-assembly method, which mainly relies on magnetic and/or electric dipole moments, oriented aggregation. These strategies appear to be suitable to efficiently manipulate the two or more nanoparticles assembly into a well-defined 1D chain, but the design of dimensional templates usually requires implementation of suitable linear structure which need large effort to build and evaluate. Moreover, most of the several "wet" conditions for the preparation of nanoparticle chains use amphiphilic molecules like oleylamine [162, 163] or cetyltrimethylamminium bromide.[164] For biological applications, these protocols pose a serious problem of contamination of the nanostructure due to the toxic cationic additives used for their preparation.[165] With this in mind, small chemical molecules appear a better choice. However, only a few cases have been described that control of the nanoparticles assembly into well-defined superstructures. In fact, the typical synthetic procedures when performed with a defect of the reducing/capping agent also lead to an ordered nanostructure.

In this chapter I will report the gold nanoparticles assembly into nanowires under very mild conditions. My results are based on the serendipitous observation that the addition of glucosamine phosphate (GAP) to AuNPs led to the growth and fusion of them into nanowires. I was looking for a mild passivating agent to replace citrate [15] in AuNPs. However, the presence of the glucose moiety on GAP, as I will show below, resulted in a cascade of redox processes [166] starting with AuNPs aggregation in a linear fashion and ending with their fusion into nanowires.

4.2 Preparation of the AuNPs

The first objective was to synthesize AuNPs for the eventual preparation of linear aggregates formation. The starting point of this investigation was to find a mild capping agent for AuNPs that can interact with AuNPs and could allow them to remain stable in solution without aggregation even when used in stoichiometric concentration to passivate the nanoparticle surface. Fortunately, we realized that the glucosamine phosphate (GAP, Figure 4-1) proved suitable for this purpose. Indeed, under these conditions (i.e., [GAP] ≥

[$Au_{surface}$]) AuNPs are stable as can be judged by the intensity and position of the SPR band monitored over several days. Phosphonic acid derivatives bearing an amino group like aminomethylphosphonic acid are mild passivating agents of AuNPs [167] and GAP behaves in a similar way. It appears to be able to passivate AuNPs by interacting with the gold surface more strongly than citrate because of the presence of the amino group.[127] However, when GAP is used under substoichiometric concentrations, i.e., at a concentration lower than that of the free Au atoms present on the surface of AuNPs, a slow aggregation process of the nanoparticles occurs that evolves into the formation of nanowires. As I will discuss below the glucose moiety of GAP is necessary for the final outcome of the process. Oxidation of glucose to gluconic acid under aerobic conditions in the presence of AuNPs was first reported by Rossi et al.[168] They observed a steady growth of nanoparticles during the process. It was later discovered [169] that hydrogen peroxide was also formed in addition to gluconic acid.[166, 170] Hydrogen peroxide is known to be able to reduce Au(III) and Au(I) to Au(0) in the presence of the AuNPs.[166] All the above processes are involved in the formation of nanowires from AuNPs as I am going to discuss.

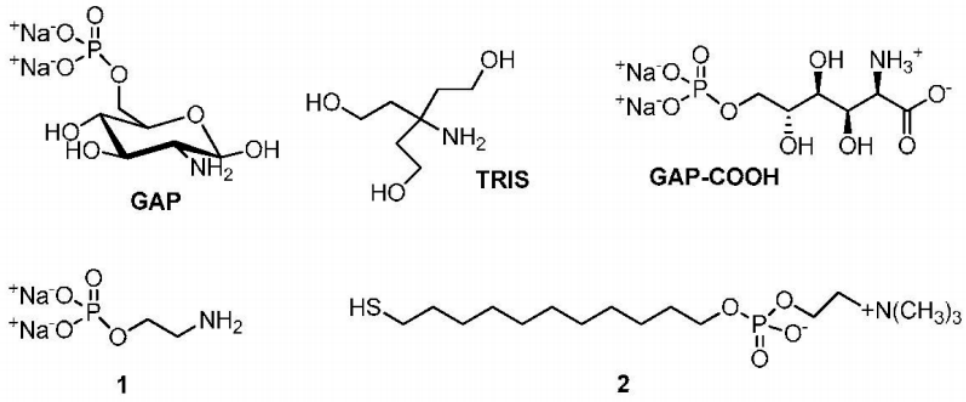

Figure 4-1. Compounds discussed in this work.

On the basis of above analysis, I started to prepare the purified AuNPs as described in Chapter 2 by reduction of gold(III) with citrate. However, in this case, before citrate depletion, GAP was added. Thus, an aqueous solution of 1 ml of GAP (8 mg, GAP per Au free atoms) was added to the citrate-passivated AuNPs solution and the solution was left to stir at room temperature for 10 min. The final concentration of GAP was 25 μM. Free molecules in solution were removed by using 15 mL Amicon® Ultra filters of 100 KDa molecular weight cut-off centrifuged for 2.5 min at 2000 rpm. Purification was repeated twice. The purified AuNPs were characterized by TEM, displaying the size is 9.5 ± 1.5 nm.

TGA (Figure 4-2) analysis revealed that the amount of organic material remaining after the washing cycles was slightly affected by the addition of GAP (from ca. 30% to 45% of the gold atoms on the surface of the nanoparticles). The Zeta potential of the as-prepared AuNPs was -25.5 mV while that of "naked" ones dropped to -2.5 mV. My estimate is that [GAP] final is 4-5 μM based on the TGA data. This amount provided the best performance for the preparation of the nanowires.

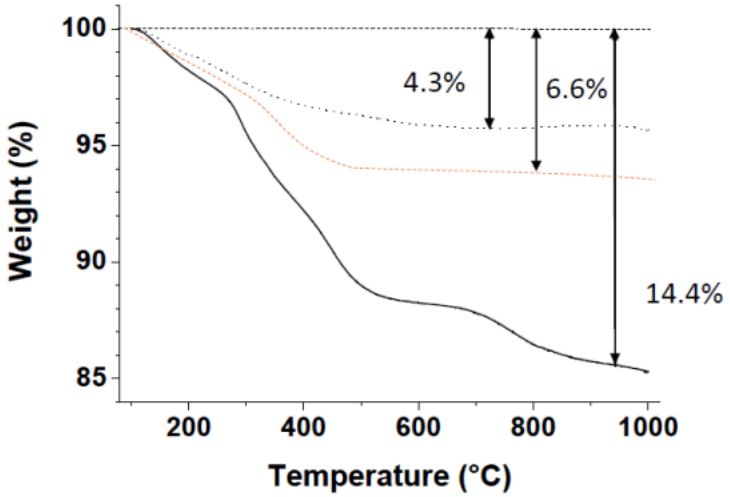

Figure 4-2. Thermogravimetric analysis (TGA) of the citrate-passivated AuNPS (solid line); citrate-depleted AuNPs with no GAP added (dotted black line); citrate-depleted AuNPs with GAP added (dotted orange line).

4.3 GAP-induced aggregation and NWs formation

The AuNPs I prepared were stable under the preparation conditions ([sodium citrate] = 6.8×10^{-3} M) for prolonged times as discussed in Chapter 2. However, when most of the capping agents was removed (citrate-depleted AuNPs) the AuNPs started very slowly to cluster [171, 172] as can be seen in the absorbance spectrum (slight increase of absorbance >600 nm in Figure 4-3B) and increase in size (increase in absorbance at 525 nm in Figure 4-3B and TEM image in Figure 4-3C). Clearly, under these low passivation conditions, Ostwald ripening cannot be prevented.

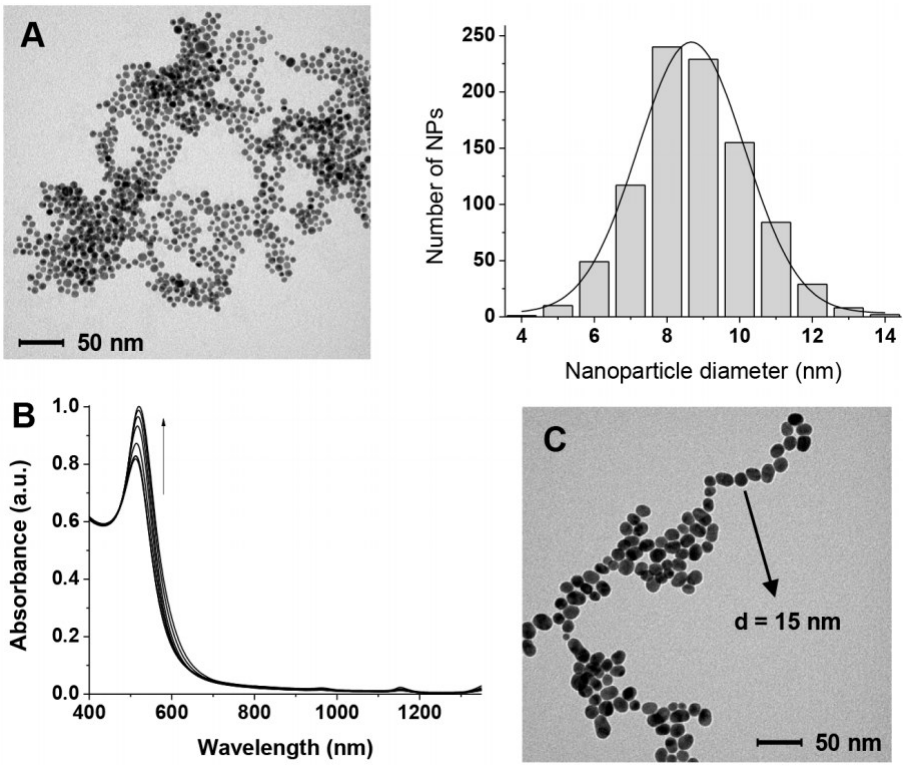

Figure 4-3. (A) TEM image and size distribution of the AuNPs used in this work passivated with citrate; (B) Evolution with time of the UV-visible spectrum in the plasmon resonance region of the AuNPs after citrate depletion (over 7 days, curves were recorded at 1-day intervals); (C) TEM image of the citrate-depleted AuNPs after 7 days (notice the same scale bar as in (A)).

On the other hand, if GAP is present in the "citrate depleted" AuNPs I observed not only the growth in size of the nanoparticles (Figure 4-4B) but also a relatively faster aggregation process (from days to hours) leading to necklace-like aggregates as revealed by the formation of an additional absorption band at 650–680 nm (Figure 4-4A, traces in red). This aggregation process only occurs when substoichiometric amounts of GAP are added. After longer times (days) this band broadens and shifts to longer wavelengths up to >1200 nm (Figure 4-4A, traces in blue). Throughout the experiment, the solution pH remains constant at 6.5 to make sure the aggregation process occurred under the same condition. Further evidence supported by TEM images taken at different time intervals revealed the formation of nanowires of increasing length resulting from the fusion of the formed necklace-like aggregates (Figure 4-4C-E). Moreover, the aggregation and fusion processes could be also followed by the naked eye as can be seen in Figure 4-5. This observation

suggest that the GAP possess the ability to passivate the AuNPs and form linear aggregates in aqueous solution.

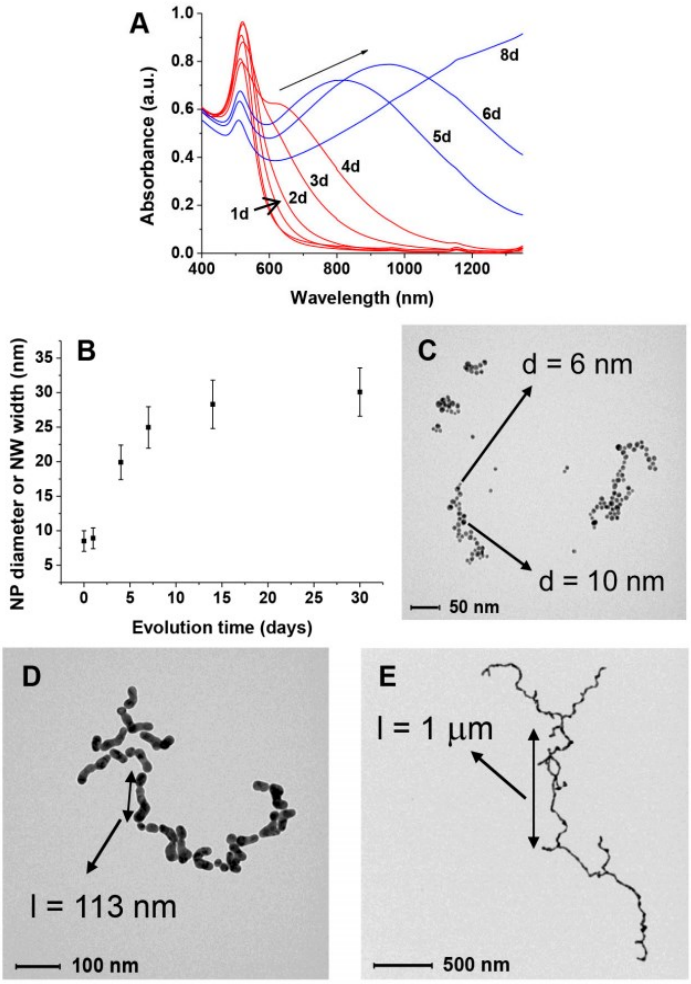

Figure 4-4. Behavior of citrate-depleted AuNPs in the presence of GAP: (A) evolution of the UV-Vis spectrum with time. In red, necklace formation, in blue, nanoparticle fusion; (B) increase in size of the AuNPs or nanowires width with time; (B-D) TEM spectra taken at increasing times (C) 1day; (D) 4 days; (E) 8 days).

As a matter of fact, the two processes (aggregation and fusion) were not fully separated. I observed that some fusion already occurs after four days. Very interestingly, if aliquots of the solution were collected at different time intervals and treated with thiol **2** (Figure 4-1) the obtained NWs were "frozen" and prevented from any further growth. These passivated nanowires could be lyophilized and redissolved showing a spectrum identical to the one recorded at the time of the thiol addition. The only relevant difference was a decrease of the intensity of the longer wavelength band in part associated with the passivation process (Figure 4-6). TEM analysis of these samples (Figure 4-7) reveals NWs

characterized by a broad-length distribution. The average aspect ratio of such nanowires increases with the time allowed for the original AuNPs to evolve, prior to the addition of thiol **2** (Table 4-1). At variance with nanorods that show relatively narrow SPR bands depending on their aspect ratio, these nanowires present rather broad SPR. This is the result of the coexistence of several plasmon modes related to the broad distribution of their length and the existence of branching points (clearly visible in Figure 4-4D,E).[157]

Length/nm	**Width/nm**	**Aspect Ratio**	**λmax**
59 ±29	21±3	3±1	634 nm
269±112	24±3	11±4	952 nm
988±212	26±4	38±12	1350 nm

Table 4-1. Dimensions of the nanowires after stoping the AuNPs aggregation and fusion at difference times and the maximum of the longer-wavelength plasmon resonance band.

Figure 4-5. Change of color of the different AuNPs preparations with time. Timescale in days.

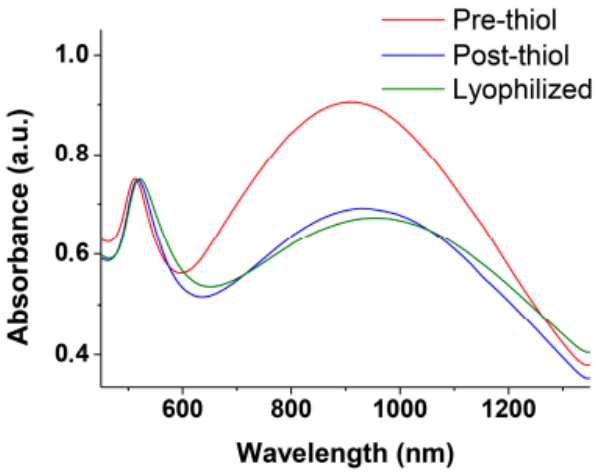

Figure 4-6. Vis-NIR spectra in the plasmon resonance region of nanowires before passivation with thiol **2**, immediately after the passivation with thiol **2** and after lyophilization and redissolution in water.

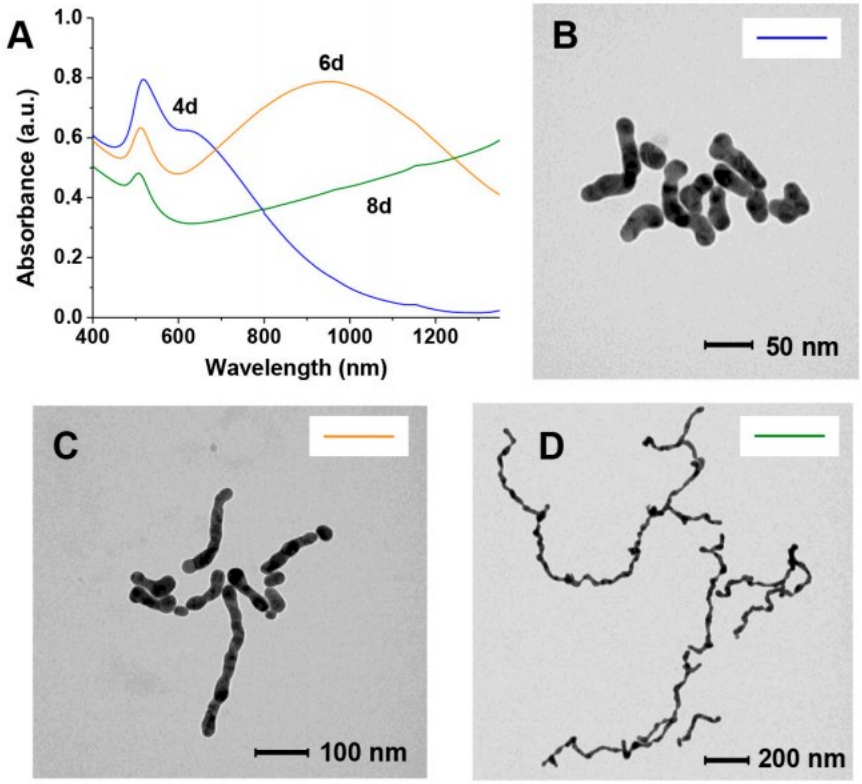

Figure 4-7. Absorption spectra (A) and TEM images of samples collected after (B) 4 days, (C) 6 days, or (D) 8 days and passivated with thiol **2**. The color of the line in the inset in each TEM image links it to the corresponding UV-Visible spectrum in A.

4.4 Analysis of the different processes occurring and the role of GAP

4.4.1 The role of GAP

The above experimental results indicate that the aggregation of the AuNPs only occurs when the surface Au atoms are not fully passivated either by citrate or GAP. Here, I noted that ca. 5 μM GAP is still present in the "citrate depleted" AuNPs, and the concentration of the surface Au atoms of these 9 nm AuNPs is ca. 30 μM. This suggests that the amount of GAP is ca. 18% of that required to fully saturate the nanoparticles surface. Incidentally, this GAP concentration is also the optimum one required for crosslinking of similarly citrate-depleted AuNPs by using amino acids.[67] In particular, the group with the strongest affinity for AuNPs among those present on GAP is the primary amine. As I have shown in Chapter 3 the passivation of AuNPs by amines does occur, although leading to less robust nanoparticles than those passivated with thiols.[31, 173, 174]

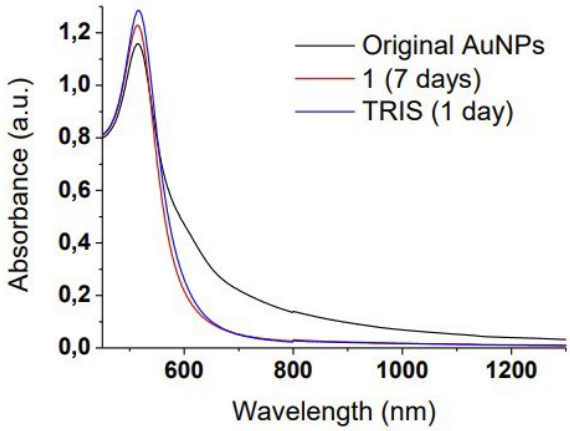

Figure 4-8. Effect of addition of 1 (incubated for up to 7 days) or TRIS (1 day) to AuNPs. 1. The reference (black) curve refers to the citrate-depleted AuNPs devoid of any additive after 7 days.

What is the other functional group responsible for the crosslinking? Notably, those present on the structure of GAP, apart from the amine, are the sugar hydroxyls and the phosphate groups. O-phosphorylethanolamine (**1**, Figure 4-1) is an amino phosphate devoid of the sugar moiety. I therefore set out an experiment to investigate if it would be possible to form nanowire when GAP is replaced by **1**. The UV-visible spectra obtained (Figure 4-8) displayed a distinctive peak in the region of 400-800 nm which corresponds to a very small AuNPs growth and no aggregation at all. Taking into consideration the hydroxyls group it could be possible it is able to induce the crosslinking process. To evaluate this possibility, tris(hydroxymethyl)aminomethane (TRIS) presenting amino-alcohols [45] was added to the AuNPs solution. It induces very limited linear aggregation towards necklaces that do not evolve into nanowires (Figure 4-8). This observation indicates that neither the hydroxyls nor the phosphate present on GAP appear to be involved in the crosslinking process. On the basis of these results, I hypothesized that, as is shown below, a new functional group is formed during the early steps of the overall process: a carboxylate. This is responsible for the aggregation in a process not much different from that observed with some amino acids.[67]

4.4.2 The role of glucosamine

To gain insight into the driving force of nanowire formation, I started a program of detailed analysis the role of GAP. All experimental evidence pointed to a critical role played by the glucose subunit present in GAP. It is known that glucose is involved in

several redox processes in the presence of Au(I) or Au(III) ions and AuNPs, as well. The $HAuCl_4$ could be reduced into AuNPs in the presence of glucose.[168] The AuNPs, once formed, oxidize glucose to gluconic acid while reducing O_2 to H_2O_2.[15, 169, 170] Furthermore, H_2O_2 is also able to reduce $AuCl_4^-$ to Au(0).[175-177] The oxidation of GAP was demonstrated in our case by analyzing the organic component of AuNPs passivated with an excess of GAP. To demonstrate this possibility, excess of GAP was added to the AuNPs solution, under these conditions, obviously, the AuNPs do not crosslink but the amount of GAP is such to allow its quantification with time. The evidence of the composition of the organic component of the AuNPs solution after several days can be obtained from the ^{1}H-NMR spectroscopy (Figure 4-9), which revealed the disappearance of the signals amenable to GAP and the appearance of signals pertaining to the oxidized glucosaminic acid phosphate (GAP-COOH) derivative. Thus, during this time, GAP is oxidized to GAP-COOH. Considering the oxidation process was carried out in a non-controlled atmosphere, it would be possible to prevent the crosslinking by treatment with depletion of O_2 from the system. The evidence supported by the UV-visible spectra that GAP behaves in the very same way as **1** does (Figure 4-10) and aggregation is not observed in the absence of O_2. All the above results indicate that GAP-COOH, at low concentration, is responsible for the linear aggregation of the nanoparticles. This implies that a carboxylate group has a higher affinity for the nanoparticle surface than a phosphate group. The aggregation is hence indirectly initiated by a redox process requiring both the glucose moiety of GAP and O_2.

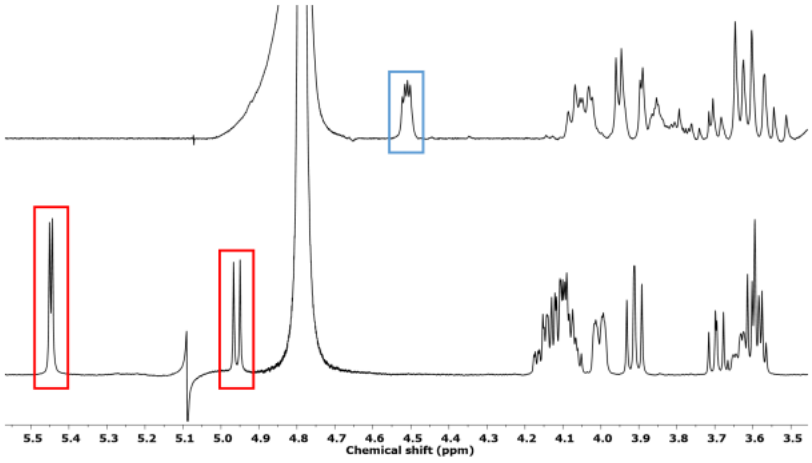

Figure 4-9. ^{1}H-NMR spectra (D_2O) of GAP (bottom) and the filtrate of a GAP solution in the presence of AuNPs after 2 weeks. Signals corresponding to the α and β anomers of GAP are highlighted with red boxes whereas H-2 of the oxidized form is shown inside a blue box.

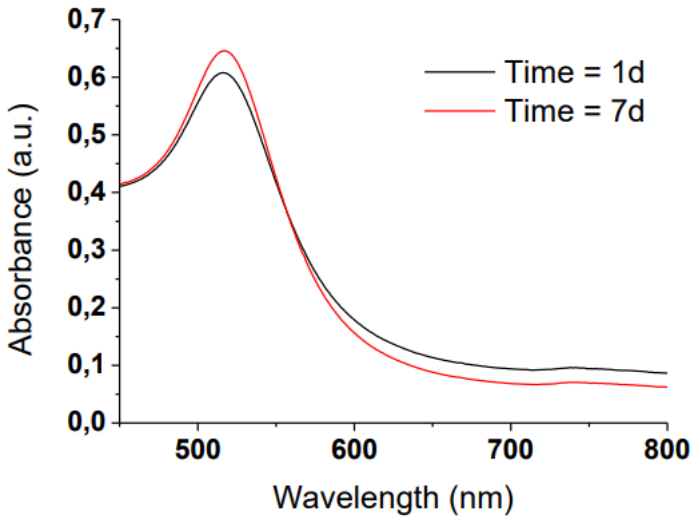

Figure 4-10. UV-Vis spectra of AuNPs treated with GAP in the absence of O_2 after 2 and 7 days.

4.4.3 The overall process

Taken together, the overall process of formation of the nanowires comprised the following steps: (i) the AuNPs growth and oxidation of GAP to GAP-COOH; (ii) the formation of necklace-like aggregates; (iii) the fusion of the aggregates into nanowires. The initial growth of the original nanoparticles (Figure 4-4B) is a well-known phenomenon reported for poorly-passivated gold nanoparticles.[178] AuNPs growth leads to the decrease of their overall surface area and, hence, the amount of passivating GAP and GAP-COOH required for their stabilization is also lower. Furthermore, larger nanoparticles are less prone to aggregation and subsequent coalescence.[178] Both these points explain why the growth of the nanoparticles, which reflects on the width of the final nanowires, stops at ca. 25 nm from the 9 nm diameter of the original ones. I observed that nanoparticles growth is fast at the early stages of the process while it slows down considerably with time (Figure 4-3B). However, the key question still in my mind is what leads to nanoparticle fusion once the linear aggregates are formed. It has been reported that AuNPs prepared by citrate reduction of $HAuCl_4$ followed by further reduction with $NaBH_4$ still contain ca. 4% Au(I).[124] I speculated that the amount of Au(I) would be expected to be larger in the absence of the final $NaBH_4$ reduction, as in my synthetic protocol. Thus, I performed an experiment on the as-prepared AuNPs in the absence of GAP to get further details on the composition of the gold surface. XPS analysis (Figure 4-11 and Table 4-2), for the as-prepared AuNPs,

revealed that ca. 9-10% Au(I) is still present. Cold welding of ultrathin gold nanowires has been reported as the result of fast surface-atom diffusion under low pressure.[179] Such atom diffusion has been also suggested in the case of NWs formation in the presence of surfactants.[164] I hypothesize, however, that the reduction of residual Au(I) by the H_2O_2 produced in the reduction of O_2 could provide the "glue" for fusing the AuNPs together when the necklaces are already formed. This observation was further supported by a control experiment to verify the role of H_2O_2 in the fusion process. I prepared linear AuNPs aggregates by addition of NaCl in EtOH following a reported procedure.[125] Their aggregation is reversible, as reported. However, after the addition of H_2O_2, rapid, irreversible fusion is observed as shown in Figure 4-12. This strongly supports the suggestion that H_2O_2 reduces the residual Au(I) present in the aggregated nanoparticles leading to their fusion into NWs.

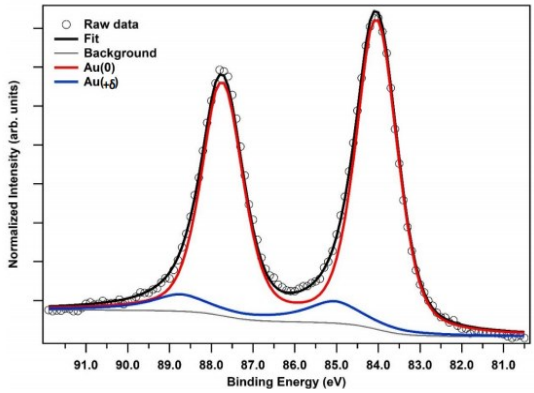

Figure 4-11. Au 4f photoemission line.

Element	Surface elemental composition (at%)
O	18
C	32
Na	20
Ag	2
Au	28

Table 4-2: Surface elemental composition.

Later, by further examining in detail the formed nanowires, I found that the "memory" of the original nanoparticles is manifested by their wavy aspect, which is not much different from that observed by Xia et al.[164] for nanowires prepared in the presence of cetyl-

trimethylammonium bromide. I cannot rule out that Au atoms could diffuse along individual nanowires to generate smooth surfaces, but this is not the process that starts the AuNPs fusion. The TEM revealed that, contrary to ultrathin NWs,[163, 180, 181] the NWs I have prepared are very likely polycrystalline rather than single-crystal structures. Notably, the branching of the nanowires occasionally observed is probably on account of the merging of smaller diameter nanoparticles. It has been demonstrated that, while gold nanoparticles of the same size aggregate in a linear fashion, the coexisting smaller ones are less selective leading to lateral aggregation (Figure 4-13).[83] Obviously, during the growth process, nanoparticles of different size coexist in spite of the rather narrow size distribution of the original AuNPs preparation. The wavy morphology of these NWs and the absence of any surfactant for their preparation is likely on the basis of their easy passivation, in strong contrast with what is typically observed with gold nanorods for which ligand exchange is not a trivial endeavour.

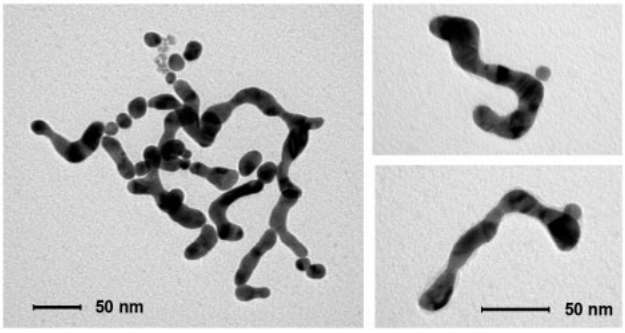

Figure 4-12. TEM image of the material collected from a solution of AuNPs after NaCl-induced linear aggregation and subsequent addition of H_2O_2. Nanowires were obtained without adding GAP.

To sum up, the experimental evidence suggests that the small amount of GAP present after the partial depletion process is oxidized to GAP-COOH in the presence of O_2, which, in turn is reduced to H_2O_2. GAP-COOH is responsible for the aggregation of AuNPs into mostly necklace-like aggregates while the reduction of residual Au(I) to Au(0) by H_2O_2 is responsible for the fusion of the aggregates with formation of nanowires. It has been reported [182] that gold nanorods can be oxidized by O_2 to Au(I) under acidic conditions and high temperature in the presence of CTAB leading to their shortening. Although my conditions are much different from those reported for such a process to occur, I cannot rule out that a similar oxidation reaction could constitute an additional source of Au(I) for the fusion of my AuNPs.

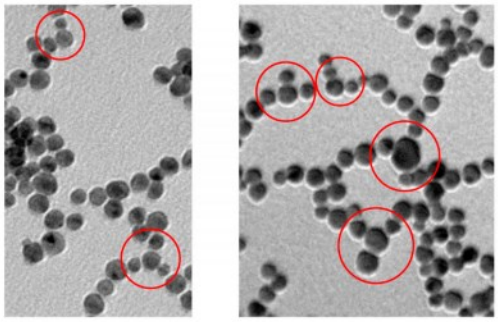

Figure 4-13. TEM pictures with highlighted branching points formed due to the non-linear disposition of AuNPs of small size in two different samples still mostly at the necklace-like aggregation state.

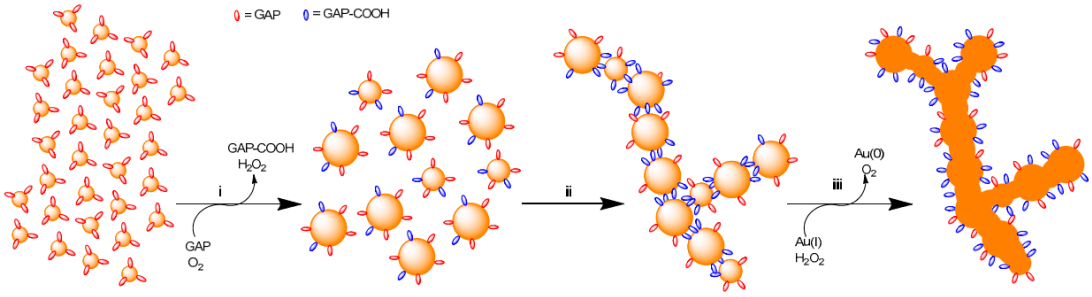

Figure 4-14. Cartoon rendition of AuNPs evolution towards nanowires: (i) GAP (red) poorly-passivated, small AuNPs grow by clustering and coalescence; the nanoparticles catalyze the oxidation of GAP to GAP-COOH (blue) and O_2 is reduced to H_2O_2; (ii) larger nanoparticles aggregate to form necklaces in a process mostly driven by GAP-COOH. Ramifications occurs because of the less selective aggregation of smaller nanoparticles; (iii) residual Au(I) is reduced to Au(0) by H_2O_2 and this induces fusion and nanowires formation.

4.5 Conclusion

In summary, I have reported a straightforward and mild procedure to induce the aggregation of AuNPs mostly in a linear fashion to form necklaces that eventually fuse into nanowires. Experimental evidence indicates that the evolution of the nanoparticles into nanowires is associated with a redox process catalysed by the nanoparticles involving the oxidation of the glucose moiety of GAP, the reduction of O_2 to H_2O_2 and eventually, the reduction of remaining Au(I) ions present in the gold clusters by the H_2O_2 formed. The product of the oxidation of GAP, the gluconic acid derivative GAPCOOH, appears to drive the mostly linear aggregation of the AuNPs while their fusion requires the reduction of residual Au(I) to Au(0) by H_2O_2. Because of the small amount of passivating agent present at the onset of the experiments, nanoparticles grow quickly by interacting together and

coalescing into bigger ones. At the early stages of the process, GAP exerts the double role of a reducing agent on one side and a source of the efficient crosslinking compound GAP-COOH on the other. Fusion of the linear aggregates into nanowires is then due to reduction of residual Au(I) by H_2O_2. The overall process is depicted in Figure 4-14. The final result is the synthesis of NWs with a broad SPR band centred at a wavelength that is more red-shifted the longer the incubation time. They can reach wavelengths well above 1000 nm. These nanowires can be covered with a thiol that, by forming a surrounding, passivating monolayer, stabilizes them, prevents any further growth, and allows their lyophilization and resuspension in water without any significant change in optical properties.

I believe that these results are very important for several applications, particularly in the field of nanomedicine [183] in view of the great interest in nanosystems presenting plasmon resonance bands shifted in the IR region where cells and tissues do not absorb the radiation. Accordingly, also because of the use of non-toxic GAP in water and without any organic solvent or surfactant [184] and the ease of functionalization, they can be potentially used for therapeutically relevant or analytical purposes.

Chapter 5. Monolayer protected AuNPs for capturing proteins

5.1 Introduction

As discussed in Chapter 1, many diseases are correlated with the presence of certain biomarker proteins or irregular protein concentrations.[118] By definition, a biomarker is a molecule that is objectively measured and evaluated as an indicator of normal biological processes, pathogenic processes or pharmacological responses to a therapeutic intervention.[185] Thus, biomarkers can be studied through proteomics as an indicator for monitoring disease at the early symptom stage. Proteomics is the large-scale study of the proteome, i.e. the entire set of proteins present in an organism, in particular related to understanding their structure and function.[186] The great progresses in the field of proteomics that have been obtained during last decades, are based also on approaches as the activity-based protein profiling, which was extensively employed to carry out proteomic studies within complex proteomes quantifying the total activity of a protein or family of proteins sharing the same activity. However, as discussed in Chapter 1, in spite of ABPP being a powerful tool in many biological applications, such as finding new enzyme inhibitors,[187] drug screening,[188] several important drawbacks are still present in this techniques. For instance, the quantification and slow analysis times remain an issue considering the proteins must be separated from complex mixtures.[189] Furthermore, ABPP probes have limited cell permeability due to their bulky reporter unit.[190] Therefore, the development of novel detection strategies would be highly welcome and a great amount of work in these directions is still needed.

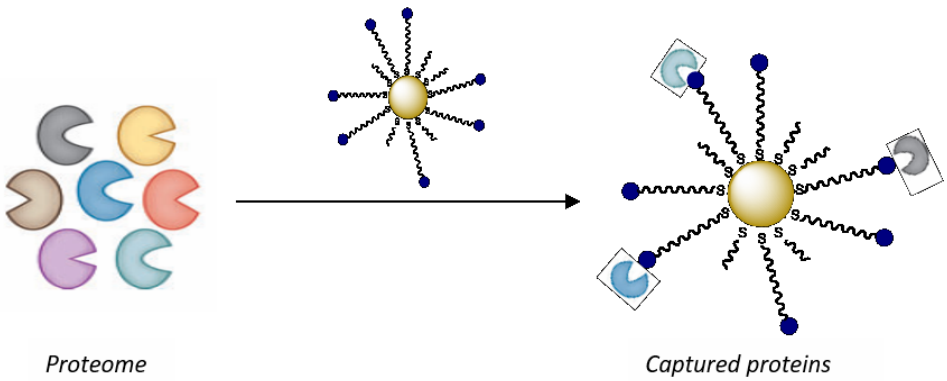

Figure 5-1. Capture of proteins within a proteome by previously functionalized gold nanoparticles.

AuNPs have been gaining attention as a promising tool for studying the interaction with proteins. As I have shown, AuNPs can be synthesized in a straightforward manner and can be made highly stable. Second, they possess unique optoelectronic properties. The third aspect, but not the less important, in ABBP detection strategy, the desired proteins can be separated from the proteome with a molecular-weight cut-off.[191] Furthermore, using AuNPs will not only improve the sensitivity, but also NPs plasmonic band can be a reporter of the protein capture, separation process could be avoided, and the system quantified *in situ*, because of the surface plasmonic resonance band is deeply sensitive to nanoparticles size and formation of aggregates.[192]

Therefore, in this chapter, I will describe the first step I have done for developing a complementary strategy with respect to the one I have followed in the previous chapters for addressing the interaction of AuNPs with biomolecules relying on the Au-N interaction. Here I pursued the functionalized AuNPs to interact covalently with a specific enzyme, urokinase plasminogen activator (uPA), aiming to test the covalent capture of a protein. My idea consists in combining the plasmonic properties of gold nanoparticles with the activity-based protein profiling approach developed by Cravatt and co-workers to build a supramolecular protein-sensing system capable to covalent-capture the desired protein or protein family (Figure 5-1). The binding process is hence performed by an irreversible inhibitor of a protein for its "capture". The enzyme uPA is a trypsin-like serine protease that can selectively bind with its membraned-anchored receptor (uPAR).[193] This process, is implicated in pathological processes, such as tumor growth, metastasis and inflammation. Once bound to the receptor, the inactive zymogen plasminogen can be catalyzed by uPA that converts it into the active proteinase plasmin. Plasmin plays an important role in the breakdown of extracellular matrix (ECM). It activates several matrix metalloproteases, which, in turn, degrade several components of the ECM including fibrin, laminin, and fibronectin. Proteolytic degradation of this ECM is very important for tumor growth and metastasis, and the uPA-uPAR system appears to be a key player in the proteolytic degradation process in cancer invasion and metastasis.[194, 195] Therefore, this serine protease is an interesting target in the fight against cancer.

5.2 Ligand design

The structure and mode of action of uPA is well-known, and most of its inhibitors are characterized by a basic function that forms a specific ionic interaction with the carboxylate group of Asp-189 of the S1 site in the deepest pocket of the substrate binding groove of the enzyme. But most of these inhibitors suffer from a poor selectivity and reversible targeting process.[196-198] K. Augustyns and co-workers [199] firstly reported several selective, irreversible uPA inhibitors which were based on a peptidic structure. The most potent and selective peptidic inhibitors ever reported among them, is the dipeptidyl diphenyl phosphonate compound (Figure 5-2). The irreversible inhibition of the enzyme, which leads to the phosphorylation of the enzyme, is attributed to the covalent reaction between the diphenyl phosphonate group and the active site of the serine protease.[200, 201] In addition, the guanidinylated benzyl group endow the inhibitor the ability to provide high selectivity and high potency toward uPA by taking advantage of interactions between the terminal guanidine and the phenyl ring and amino acid residues present in the active site.

Accordingly, my idea was to prepare monodisperse gold nanoparticles and to functionalize them with a thiol bearing the specific inhibitor. To ensure the nanoparticle water solubility, a hydrophilic ligand like **1** can be employed. This part of my overall project has not been completed yet and only the synthesis of the thiolated molecules to be used for the passivation of the AuNPs has been performed so far.

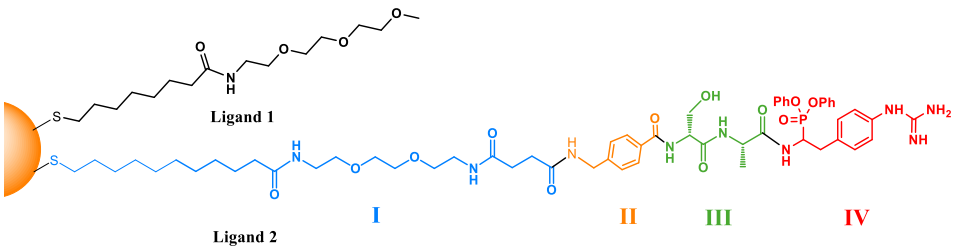

Figure 5-2. The structure of the coating ligands and analytes used.

The chemical structure of the ligand **2** (Figure 5-2) can be divided into four parts: 1) the hydrophilic oligo(ethylene glycol) moiety (blue) bearing thiol, that acts as a water soluble linker to be anchored on the nanoparticles surface; 2) general linker (orange), that acts as a building block for coupling the capture unit; 3) inhibitor unit, that would covalently bind

the protein and leads to phosphorylation of serine; 4) capture unit, that ensures high selectively for the target protein. The mixed monolayer AuNPs can be obtained via ligand exchange and the component of the surface can be modulated by tuning the ratio of ligand **1** and ligand **2** to afford a highly sensitive yet stable nanoprobe.

5.3 Synthesis of the thiolated ligands

The important objective discussed in this section is the preparation of the functional ligands. The first molecule of the series, amide-DEG, has been conceived for two reasons: first, it exhibits solubility in bio-friendly solvents; second, as anticipated above, it should be of the appropriate length to avoid masking the active functionalities on ligand **2**. Thiol **1** was synthesized according to the previous protocol of our group (Scheme 5-1).

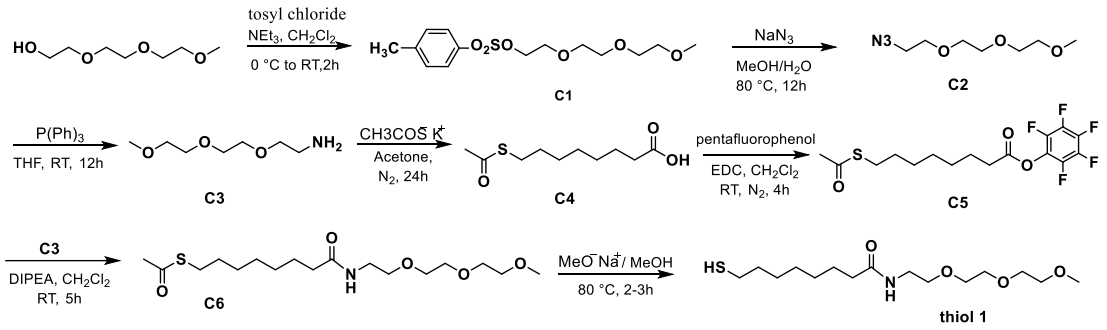

Scheme 5-1. Synthetic route of thiol **1.**

Subsequently, I prepared thiol **2**, that has a much more complicated structure than **1**. For this reason, the synthetic route is divided into three building blocks, afterwards, converging into one single molecule at the very end. The first building block (I) is alkyl-DEG chain terminated by a carboxylic group for connection of the recognition unit of the molecule (Scheme 5-2). The other extremity with the double bond will be functionalized with a thiolated unit for the anchoring to the AuNPs surface.

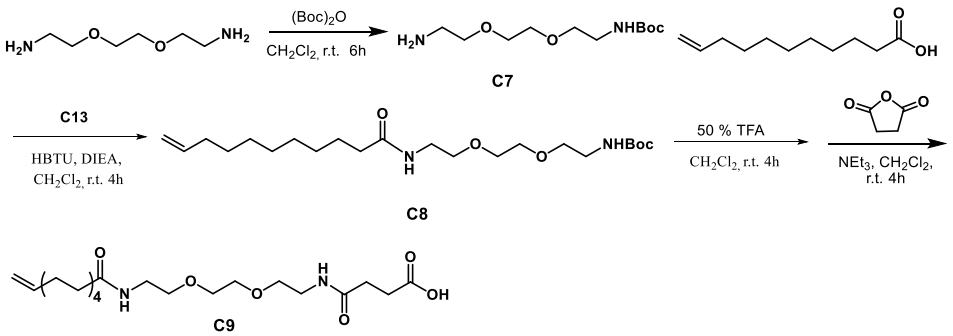

Scheme 5-2. Synthetic route of building block (I).

The second building block (IV) presents the functional unit to selectively inhibit the target protein. The disubstituted benzene derivative comprised two important moieties, one of the substituents is an amino phosphonate group which will be responsible for the phosphorylation of the protein, while the other is a guanidine moiety affording high selectivity. Afterwards, the dipeptidyl group can be conjugated by coupling reaction with the terminal amine. Here, a common method for the removal of Cbz protective group was hydrogenation, however, this deprotection process did not provide the desired product C12. I monitored the reaction by ^{1}H-NMR and ESI-MS every five minutes and observed that the product can be easily degraded as soon as it is generated by hydrogenation. I speculated that the phosphonate group could be damaged by the weakly basic reaction conditions leading to its decomposition. Based on this consideration, a modified synthetic procedure was exploited by adding 5% HCl into the reaction mixture. The result was in line with my hypothesis and the product was obtained in 98% yield.

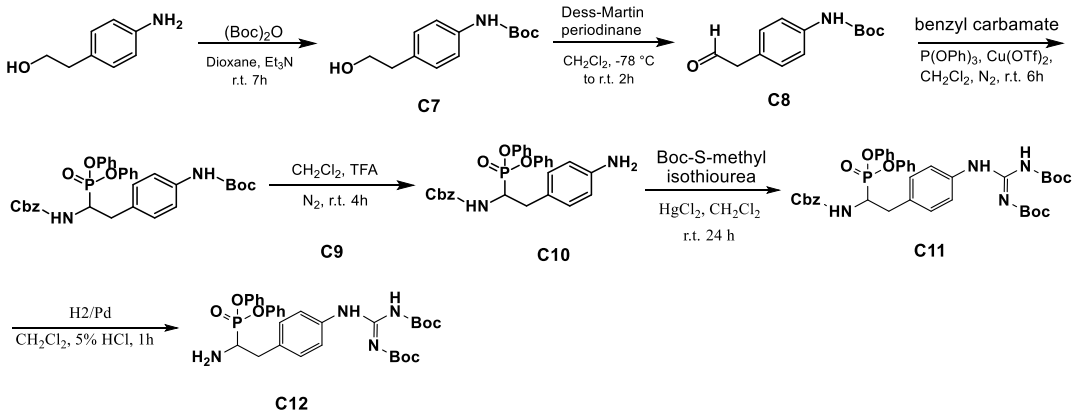

Scheme 5-3. Synthetic route to building block (IV).

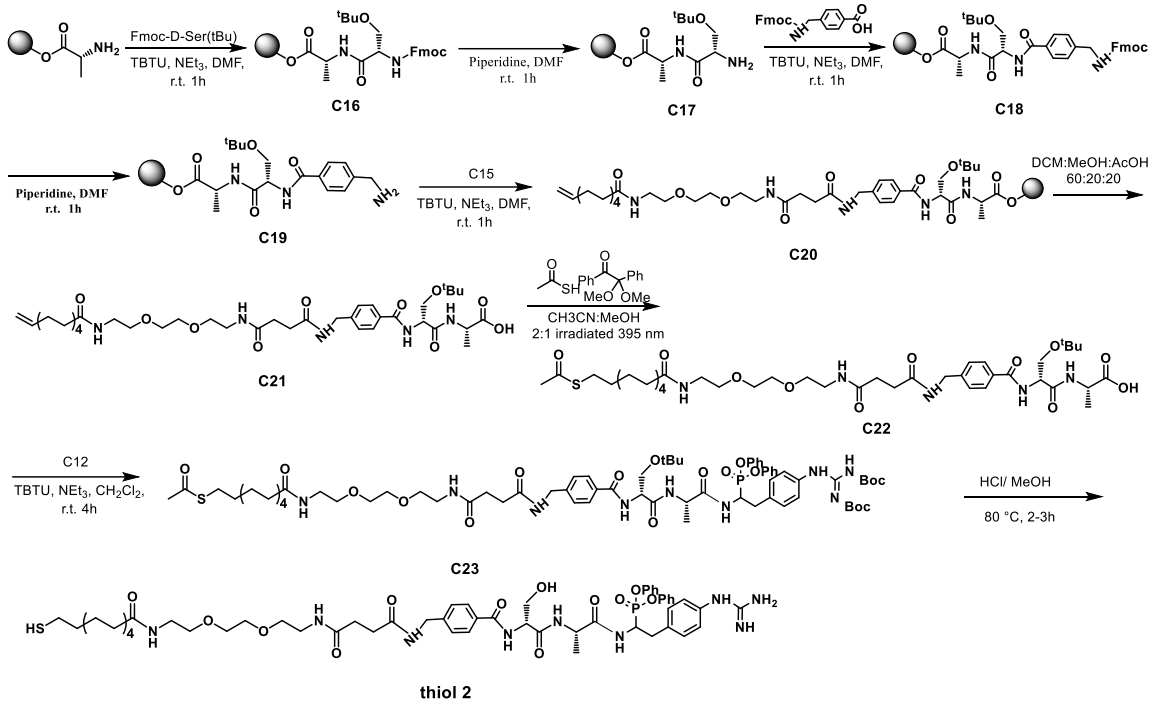

Scheme 5-4. Synthetic route to thiol **2**.

The third building block (III) is the dipeptidyl group, which was prepared by using standard solid-phase peptide synthesis (SPPS) and Fmoc chemistry on a 2-chlorotrityl chloride resin (Scheme 5-4). Afterwards, ligand **2** was obtained through a series of standard reactions. The overall synthetic process required more time and efforts than I had expected. At the moment I am convinced to have prepared **2** on the basis of the ESI-MS spectrum. However, a full characterization by ^{1}H- and ^{13}C-NMR has not been performed yet.

5.4 Conclusion

In summary, I have prepared a thiolated targeting probe which can be used for the highly selective and irreversible interaction with the protein uPA. Its design included the dipeptidyl diphenyl phosphonate and guanidinylated benzyl moieties each playing a different role. The diphenyl phosphonate group is expected to react, forming a covalent bond, with the active site of the serine protease. The guanidinylated benzyl group endows the inhibitor with high selectivity and high potency toward uPA by taking advantage of interactions between the terminal guanidine and the phenyl ring and amino acid residues present in the active site. Once ligand **2** will be fully characterized it will be conjugated to AuNPs of different sizes and covalent capture experiments of the target protein will be

performed, first with the target only, afterwards in vitro using a simulated biological solution and, if things will go as expected, also in vivo.

Chapter 6. Materials and methods

6.1 Solvents, reagents and general procedures

Chemical reagents and solvents were purchased from Sigma-Aldrich and used as received without further purification unless stated otherwise. 2-Chlorotrityl amine resin and amino acids were obtained from Iris Biotech company and were kept at -24 °C. Tetrachloroauric acid was dissolved in a given amount of MilliQ water in accordance with the experimental requirement other way kept at -24 °C. The stock solutions for the titration experiment were kept at 4 °C in sealed vial to prevent oxidation and degradation. The solution of gold nanoparticles, including the citrate-passivate gold nanoparticles and the citrate-depleted ones were kept at 4 °C during storage. The free amines, which were obtained as ammonium salts, were deprotonated with weakly basic potassium carbonate and kept in EtOH at 4 °C.

The resin terminated by amine groups were revealed by Kaiser test under heating. Macherey-Nagel Alugram Xtra SIL G/UV_{254} plates were used for TLC experiment to monitor the reaction under 298/365 nm irradiation and phosphomolybdic acid ethanolic solution. Ethanolic $KMnO_4$ and ninhydrin were employed to monitor terminal alkynes and amines, respectively. Macherey-Nagel Keiselgel 60 with particles sizes of 0.04-0.063 mm were employed for flash column chromatography.

All glassware used for the preparation of the AuNPs was washed with freshly prepared aqua regia before use and rinsed with MilliQ water. Preparation and purification of all AuNPs were performed with MilliQ water. All AuNPs were purified with a Hettich Universal 320 R in the Amicon filter (10K).

6.2 Instrumentation

UV–Visible spectra were recorded on a Varian Cary 50 or Cary 100 spectrophotometer with 1 cm path length using Hellma Suprasil® quartz cuvettes. The spectrophotometer was equipped with a cell holder with a water circulation to keep the temperature constant during scanning kinetics.

Electronic circular dichroism (ECD) spectra were performed with a Jasco J-1500 instrument equipped with a thermostatic system with water circulation. A fused quartz cell of 1cm path length (Hellma) was used.

Dynamic light scattering (DLS) measurements were performed with a ZetaSizer NanoS instrument from Malvern equipped with a laser system. For the measurements quartz cuvettes were used with an optical path of 1 cm in a cell holder with a thermostatic system.

Fluorescence spectra were recorded on a FL_LS50B spectrophotometer with 1 cm path length using Hellma Suprasil® quartz cuvettes, equipped with pulsed xenon lamp and a cell holder thermostatic system with water circulation.

ESI mass spectra were measured on an Agilent Technologies 1100 Series system equipped with an MSD SL Trap mass spectrometer (G2445D SL) and ESI source in methanol or acetonitrile

NMR spectra were recorded on a Bruker Avance DPX 200, Avance 300 or AVIII 500 spectrometers operating at 200, 300 and 500 MHz for proton and 50.3, 75.5 and 125.7 MHz for ^{13}C, respectively. The chemical shifts refer to the tetramethylsilane used as an internal standard. The symbology used to describe the spectral signals is the following: s = singlet; d = doublet, t = triplet, q = quartet, qn = quintet, st = sextet, m = multiplet, broad = enlarged.

Thermogravimetric analyses (TGA) were carried out on ~0.5 mg of nanoparticles with a Q5000 IR instrument. Solvent was removed by heating the sample at 100 °C for 10 minutes and then a 10 °C/min temperature ramp was applied from 100 to 1000 °C.

Transmission electron microscopy (TEM) analyses were run on a FEI Tecnai G12 microscope operating at 100 keV and with corresponding magnification; the pictures were recorded by CCD. Measurement samples were distributed on a copper grid and the excess of solvent discarded with filtering paper. Size distribution analysis was carried out by performing direct statistics with ImageJ2x software.

6.3 Gold nanoparticle preparation

In this section I will describe the AuNPs preparation, purification, characterization and the analytical methods for doing this for a comprehensive understanding of how parameters like amounts and type of reagents, temperature control the shape and size of AuNPs. The stabilizing and capping agents are important to hinder further growth and aggregation and for the functionalization of the AuNPs to endow them of specific functions in the reaction medium.

6.3.1 Sample preparation

All glassware used in contact with AuNPs was treated with aqua regia and rinsed with distilled water 5 times to prevent contamination. All starting materials used for the synthesis of AuNPs including purification were treated with Milli-Q water (>18 MΩ cm^{-1}). The solution of reducing agent (citrate, $NaBH_4$) was prepared immediately prior to their usage.

6.3.2 Synthesis of citrate capped AuNPs

Citrate protected AuNPs (10, 15 and 25 nm) were prepared by modifying a previously reported procedure which is based on the Turkevich method. In the typical synthesis, for AuNPs with size of about 10 nm, to 5.6 ml of water, an aqueous solution of 1.6 ml of sodium citrate (510 mM), 250 µl of silver nitrate (10 mM) and 500 µl of tetrachloroauric acid (50 mg, 0.127 mmol, 250 mM) were added. The mixture is vigorously stirred for 5 minutes. During this period of time the colour of solution changed ranging from bright yellow to dark green and finally black. Later on, the mixture solution was quickly transferred into boiling water (117 ml). An immediate colour change from pale yellow to ruby occurred within a few seconds, indicating the formation of AuNPs. The solution was kept under reflux for 1 hour to ensure the completion of the reaction and then allowed to cool down to room temperature to obtain the citrated-stabilized nanoparticles. Gold nanoparticles with size of 15, 25 nm were prepared by the same method with different molar ratio of citrate to tetrachloroauric acid. The amount of materials is summarised in Table 6-1. The ratio of the gold precursor to reducing agent was varied leading to the

production of the nanoparticles of the desired size. The concentration of the stock solution was quantified by UV-Visible spectra (Figure 6-2).

In the case of 5 nm nanoparticles preparation procedure, a previously reported approach was followed.[202] Typically, to 180 mL of water, a 5 ml of 0.01 M tetrachloroauric acid and 5 ml of 0.01 M sodium citrate aqueous solution was added under stirring in an ice bath. After 10 minutes, 5 ml of freshly prepared 0.1 M sodium borohydride was added into the above mixture dropwise. The solution change from pale yellow to deep red upon addition of the reducing agent, indicating the formation of AuNPs. The solution was kept at ice bath temperature for 30 minutes to ensure the completion of the reaction and then to room temperature. The resulting nanoparticles were purified by centrifugation.

Sampe Size	$HAuCl_4$ / mM	$AgNO_3$ / mM	Citrate / mM	Molar ratio of gold(III) to citrate	Temperature / °C
10 nm	1.00	0.02	6.76	1.00/6.76	100
15 nm	1.00	0.02	2.61	1.00/2.61	100
25 nm	1.00	0.02	1.43	1.00/1.43	100

*The concentration here is the final one.

Table 6-1: Experiment conditions and concentration* used for the synthesis of citrate capped AuNPs.

6.3.3 Purification of AuNPs

To remove the citrate and its oxidation products from the solution used for their synthesis, the freshly prepared nanoparticles were purified by using an Amicon filter of 15 ml of 10 KDa molecular weight cut-off centrifuged for 7 minutes at 5000 rpm (Figure 6-1). The filters were washed 5 times with 50% water in ethanol before adding the colloidal gold. After the centrifugation, the supernatant was discarded leaving around 100 µl of solution which was then resuspended in 15 ml of Milli-Q water. The solution was further centrifuged (7 min at 5000 rpm) and the supernatant discarded for another 4 cycles. The concentrated and purified AuNPs aqueous solution was frozen with dry ice/acetone and freeze-dried overnight on a Cinquepascal 105PDGT lyophilizer to give 43 mg of "naked" nanoparticles. For the stock solution, the resulting pellet was finally resuspended in 10 ml of ethanol. The concentration of the nanoparticles was determined by UV-visible. The

residual amount of citrate ions on the surface of nanoparticles after purification was determined by TGA.

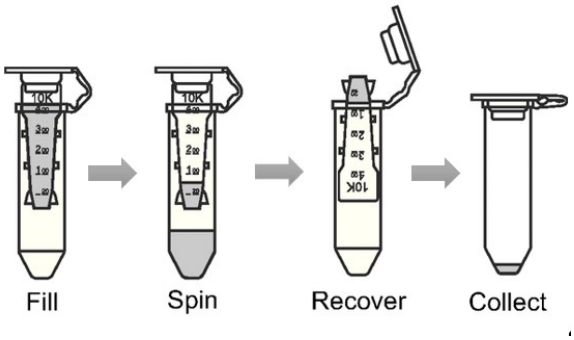

Figure 6-1. Schematic representation of Amicon Ultra centrifugal filters for separating nanoparticles.

6.3.4 Characterization of AuNPs

Several analytical and imaging techniques have been used to fully characterize the synthesized AuNPs. The following subsections will introduce how these techniques were applied and the related sample preparation steps.

6.3.4.1 UV-visible and TEM

Considering the properties of AuNPs, a surface plasmon resonance band (SPR) originates in the absorption spectrum which is controlled by the morphology, size and concentration of gold nanoparticles. UV-visible spectra can be a useful tool to give the information about the size, shape, concentration and aggregation of gold nanoparticles in a fast and real-time on-line analysis as discussed previously.

In order to prepare the stock solution, UV-visible spectra were recorded on a Cary 50/100 spectrometer using 1 cm path length quartz cuvettes. The nanoparticles concentration was determined with a previously reported analytical method.[203] By using the data of extinction coefficient (ε_{450}), the particle concentration can be obtained by dividing the value of A_{450} for a standard path length (l) of 1 cm.

For the synthesized nanoparticles, the absorption spectrum in the region of the SPR band red shifts to longer wavelengths (varying between 514 and 520 nm), according to their size increase (Figure 6-2). The corresponding concentrations are shown in Table 6-2.

Transmission electron microscopy (TEM) can give a direct information concerning the size, shape and dispersion of nanoparticles. Thus, Figure 6-3 reports the TEM images and diagrams of the different nanoparticles prepared in terms of mean particle diameter distributions. As expected, the shape of the synthesized nanoparticles was spherical and uniform. The average diameter for the nanoparticles is 5.2±0.5 nm, 9.7±1.3 nm, 15±2.0 nm and 25.5±2.0 nm.

Sample Size	Absorbance intensity (SPR)	A_{450}	ε_{450}	concentration
5 nm	0.8	0.50124	7.20×10^6	69 nM
10 nm	0.8	0.47501	4.43×10^7	10 nM
15 nm	0.8	0.45531	2.10×10^8	2.45 nM
25 nm	0.8	0.44253	1.10×10^9	0.41 nM

Table 6-2: The extinction constant and concentration of different size of resulting nanoparticles.

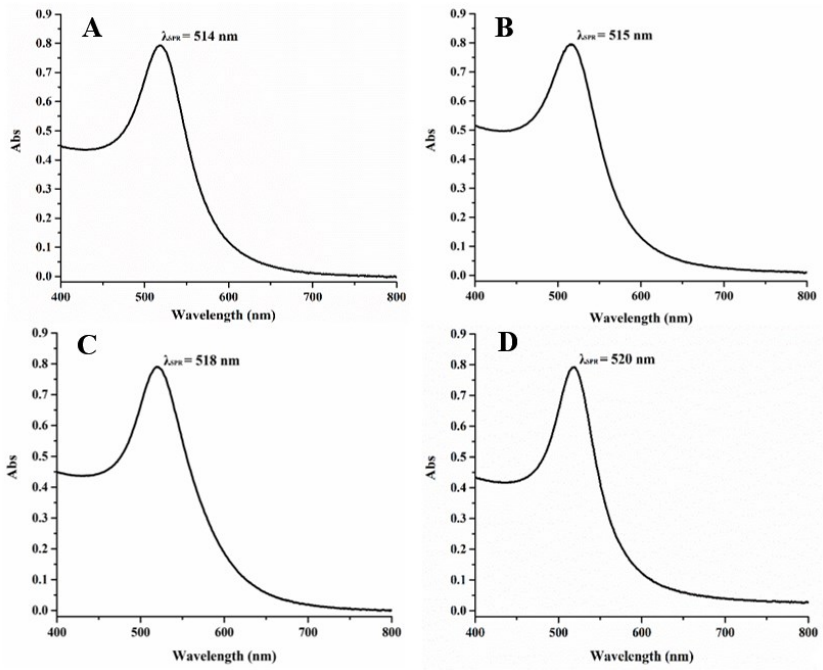

Figure 6-2. UV-visible spectra of the SPR region of AuNPs of the 5 nm (A), 10 nm (B), 15 nm (C) and 25 nm (D) in ethanol.

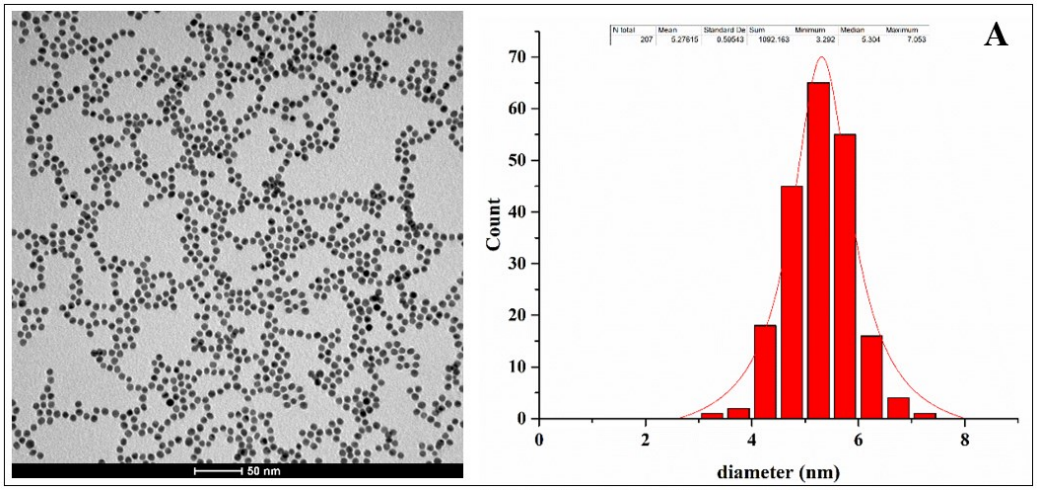
50 nm
A
Count
diameter (nm)

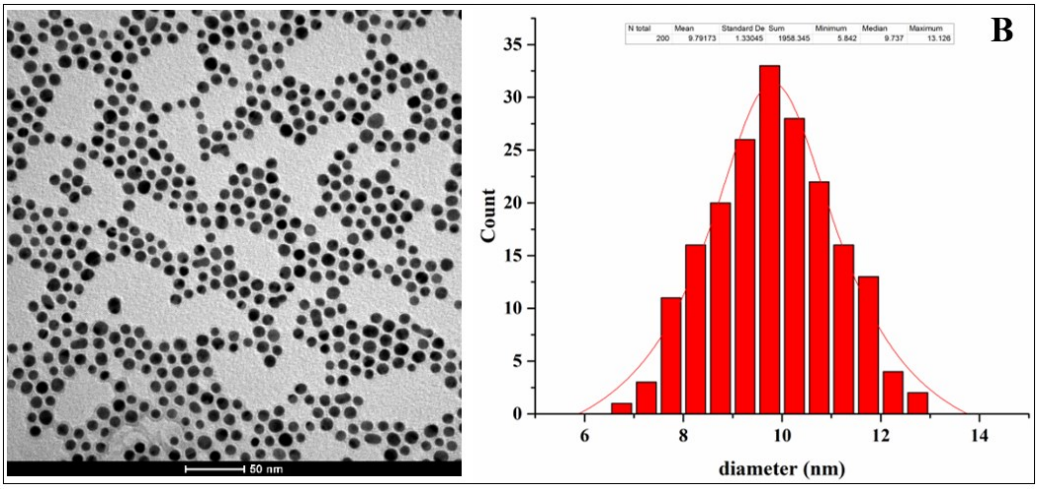
50 nm
B
Count
diameter (nm)

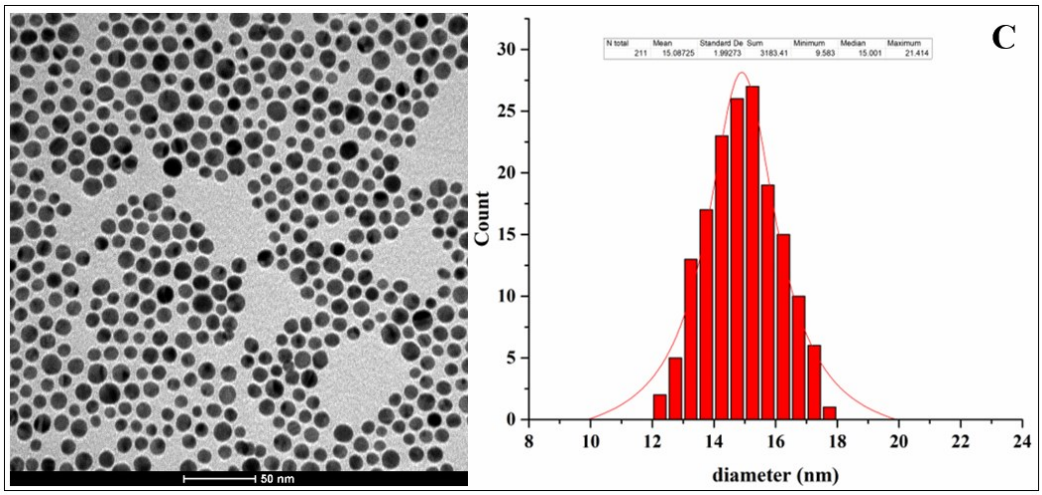
50 nm
C
Count
diameter (nm)

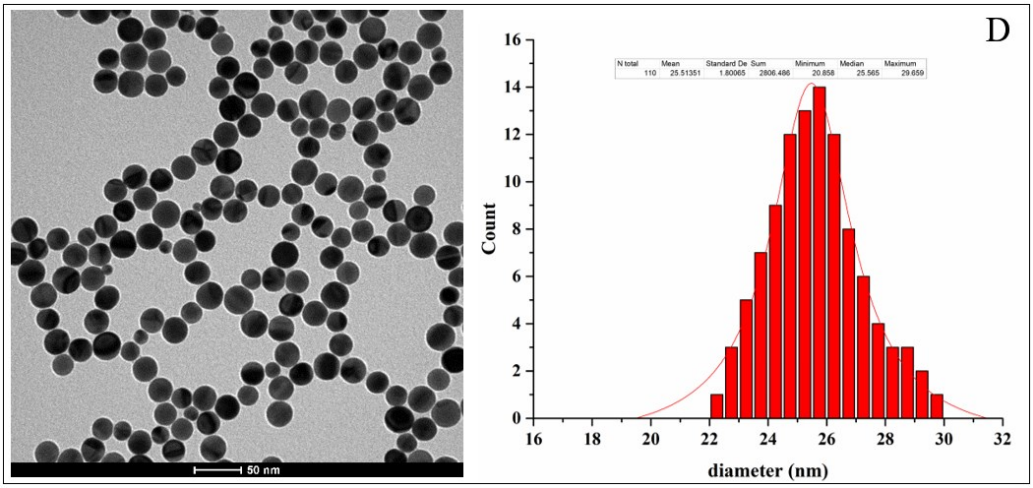

Figure 6-3. TEM image of resulting nanoparticles and diagram of particle size distribution: average diameter = 5.2±0.5 nm (A), 9.7±1.3 nm (B), 15±2.0 nm (C) and 25.5±2.0 nm (D).

6.3.4.2 Dynamic light scattering

Dynamic light scattering (DLS) was employed to determine the size of nanoparticles in solution. It provides an accurate measure of nanoparticle hydrodynamic size. The result of the dynamic light scattering studies were consistent with the TEM results (Table 6-3), showing the diameter was varying from 6.3 to 26 and no obvious aggregation was found after a month of storage at room temperature or 4 °C.

Sample size	diameter (nm) / DLS	diameter (nm) / TEM
5 nm	6.3	5.2
10 nm	9.4	9.7
15 nm	17	15
25 nm	26	25.5

Table 6-3: The average of hydrodynamic diameter obtained by DLS and core diameter of nanoparticles obtained by TEM.

6.3.5 Calculation of the amount of the surface coverage by citrate ions

The amount of surface gold atoms per nanoparticle (n_{out}) was calculated as previously reported in the literature [204] by considering the AuNPs as spherical employing the following formula (eq 6-1):

$$n_{out} = \left(\frac{4\pi}{3\nu_g}\right)[(R-\delta)^3 - (R-\delta-2.38)^3] \qquad \text{eq 6-1}$$

Where ν_g is the average volume of a gold atom (17 Å^3), R is the radius of the nanoparticle and the organic layer, δ is the thickness of the organic monolayer and 2.38 is the thickness of the outer shell of gold atoms on the nanoparticle. All previous distances are expressed in Å. Notice that despite the difficulty to obtain a reliable value of the organic layer thickness (δ), R - δ is equal to the radius of the gold core only, measured with high precision from TEM images. By employing the total volume of the gold sphere and the average volume of a gold atom, we can calculate the number of gold atoms for forming the corresponding nanoparticle. Therefore, the percentage of the total gold which is actually on the surface of the nanoparticles can be obtained. This allows us to evaluate the amount of gold atoms on the surface before and after the binding event.

6.4 Chemical synthesis

Compound **2** and its intermediates in the Chapter 4 were synthesized by the former lab member and manuscript is in the progress. Remaining compounds and intermediates were synthesized and characterized which is described below.

6.4.1 8-mercapto-N-(2-(2-(2-methoxyethoxy)ethoxy)ethyl)octanamide (thiol 1)

Thiol 1 was prepared according to the following procedure [205]:

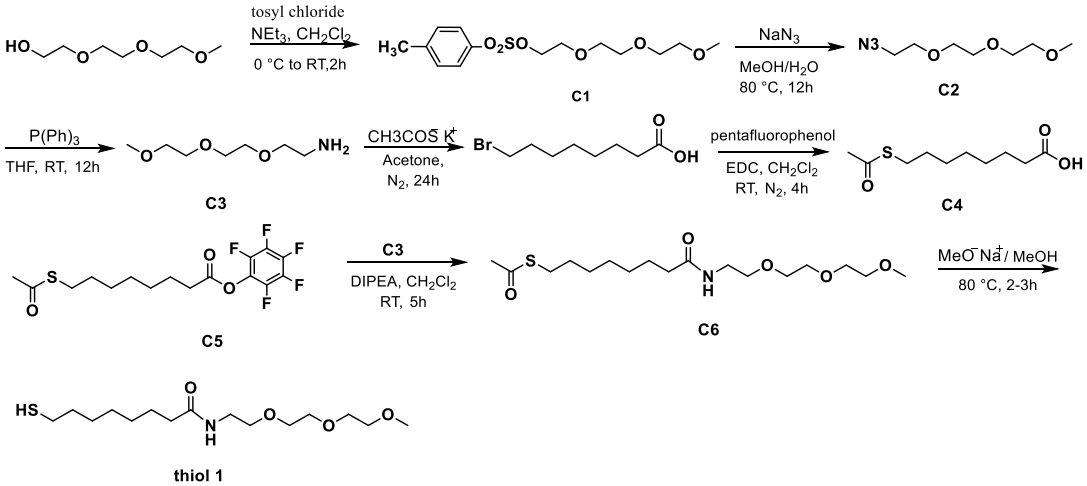

2-[2-(2-Methoxyethoxy)ethoxy]-1-ethyl 4-methylbenzenesulfonate (C1). Triethylene glycol monomethyl ether (1.0 g, 6.09 mmol, 1.0 equiv) was dissolved in 17 ml of triethylamine and the solution of 15 ml anhydrous dichloromethane of tosyl chloride (1.3

g, 6.69 mmol, 1.1 equiv) was dropwise added under the ice bath. The reaction mixture was stirred for another 2 hours at room temperature under nitrogen, then it was diluted with 15 ml of dichloromethane, extracted with 6 M HCl (2 × 10 ml), washed with 5% $NaHCO_3$ (2 × 10 ml) and water (2 × 10 ml). The organic phase was dried on anhydrous Na_2SO_4 and the solvent evaporated. 1.25 g of **C1** were obtained as pale yellow oil. Yield 79%.

^{1}H-NMR (500 MHz, $CDCl_3$) δ_H (ppm): 7.67-7.40 (m, 4H, C_6H_4), 3.66-3.55 (m, 10H, OCH_2), 3.37 (s, 3H, OCH_3), 2.44 (s, 3H, $PhCH_3$).

ESI-MS (m/z, MeOH/H^+): 319.4 [M+H^+].

2-[2-(2-Methoxyethoxy)ethoxy]ethyl azide (C2). The compound of **C1** (900 mg, 2.83 mmol, 1.0 equiv) and sodium azide (2.2 g, 33.8 mmol, 12 equiv) were dissolved in anhydrous DMF (20 ml) in a pressure resistant Pyrex bottle. The bottle was tightly closed, and the reaction mixture was heated for 12 hours under stirring at 80 °C. The reaction mixture was concentrated, the residue was diluted with 20 ml of water and extracted with dichloromethane (3 × 20 ml). The organic layer was dried over anhydrous Na_2SO_4, the crude products were used in the next step without any purification after the solvent evaporated, 0.517 g (98%) of **C2** was obtained as a colorless oil.

^{1}H-NMR (500 MHz, $CDCl_3$) δ_H (ppm): 3.66-3.37 (m, 15 H, OCH_2CH_2O).

ESI-MS (m/z, MeOH/H^+): 190.3 [M+H^+].

2-[2-(2-Methoxyethoxy)ethoxy]ethylamine (C3). Triphenylphosphine (5.963 g, 22.76 mmol, 4.0 equiv), was added to a solution of **C2** (1.076 g, 5.69 mmol, 1.0 equiv) in 14 ml of THF and 7 ml of H_2O. The reaction mixture was stirred for 12 hours under N_2 at room temperature. After the completion of the reaction, the mixture was concentrated in vacuo to remove the solvent and, to the residue, 20 ml of toluene and 35 ml of water were added. The heterogeneous mixture was stirred until phosphine oxide was dissolved, the mixture was washed with DCM and extracted with HCl solution (1 M, 2 × 15 ml). the combined aqueous solution was evaporated to dryness in vacuo. After solvent removal, 793 mg (85%) of amine (**C3**) were obtained as a pale yellow oil.

^{1}H-NMR (500 MHz, $CDCl_3$) δ_H (ppm): 3.57-3.42 (m, 10H, OCH_2CH_2O), 3.30 (s, 3H, CH_3O), 2.79 (t, 2H, CH_2N), 1.75 (s, 2H, NH_2).

ESI-MS (m/z, MeOH/H^+): 164.2 [M+H^+].

S-Acetyl-8-thiooctanoic acid (C4). A solution of 8-bromooctanoic acid (4.0 g, 17.93 mmol, 1.0 equiv) in 60 ml of acetone, was added potassium thioacetate (2.5 g, 21.89 mmol, 1.2 equiv). The reaction mixture was stirred for 15 hours at room temperature in a nitrogen atmosphere. After the completion of the reaction, the mixture was concentrated in vacuo, the residue was washed with 20 ml of water and extracted with dichloromethane (3 × 20 ml), and then the organic layers were collected and dried over Na_2SO_4. After solvent removal, the crude product was purified by flash chromatography (Hexane/EtOAc 1:2). 3.14 g (80%) of S-acetyl-8-thiooctanoic acid (**C4**) were obtained as a yellow oil.
^{1}H-NMR (500 MHz, $CDCl_3$) δ_H (ppm): 2.87 (t, 2H, CH_2), 2.65 (t, 2H, CH_2), 2.32 (s, 3H, CH_3), 1.77 (t, 2H, CH_2), 1.58 (t, 2H, CH_2), 1.38 (m, 6 H, CH_2).
ESI-MS (m/z, MeOH/H^+): 219.3 [M+H^+].

S-perfluorophenyl 8-(acetylthio)octanoate (C5). C4 (1.6 g, 3.66 mmol, 1.0 equiv) and pentafluorophenol (1.128 g, 6.131 mmol, 1.3 equiv) were dissolved in 15 ml of dry dichloromethane, and hydrochloride (EDC, 1.175 g, 6.130 mmol, 1.3 equiv) was added. The reaction mixture was stirred for 4 hours at room temperature under N_2. The solvent was removed under reduced pressure, the residue was treated with toluene (5 ml) that was then removed in vacuo. The acyl chloride (**C5**) was obtained in quantitative yield.
^{1}H-NMR (500 MHz, $CDCl_3$) δ: 2.87 (t, 2H, CH_2), 2.65 (t, 2H, CH_2), 2.32 (s, 3H, CH_3), 1.77 (t, 2H, CH_2), 1.58 (t, 2H, CH_2), 1.27 (m, 6 H, CH_2).
ESI-MS (m/z, MeOH/H^+): 385.4 [M+H^+].

S-(12-oxo-2,5,8-trioxa-11-azanonadecan-19-yl) ethanethioate (C6). C3 (1.010 g, 6.13 mmol, 1.0 equiv) and S-perfluorophenyl 8-(acetylthio)octanoate (**C5**) (3.07 g, 7.97 mmol, 1.3 equiv) was dissolved in 30 ml of dry dichloromethane. Then a solution of dry N, N-diisopropylethylamine (DIPEA, 1.004 g, 7.97 mmol, 1.3 equiv) were added. The mixture was stirred at room temperature for 12 hours in nitrogen atmosphere. The mixture was washed with 1 M HCl (2 × 10 ml), the organic layers were collected and dried over Na_2SO_4. After solvent evaporation, the crude product was purified by flash chromatography (EtOAc/CH3OH 9:1), giving 2.002 g (90%) of **C6** as a clear oil.
^{1}H-NMR (500 MHz, $CDCl_3$) δ_H (ppm): 6.13 (br, 1H, NH), 3.62-3.54 (m, 10H, CH_2O), 3.43 (m, 2H, CHN), 3.36 (s, 3H, CH_3O), 2.83 (t, 2 H, CH_2S), 2.29 (s, 3H, CH_3), 2.16 (t, 2H, CH_2CO), 1.72-1.45 (m, 4H, CH_2), 1.45-1.2 (m, 6H, CH_2).

ESI-MS (m/z, ACN/H^+): 364.4 [M+H^+], 386.3 [M+Na^+].

8-mercapto-N-(2-(2-(2-methoxyethoxy)ethoxy)ethyl)octanamide (Thiol 1).In 10 ml of dry ethanol, **C6** (0.718 g, 1.98 mmol) was added. To the mixture, a 6 M HCl solution in water (2.0 mL) was added. The reaction mixture was stirred for 2 hours at 80 °C under nitrogen atmosphere. After the completion of reaction, the reaction mixture was allowed to cool down and the solvent was evaporated obtaining 0.7862 g (95%) of **Thiol 1**.

^{1}H NMR (500 MHz, MeOD) δ_H (ppm): 3.67-3.60 (m, 8H, CH_2O), 3.56 (m, 2H, CH_2N), 3.50 (t, 2H,CH_2O), 3.38 (s, 3H, CH_3O), 2.52 (t, 2H, CH_2S), 2.43 (t, 2H, CH_2CO), 1.72-1.57 (m, 4H, CH_2), 1.48-1.33 (m, 6H, CH_2).

^{13}C NMR (126 MHz, MeOD) δ: 176.90 (1C, CO), 71.53 (1C, CH_2O), 70.16 (1C, CH_2O), 69.97 (1C, CH_2O), 69.90 (1C, CH_2O), 68.28 (1C, CH_2O), 57.76 (1C, CH_3O), 40.34 (1C, CH_2N), 34.34 (1C, CH_2), 33.68 (1C, CH_2), 28.59 (1C, CH_2), 28.35 (1C, CH_2), 27.78 (1C, CH_2), 25.73 (1C, CH_2), 23.56 (1C, CH_2S).

HR-MS: [M+H^+] calcd. for $C_{15}H_{31}NO_4S$ = 322.2074; found = 322.2081.

6.4.2 Synthesis of 4,15-dioxo-8,11-dioxa-5,14-diazapentacos-24-enoic acid

Compound **C9** was prepared according to the following procedure:

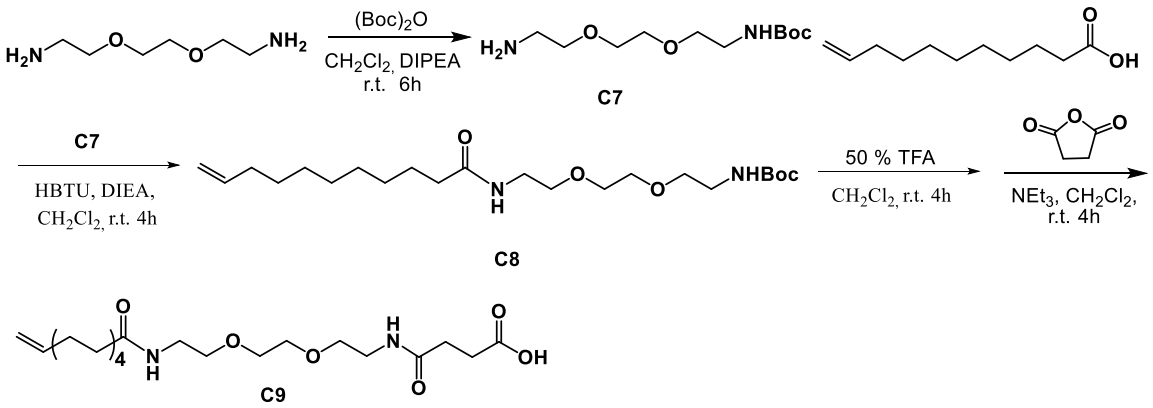

Synthesis of tert-butyl (2-(2-(2-aminoethoxy)ethoxy)ethyl)carbamate (C7). 1,2-bis(2-aminoethoxy)ethane (2.05 g, 16.6 mmol, 1.0 equiv) and DIPEA (0.51 mL, 0.3 mmol) were dissolved in 25 ml of anhydrous dichloromethane at room temperature, a solution of di-*tert*-butyl-dicarbonate (1.80 g, 8.45 mmol, 0.5 equiv) in anhydrous dichloromethane (10 ml) was dropwise added. The mixture was stirred for 6 hours at room temperature, the

resulting solution was concentrated under reduced pressure and purified by column chromatography (DCM/MeOH/NEt_3 19/1/0.01) to afford mono-protected product **C7** (1.85 g, 45%) as a colorless oil.

^{1}H-NMR (500 MHz, $CDCl_3$): δ_H (ppm): 5.16 (1H, br, NH), 3.62-3.51(m, 8H, OCH_2CH_2O), 3.30 (m, 2H, CH_2NH_2), 2.89 (t, 2H, CH_2NH), 1.65 (s, 2H, NH_2), 1.44 (s, 9H, CH_3).

ESI-MS (m/z, ACN/H^+): 249.2 [M+H^+], 271.4 [M+Na^+].

Synthesis of tert-butyl (2-(2-(2-(undec-10-enamido)ethoxy)ethoxy)ethyl)carbamate (C8). To a solution of 10-undecenoic acid (297 mg, 1.6 mmol, 1.0 equiv) in 15 ml of anhydrous dichloromethane was added HATU (638 mg, 1.68 mmol, 1.05 equiv) and DIPEA (0.36 ml, 1.92 mmol, 1.2 equiv), stirring was continue for 0.5 hour, after which, mono-protected **C13** (400 mg, 1.6 mmol, 1.0 equiv) was added, the reaction was stirred for additional 3.5 hours at room temperature. Afterwards, the solvent was removed under reduced pressure and the crude product was dissolved in ethyl acetate, washed with aqueous HCl (1M, 3 × 10 ml), saturated $NaHCO_3$ solution and brine and purified by column chromatography (EtOAc/Hexane 1/2 to 1/1) to give **C8** (564.4 mg, 85%) as a colorless oil

^{1}H-NMR (500 MHz, $CDCl_3$): δ_H (ppm): 5.81 (br, 1H, NH), 5.77 (m, 1H, CH), 4.99-4.87 (m, 2H, CH_2), 3.57-3.45 (m, 12H, CH_2O), 3.33 (m. 2H, CH_2), 2.15 (t, 2H, CH_2), 2.02 (t, 2H, CH_2), 1.65 (s, 2H, CH_2), 1.45 (s, 9H, CH_3), 1.29 (m, 10H, CH_2).

ESI-MS (m/z, ACN/H^+): 415.6 [M+H^+], 437.4 [M+Na^+].

Synthesis of 4,15-dioxo-8,11-dioxa-5,14-diazapentacos-24-enoic acid (C9). The Boc-protected **C8** (260 mg, 0.628 mmol, 1.0 equiv) was dissolved in 15 ml of anhydrous dichloromethane at ice bath, and then a solution of 50% TFA was portionwise added. The reaction was kept at 0 °C for 0.5 hour and stirring was continue for additional 2 hours. The solvent was removed in vacuo and the crude product was used in following step without further purification. To a solution of deprotection of **C8** in 20 ml of anhydrous dichloromethane was added succinic anhydride (125 mg, 1.256 mmol, 2.0 equiv) and triethylamine (5 ml, 3.125 mmol, 5 equiv). The mixture was stirred for 4 hours at room temperature. After which, the solvent was evaporated under vacuum and washed with aqueous HCl (1M, 2 × 10 ml) and extracted with EtOAc. The organic layer was dried over $NaSO_4$ and solvent evaporated. After removing the solvent, the diethyl ether was added into the flask and white solid was observed. The pure compound **C9** (99.85 mg, 90%) was

obtained.

^{1}H-NMR (500 MHz, $CDCl_3$): δ_H (ppm): 6.54 (br, 1H, NH), 6.28 (br, 1H, NH), 5.82 (m, 1H, CH), 4.95 (m, 2H, CH_2), 3.66-3.44 (m, 12H, CH_2O), 2.66 (m. 2H, CH_2), 2.54 (t, 2H, CH_2), 2.19 (t, 2H, CH_2), 2.02 (t, 2H, CH_2), 1.61 (s, 2H, CH_2), 1.29 (m, 10H, CH_2).

ESI-MS (m/z, ACN/H^+): 401.3 [M+H^+], 423.5 [M+Na^+].

6.4.3 Synthesis of diphenyl 1-Amino-2-(4-N, N'-bis(tert-butyloxycarbonyl)guanidino) phenyl)ethanephosphonate

Compound **C15** was prepared according to the following procedure:

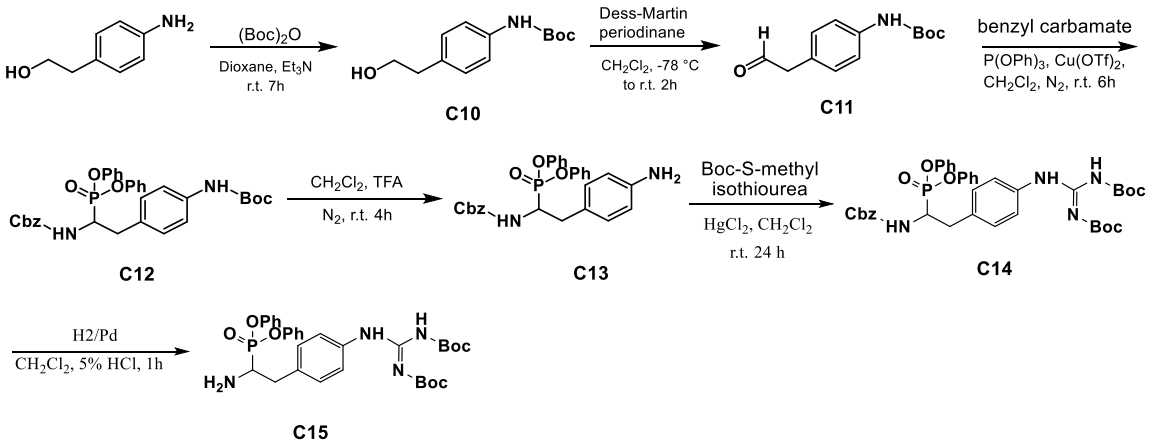

tert-butyl (4-(2-hydroxyethyl)phenyl)carbamate (C10). To a solution of 4-Aminophenethyl alcohol (5.0 g, 36.45 mmol, 1.0 equiv) in dioxane (100 ml), triethylamine (2.0 equiv) and di-*tert*-butyl dicarbonate (8.75 g 40.2 mmol, 1.1 equiv) were added and the reaction stirred at room temperature for 7 hours. The reaction was monitored by TLC in every hour. During the reaction in progress, gas was developing, and a white precipitate appeared. After the competition of reaction, the solvent was removed in vacuo and 2 M aq. HCl (50 ml) was added. The acidified aqueous layer the was extracted with ethyl acetate (3 × 50 ml). The combined organic layers were dried over Na_2SO_4 and the solvent evaporated under reduced pressure, the crude product was purified by flash chromatography (EtOAc/Hexane 1:1), giving 7.495 g (86.7%) of **C10** as a white sloid.

^{1}H-NMR (500 MHz, $CDCl_3$): δ_H (ppm): 7.30 (d, 2H, CHCHNH), 7.17 (d, 2H, CHCHCHNH), 6.49 (br, 1H, NH), 3.86 (t, 2H, CH_2OH), 2.82 (t, 2H, CH_2CH_2OH), 1.56 (s, 9H, CH_3).

ESI-MS (m/z, MeOH/H^+): 238.3 [M+H^+]. 260.4 [M+Na^+].

tert-butyl (4-(2-oxoethyl)phenyl)carbamate (C11). A suspension of alcohol (**C10**) (200 mg, 0.84 mmol, 1.0 equiv) was stirred in 50 ml of anhydrous dichloromethane at -78 °C, a solution of Dess-Martin periodinane (712 mg, 2.0 equiv) in dry dichloromethane was dropwise added. The mixture was stirred for 30 minutes at -78 °C, afterwards the dry ice bath was removed, and the solution was stirred at room temperature for another 1.5 hours. After the competition of reaction, the resulting mixture was poured into saturated $NaHCO_3$ and $Na_2S_2O_3$ solution (1:1, 200 ml) under vigorously stirred for five minutes. The organic layer was separated and, washed with aqueous NaCl and dried over $NaSO_4$. The crude product aldehyde (**C11,** 98.7 mg, 50%) was obtained by evaporated the solvent under vacuum and used in the next step without further purifications.

^{1}H NMR (500 MHz, $CDCl_3$): δ_H (ppm): 9.71 (t, 1H, HCO), 7.34 (d, 2H, CHCHNH), 7.15 (d, 2H, CHCHCHNH), 6.48 (br, 1H, NH), 3.63 (d, 2H, CH_2CO), 1.52 (s, 9H, CH_3).

ESI-MS (m/z, MeOH/H^+): 235.6 [M+H^+], 258.7 [M+Na^+].

tert-butyl(4-(2-(((benzyloxy)carbonyl)amino)-2-(diphenoxyphosphoryl)ethyl)phenyl) carbamate (C12). The crude compound **C11** (252 mg, 1.071 mmol, 1.0 equiv) was dissolved in 50 ml of anhydrous dichloromethane and benzyl carbamate (162 mg, 1.071 mmol, 1.0 equiv), tryphenil phosphite (332 mg, 1.071 mmol, 1.0 equiv) and copper (II) triflate (39 mg, 0.107 mmol, 0.1 equiv) were added with the another 50 ml of dry dichloromethane. The color of mixture became dark brown immediately, and the solution was stirred remained as such at room temperature for 6 hours. Afterwards, the solvent was removed under vacuum, the crude compound dissolved in methanol by heating and after cooling down the solution was kept in the fridge (4°C) overnight until a light brown precipitation of diphenyl phosphonate was complete. The precipitated was filtrated off and crystallized and washed with cold MeOH to give **C12** (258 mg, 40%) as a white solid.

^{1}H NMR (500 MHz, $CDCl_3$): δ_H (ppm): 7.34-7.10 (m, 19H, CH aromatic), 6.46 (s, 1H, C_6H_6NHCO), 5.14-4.69 (m, 3H, CONHCH, $C_6H_6C\mathit{H}_2O$), 3.53-3.33 (m, 2H, $PCHCH_2$), 1.52 (s, 9H, CH_3).

ESI-MS (m/z, ACN/H^+): 603.7 [M+H^+], 625.1 [M+Na^+], 641.1 [M+K^+].

benzyl (2-(4-aminophenyl)-1-(diphenoxyphosphoryl) ethyl)carbamate (C13). To Boc-

protected compound **C12** (100 mg, 0.17 mmol, 1.0 equiv), a solution of 50% TFA (2 ml) in anhydrous dichloromethane (8 ml) was added at 0°C under nitrogen atmosphere. Then the mixture was stirred for 4 hours at room temperature under N_2. After removing the solvent under vacuum, the crude oil product was treated with cold ether, and the formation of a precipitate was observed. The white precipitation was filtrated and used in the following procedures without other purifications.

^{1}H NMR (500 MHz, $CDCl_3$): δ_H (ppm): 7.34-7.10 (m, 19H, CH aromatic), 6.46 (s, 1H, C_6H_6NHCO), 5.10-4.63 (m, 3H, CONHCH, $C_6H_6CH_2O$), 3.53-2.90 (m, 2H, $PCHCH_2$).

ESI–MS (m/z, MeOH/H^+): 503.2 [M+H^+], 525.2 [M+Na^+].

Synthesis of diphenyl 1-(Benzyloxycarbonylamino)-2-(4-N, N'-bis(tert-butyloxy carbonyl)guanidino)phenyl)ethanephosphonate (C14). To a solution of deprotected compound **C13** (85.51 mg, 0.17 mmol, 1.0 equiv) in 10 ml of anhydrous dichloromethane, 1,3-Bis(tert-butoxycarbonyl)-2-methyl-2-thiopseudourea (50 mg, 0.187 mmol, 1.1 equiv) and $HgCl_2$ (138.4 mg, 0.54 mmol, 3.0 equiv) were added and the reaction left stirring overnight at room temperature. After 24 hours other 3 equiv. of $HgCl_2$ were added to help the completion of the product. Afterwards, the solvent was evaporated in vacuo and the crude product was dissolved in 20 ml of ethyl acetate. The resulting solution was washed with aqueous HCl (1 M, 2 × 10 ml), saturated $NaHCO_3$ solution (3 × 20 ml), and brine (3 × 20 ml), the organic layer was finally dried over $MgSO_4$. The solvent was evaporated, and the compound purified by flash column chromatography eluting with EtOAc:Petroleum ether 1:6 to give product **C14** (50.59 mg, 40%) as a white solid.

^{1}H NMR (500 MHz, $CDCl_3$): δ_H (ppm): 7.51-7.10 (m, 19H, CH aromatic), 5.11 (d, 1H, CONHCH), 5.02 (m, 2H, $C_6H_6CH_2O$), 4.79-4.69 (m, 1H, PCH), 3.37-3.02 (m, 2H, $PCHCH_2$), 1.51 (s, 18H, CH_3).

ESI–MS (m/z, MeOH/H^+): 745.5 [M+H^+], 767.4 [M+Na^+].

Synthesis of diphenyl 1-Amino-2-(4-N, N'-bis(tert-butyloxycarbonyl)guanidino)phen yl)ethanephosphonate (C15). The Cbz-protected compound **C11** (100 mg, 0.166 mmol, 1.0 equiv) was dissolved in 20 mL anhydrous ethanol in a two-neck flask, aqueous HCl (1 ml, 5%) and Pd/C (10 mg, 10%, 0.1 equiv) was added. After removing the oxygen with vacuum pump, anhydrous hydrogen was bubbled into the solution with the balloon. The mixture was stirred for 1 h at room temperature. Afterwards, the resulting solution was

filtered over Celite, and the filtrate was evaporated in vacuo. The deprotected product **C15** was used in next step without further purification.

^{1}H NMR (500 MHz, $CDCl_3$): δ_H (ppm): 7.51-7.10 (m, 19H, CH aromatic), 5.11 (d, 1H, CONHCH), 5.02 (m, 2H, $C_6H_6CH_2O$), 4.79-4.69 (m, 1H, PCH), 3.37-3.02 (m, 2H, $PCHCH_2$), 1.51 (s, 18H, CH_3).

ESI–MS (m/z, MeOH/H^+): 611.5 [M+H^+], 633.6 [M+Na^+].

6.4.4 Synthesis of diphenyl (2-(4-guanidinophenyl)-1-((S)-2-((R)-3-hydroxy-2-(4-(27-mercapto-3,6,17-trioxo-10,13-dioxa-2,7,16-Ttriazaheptacosyl)benzamido)propanamido)propanamido)ethyl)phosphonate (thiol 2)

Thiol 2 was prepared according to the following procedure:

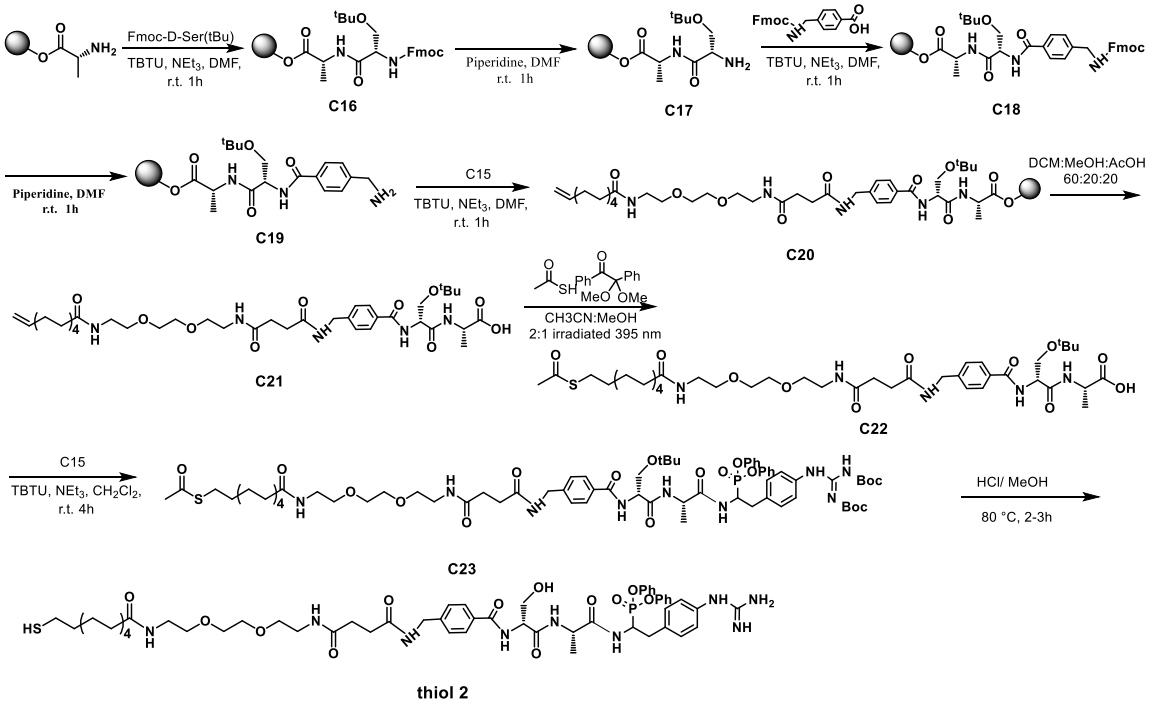

Synthesis of C16. The preparation procedure was based on the standard solid-phase peptide synthesis (SPPS) and Fmoc chemistry on a H-L-Ala -2-chlorotrityl chloride resin. The dry resin (100 mg, 0.065 mmol, 1.0 equiv) was swelled with DMF for 30 minutes. Later, Fmoc-D-Ser (tBu) (50 mg, 0.13 mmol, 2.0 equiv), HBTU (49.3 mg, 0.13 mmol, 2.0 equiv) and DIPEA (45 µl, 0.26 mmol, 4.0 equiv) were added in a reactor containing the resin and mixed for 1 hour. Afterwards, the reaction was monitored by using Kaiser kit for

displaying pale yellow.

Synthesis of C17. The resin (C**16**) was washed with DMF (3 ×), DCM (3 ×), the Fmoc protecting group was removed with a solution of 20% piperidine in DMF, after 1 hour following the deprotection of Fmoc, the resin was dried and rinsed with DMF (3 ×), DCM (2 ×), MeOH (1 ×) and Et_2O. The color of solution was blue by treated with Kaiser kit under heated.

Synthesis of C18. To the reaction container, a solution of Fmoc protected 4-(Aminomethyl)benzoic acid (48.5 mg, 0.13 mmol, 2.0 equiv), HBTU (49.3 mg, 0.13 mmol, 2.0 equiv), and DIPEA (45 µl, 0.26 mmol, 4.0 equiv) in anhydrous DMF were added, the reaction mixture was stirred for 1 hour at room temperature. After which, the solvent was removed by N_2 flow and washed by DCM (3 ×).

Synthesis of C19. The product **C18** was treated by a solution of 20% piperidine in DMF, the reaction container was stirred for 1 hour, afterwards, the resin was dried and rinsed with DMF (3 ×), DCM (2 ×), MeOH (1 ×) giving the product **C19**. The color of solution was blue by treated with Kaiser kit under heated.

Synthesis of C20. To the reaction container, a solution of **C9** (53.9 mg, 0.23 mmol, 2.0 equiv), HBTU (49.3 mg, 0.13 mmol, 2.0 equiv), and DIPEA (45 µl, 0.26 mmol, 4.0 equiv) in anhydrous DMF were added, the mixture was stirred for 1 hour and washed by DMF (3 ×), DCM (2 ×).

Synthesis of O-(tert-butyl)-N-(4-(3,6,17-trioxo-10,13-dioxa-2,7,16-triazaheptacos-26-en-1-yl)benzoyl)-D-seryl-L-alanine (C21). Cleavage of side chain protected linear peptide from 2-chlorotrityl chloride resin. The peptidyl resin was treated at room temperature with AcOH/MeOH/DCM (2:2:6) for 2 hours. The resin was removed by filtration and washed 3 times with the cleaving mixture and 2 times with DCM. The solvent was evaporated under vacuum affording the crude product. All the products were purified by flash chromatography.

ESI–MS (m/z, MeOH/H^+): 762.5 [$M+H^+$], 784.6 [$M+Na^+$].

Synthesis of O-(tert-butyl)-N-(4-(3,6,17,29-tetraoxo-10,13-dioxa-28-thia-2,7,16-triaza triacontyl)benzoyl)-D-seryl-L-alanine (C22). C21 (115 mg, 0.151 mmol, 1 equiv) was dissolved in methanol (3 mL) and the solution was degassed for 10 min under nitrogen.

Afterwards, 2,2-Dimethoxy-2-phenylacetophenone (2.0 mg, 0.007 mmol, 0.05 equiv) and ethanethioic S-acid (45.9 mg, 0.548 mmol, 4 equiv) were added and the mixture was stirrend under irradiation (365 nm) for overnight. After solvent evaporation, the crude product was purified by flash chromatography (EtOAc/Hexane 4:1). 60 mg (48%) of **C22** were obtained.

ESI–MS (m/z, MeOH/H^+): 838.6 [M+H^+], 860.5 [M+Na^+].

Synthesis of S-(1-(4-(((2R)-1-(((2S)-1-((2-(4-((Z)-2,3-bis(tert-butoxycarbonyl)guanidino)phenyl)-1-(diphenoxyphosphoryl)ethyl)amino)-1-oxopropan-2-yl)amino)-3-(tert-butoxy)-1-oxopropan-2-yl)carbamoyl)phenyl)-3,6,17-trioxo-10,13-dioxa-2,7,16-triazaheptacosan-27-yl) ethanethioate (C23). C22 (20.19 mg, 0.0134 mmol, 1.0 equiv), EDAC (2.56 mg, 0.0134 mmolo, 1.0 equiv) and HOBt (1.8 mg, 0.0134 mmol, 1.0 equiv) were dissolved in dry dichloromethane (5 ml). After 30 minutes stirring, **C15** (10 mg, 0.0134 mmol, 1.0 equiv) was added. The mixture was stirred for 4 hours under nitrogen at room temperature. After solvent evaporation, the crude product was purified by flash chromatography (MeOH/ DCM 0.5:9.5 → 1:9). 13.4 mg (70%) of **C23** were obtained.

ESI–MS (m/z, MeOH/H^+): 1430.7 [M+H^+], 1452.6 [M+Na^+].

Synthesis of diphenyl (2-(4-guanidinophenyl)-1-((S)-2-((R)-3-hydroxy-2-(4-(27-mercapto-3,6,17-trioxo-10,13-dioxa-2,7,16-Ttriazaheptacosyl)benzamido)propanamido)propanamido)ethyl)phosphonate (thiol 2). C23 (50 mg, 0.035 mmol) was dissolved in ethanol (2.0 mL). A 6 M HCl solution in water (2.0 mL) was added and the mixture was stirred at 80 °C for 2 hours under nitrogen. The reaction mixture was allowed to cool and the solvent was evaporated to obtain 38.42 mg (97%) of thiol **2**.

ESI–MS (m/z, MeOH/H^+): 1132.4 [M+H^+], 1154.7 [M+Na^+].

6.4.5 Synthesis of the peptides A and B sequence.

Peptides **A** and **B** series were prepared according to the following procedure:

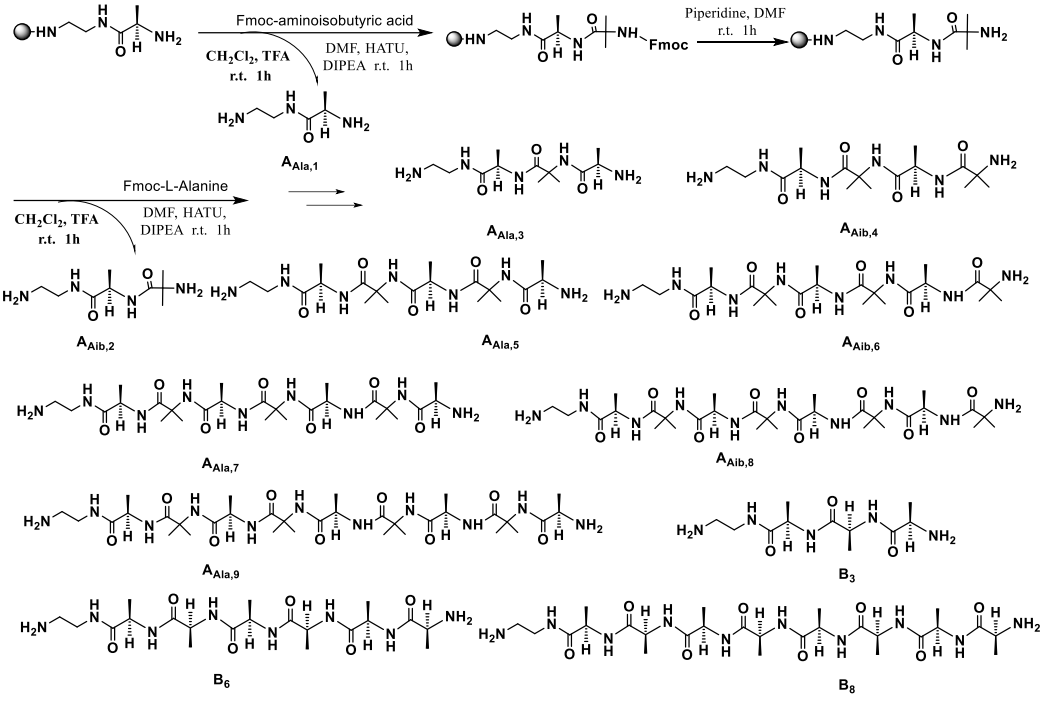

Synthesis of $A_{Ala,1}$. The $A_{Ala,1}$ was prepared by using standard solid-phase peptide synthesis (SPPS) and Fmoc chemistry on a 2-chlorotrityl chloride resin. The dry 2-chlorotrityl chloride resin (1.0 g, loading 1.6 mmol/g, 1.0 equiv) was swelled with DMF for 30–45 minutes before use. After linking ethylenediamine to the resin, Fmoc-L-Alanine (995 mg, 3.2 mmol, 2.0 equiv), HOAt (871 mg, 6.4 mmol, 4.0 equiv), HATU (2.4 g, 6.4 mmol, 4.0 equiv) and DIPEA (1.1 ml, 6.4 mmol, 4.0 equiv) were added in a reactor containing the resin and mixed for 2 hours. Afterwards, the reaction was monitored by using Kaiser kit for displaying pale yellow. Then the resin was washed with DMF (3 ×), DCM (3 ×), the Fmoc protecting group was removed with a solution of 20% piperidine in DMF, after 1 hour following the deprotection of Fmoc, the resin was dried and rinsed with DMF (3 ×), DCM (2 ×), MeOH (1 ×). The color of solution was blue by treated with Kaiser kit under heated.

Then the resin was treated at room temperature with AcOH/MeOH/DCM (2:2:6) for 2 hours. The resin was removed by filtration and was dried and rinsed with DMF (3 ×), DCM (2 ×), MeOH (1 ×). The solvent was evaporated under vacuum affording the crude product and purified by reversed phase chromatography to give $A_{Ala,1}$.

Synthesis of $A_{Aib,2}$. To the reaction container, a solution of peptidyl resin ($A_{Ala,1}$) (1.0 g,

loading 1.6 mmol/g, 1.0 equiv), Fmoc-Aib-OH (1.041 g, 3.2 mmol, 2.0 equiv), HOAt (871 mg, 6.4 mmol, 4.0 equiv), HATU (2.4 g, 6.4 mmol, 4.0 equiv) and DIPEA (1.1 ml, 6.4 mmol, 4.0 equiv) were added, the reactor was stirred at room temperature for 2 hours. Afterwards, the reaction was monitored by using Kaiser kit for displaying pale yellow. Then the resin was washed with DMF (3 ×), DCM (3 ×) under N_2 flow, the Fmoc protecting group was removed with a solution of 20% piperidine in DMF, after 1 hour following the deprotection of Fmoc, the resin was dried and rinsed with DMF (3 ×), DCM (2 ×), MeOH (1 ×). The color of solution was blue by treated with Kaiser kit under heated.

Then the resin was treated at room temperature with AcOH/MeOH/DCM (2:2:6) for 2 hours. The resin was removed by filtration and was dried and rinsed with DMF (3 ×), DCM (2 ×), MeOH (1 ×). The solvent was evaporated under vacuum affording the crude product and purified by reversed phase chromatography to give $A_{Aib,2}$.

Synthesis of $A_{Ala,3}$, $A_{Aib,4}$, $A_{Ala,5}$, $A_{Aib,6}$, $A_{Ala,7}$, $A_{Aib,8}$, $A_{Ala,9}$ and B_3, B_6, and B_8

Successive amino acids were added step-by step, by using the above protocol: 4.0 equiv (relative to the resin loading) of Fmoc-protected amino acid were activated with 4.0 equiv of HOAt, 4.0 equiv of HATU and 8 equiv of DIPEA in DMF. This mixture was added in a reactor containing the resin-bound peptide and mixed for 2 hours under N_2 flux. In each step, the Fmoc protecting group was removed with a solution of 20% piperidine in DMF. After each chain-extension step, and following the deprotection of Fmoc, a part of the resin was dried and rinsed with DMF (3 ×), DCM (2 ×), MeOH (1 ×). Finally, the relative resin-bound peptide was unblocked with a mixture 18:2 (v/v) of DCM/TFA. The peptide A series 3-9 and B series were obtained in high purity. They were treated with a basic resin prior to use.

6.4.6 Synthesis of N-(8-aminooctyl)-4-(pyren-4-yl)butanamide (indicator 1) and N-(8-(2-aminoacetamido)octyl)-4-(pyren-4-yl)butanamide (indicator 2)

Indicator **1** and **2** was prepared according to the following procedure:

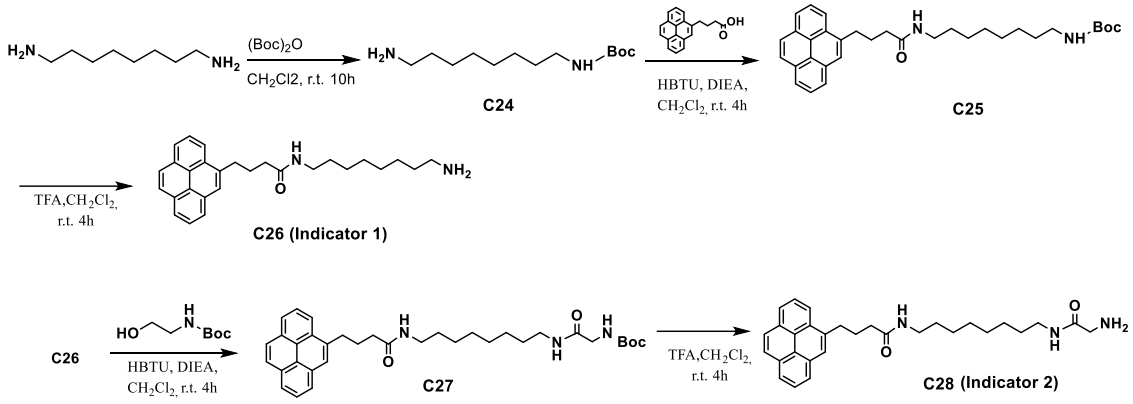

Synthesis of tert-butyl (8-aminooctyl)carbamate (C24). C24 was obtained by mono-protection of the proper diamine with Boc. 1,8-Diaminooctane (4.0 g, 27.7 mmol, 1.0 equiv) was dissolved in 50 ml of anhydrous dichloromethane at ice bath. And then a solution of Boc_2O (1.815 g, 8.3 mmol, 0.3 equiv) in CH_2Cl_2 was added dropwise over a 2 hours period. The reaction mixture was stirred for 10 hours at room temperature. After which, the solvent was evaporated under vacuum and the resulting oil dissolved in EtOAc (400 mL), which was washed with half-saturated brine (3 × 150 mL), dried ($MgSO_4$) and concentrated under vacuum to afford crude mono-Boc-protected diamine. Purification by flash chromatography on silica with CH_2Cl_2/ MeOH (7:1) yielded **C24** as a colorless oil (70 %).

^{1}H NMR (500 MHz, $CDCl_3$): δ_H (ppm): 3.07 (t, 2H, CH_2,), 2.64 (t, 2H, CH_2,), 1.60-1.42 (m, 14H, CH_2, CH_3,), 1.28 (s, 8H, CH_2).

ESI–MS (m/z, MeOH/H^+): 245.3 [M+H^+], 267.4 [M+Na^+].

Synthesis of tert-butyl (8-(4-(pyren-4-yl)butanamido)octyl)carbamate (C25): To a round bottom flask (100 ml) with stirring bar and 50 ml of anhydrous dichloromethane, 1-pyrenebutyric acid (118 mg, 0.4 mmol, 1.0 equiv) and HBTU (182 mg, 0.48 mmol, 1.2 equiv), DIEA (100 µl, 0.48 mmol, 1.2 equiv) were added and stirred for half an hour, and then N-Boc-1,8-diaminooctane (**C24**) (100 mg, 0.4 mmol, 1.0 equiv) were added. The mixture was stirred at room temperature for 4 hours. The crude solution was concentrated under vacuum and the resulting oil dissolved in EtOAc (50 mL) and extracted with half-saturated brine (3×50 mL), dried (Na_2SO_4) and concentrated under vacuum to afford crude product. Purification by flash chromatography on silica with CH_2Cl_2/ EtOAc (4:1) yielded **C25** as a colorless powder (89%).

^{1}H NMR (500 MHz, $CDCl_3$): δ_H (ppm): 8.30-7.83 (m, 9H, CH aromatic), 6.08 (br, 1H, NH), 5.68 (br, 1H, NH), 3.70 (t, 2H, CH_2), 3.39 (t, 2H, CH_2), 3.20 (m, 4H, CH_2), 2.29-2.02 (m, 4H, CH_2), 1.84 (s, 4H, CH_2), 1.43 (s, 9H, CH_3), 1.24 (s, 10H, CH_2).
ESI–MS (m/z, MeOH/H^+): 515.3 [M+H^+], 537.2 [M+Na^+].

Synthesis of N-(8-aminooctyl)-4-(pyren-4-yl)butanamide (C26) Indicator 1: The Boc-protected compound (**C25**) (100 mg, 0.2 mmol, 1.0 equiv) was dissolved in 50% TFA in anhydrous dichloromethane (5 mL). After stirring for 3 hours at room temperature, the solvent was evaporated under vacuum pump. The crude oil was washed with cold ether giving a white solid. Compound C26 was used without further purification.
^{1}H NMR (500 MHz, $CDCl_3$): δ_H (ppm): 8.35-7.84 (m, 9H, CH aromatic), 3.71 (t, 2H, CH_2), 3.39 (t, 2H, CH_2), 3.21 (m, 4H, CH_2), 2.28-2.21 (m, 4H, CH_2), 1.25 (s, 101H, CH_2).
ESI–MS (m/z, MeOH/H^+): 415.3 [M+H^+], 437.4 [M+Na^+].

Synthesis of tert-butyl (2-oxo-2-((8-(4-(pyren-4-yl)butanamido)octyl)amino)ethyl)carbamate (C27). N-(tert-Butoxycarbonyl)-Glycine (35 mg, 0.2 mmol, 1.0 equiv) and HBTU (90.96 mg, 0.24 mmol, 1.2 equiv), DIEA (60 µl, 0.24 mmol, 1.2 equiv) were dissolved in 10 ml of anhydrous dichloromethane and stirred for half an hour, and then **C26** (83 mg, 0.2 mmol, 1.0 equiv) were added and the mixture was stirred at room temperature for 4 hours. The crude solution was concentrated under vacuum and dissolved in EtOAc (50 mL), washed with half-saturated brine (3×50 mL), dried (Na_2SO_4) and concentrated under vacuum to afford crude product. Purification by flash chromatography on silica with CH_2Cl_2/ EtOAc (2:1) yielded **C27** as a colorless powder (91%).
^{1}H NMR (500 MHz, $CDCl_3$): δ_H (ppm): 8.44-7.86 (m, 9H, CH aromatic), 6.04 (br, 1H, NH), 5.61 (br, 1H, NH), 3.70 (t, 2H, CH_2), 3.41 (t, 2H, CH_2), 3.22 (m, 4H, CH_2), 2.31-2.23 (m, 4H, CH_2), 1.84 (s, 4H, CH_2), 1.44 (s, 9H, CH_3), 1.26 (s, 12H, CH_2).
ESI–MS (m/z, MeOH/H^+): 571.4 [M+H^+], 594.3 [M+Na^+].

Synthesis of N-(8-(2-aminoacetamido)octyl)-4-(pyren-4-yl)butanamide (C28) Indicator 2. The indicator was prepared by the same method as C26. The Boc-protected compound **C27** (30 mg, 0.063 mmol, 1.0 equiv) was dissolved in 50% TFA in anhydrous dichloromethane (5 mL). After stirring for 4 h at room temperature, the solvent was evaporated via rotary evaporator and a light-yellow oil was obtained. This raw product

was dissolved in 60 ml EtOAc and washed three times with sodium hydrogen carbonate solution, dried (Na_2SO_4) and concentrated under vacuum to afford pure product as a pale yellow solid and with 88% yield.

^{1}H NMR (500 MHz, $CDCl_3$): δ_H (ppm): 8.28-7.62 (m, 9H, CH aromatic), 4.58 (m, 4H, CH_2), 2.08 (m, 2H, CH_2), 1.92 (m, 2H, CH_2), 1.28 (s, 4H, CH_2), 1.13 (s, 10H, CH_2).

ESI–MS (m/z, MeOH/H^+): 471.3 [M+H^+], 494.4 [M+Na^+].

Acknowledgement

There are so many people whom I would like to take this opportunity to thank for their valuable support and encouragement in the life of my PhD project. First, I wish to express my deepest gratitude to my supervisor Prof Paolo Scrimin for his valuable guidance, patience, inspiration and understanding. His friendly support enables me to develop the understanding of the way how to become a more conscientious and excellent mentor. I have been extremely fortunate to explore the novel specific question in his pleasurable lab environment over the past three years. This thesis would not have been possible without his endless professional support.

I owe my thanks to Prof. Fabrizio Mancin, Prof. Alessandro Moretto, Prof. Federico Rastrelli, Prof. Stefano Corni, Prof. Gaetano Granozzi, Prof. Fernando Formaggio, Dr. Marta De Zotti, Dr. Giulia Marafon and all the people with whom I have been cooperating with. I am also grateful to my PhD project commission members: Prof. Polimeno Antonino, Prof. Zoleo Alfonso and Prof. Pasut Gianfranco for their productive scientific discussion and useful suggestion on my PhD projects.

I would like to express my special thanks to Álvaro Martínez, who taught me many useful experimental skills and friendly help when I joined the lab, and I am grateful to Jakub Trzcinski, Xiaohuan Sun, Daniele Rosa-Gastaldo, Lucia Morillas, Joanna Czescik, Giordano Zanoni, Wenwen Fei, Meng Zheng, Jiaying Yu, Rui Chen, Jiajia Ran, Jie Luo, Panjuan Tang, Chuanyu Sun and all the other people who have worked with me and made my life at Padova much more colourful. I am grateful to all the staff of Department of Molecular Science at University of Padova for their kind help.

I would particularly like to express my sincere thanks to China Scholarship Council for the funding of my fellowship.

Finally, deepest gratitude to my parents for their love, supporting and understanding, and special thanks to my sister who has put many efforts into taking care of my parents. I would like to send endless love to my wife, Qingqing Sun, who is a beautiful, diligent and kind girl. Thank you for your love and constant support from early morning to midnight. Thank you for being my life partner, I owe you everything.

Appendix

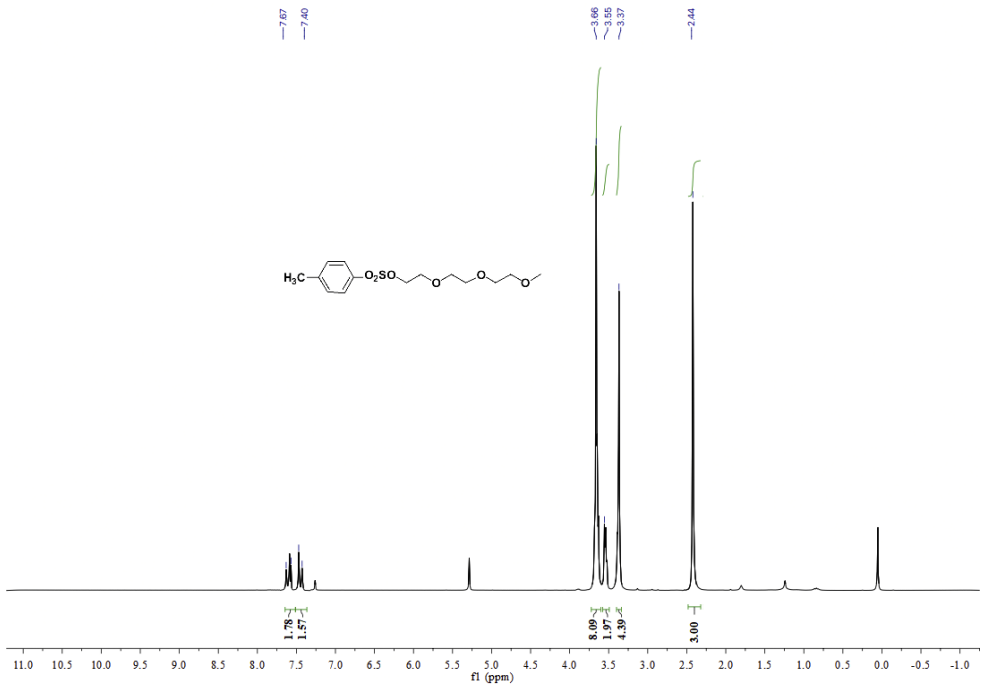

Figure A1. ^{1}H NMR spectrum of compound C1.

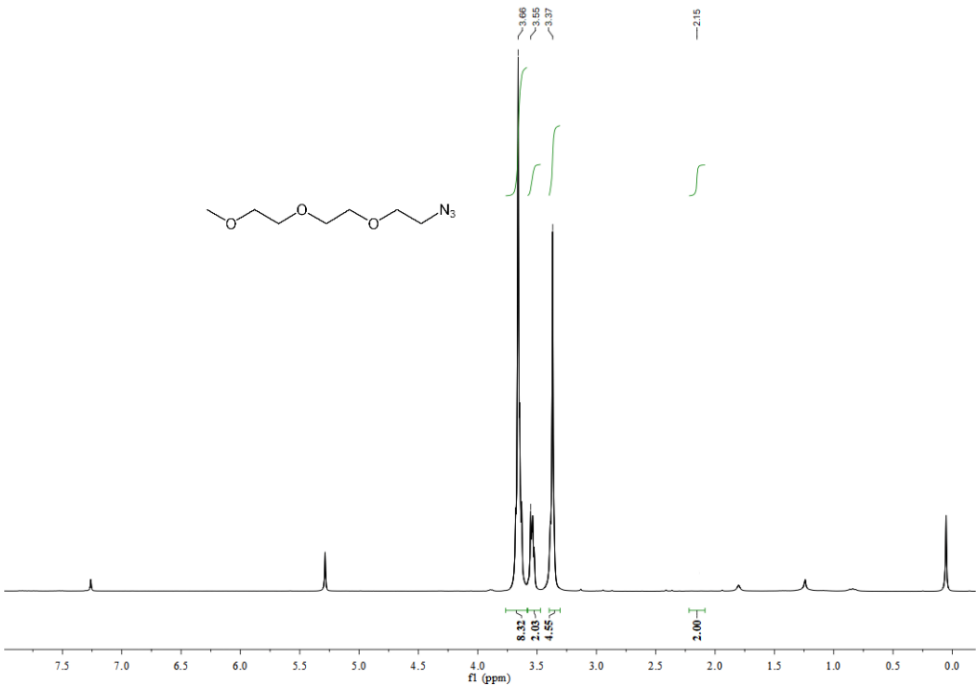

Figure A2. ^{1}H NMR spectrum of compound C2.

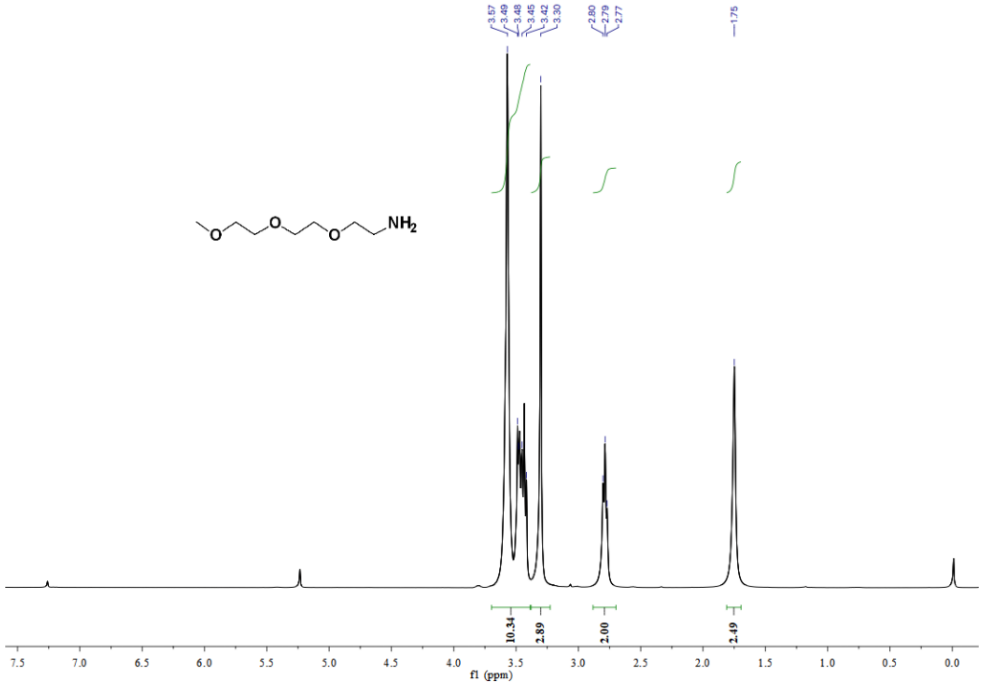

Figure A3. ^{1}H NMR spectrum of compound C3.

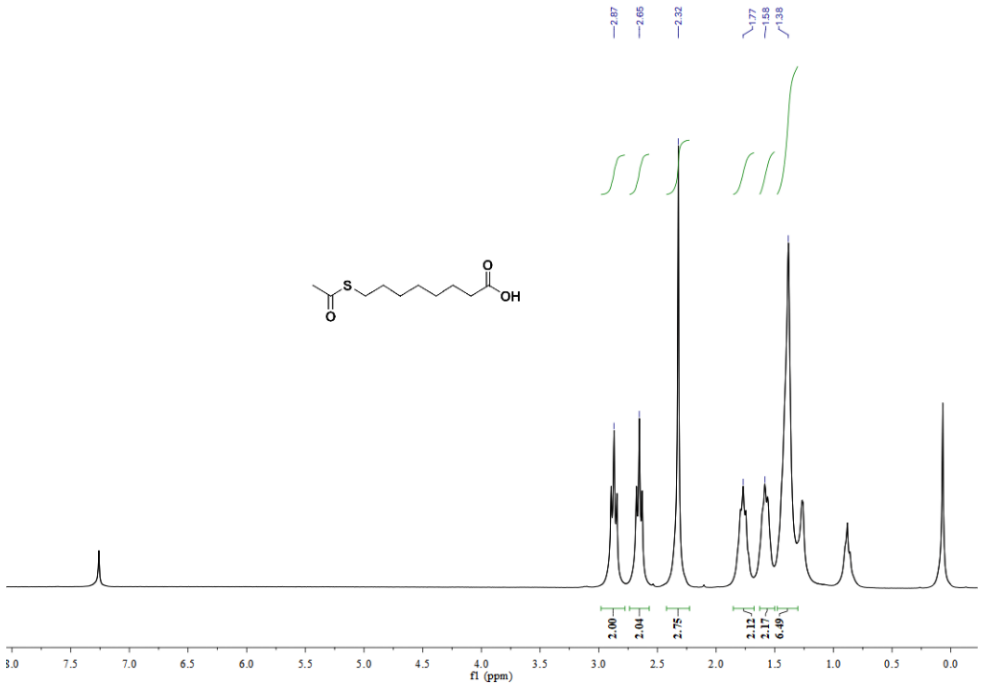

Figure A4. ^{1}H NMR spectrum of compound C4.

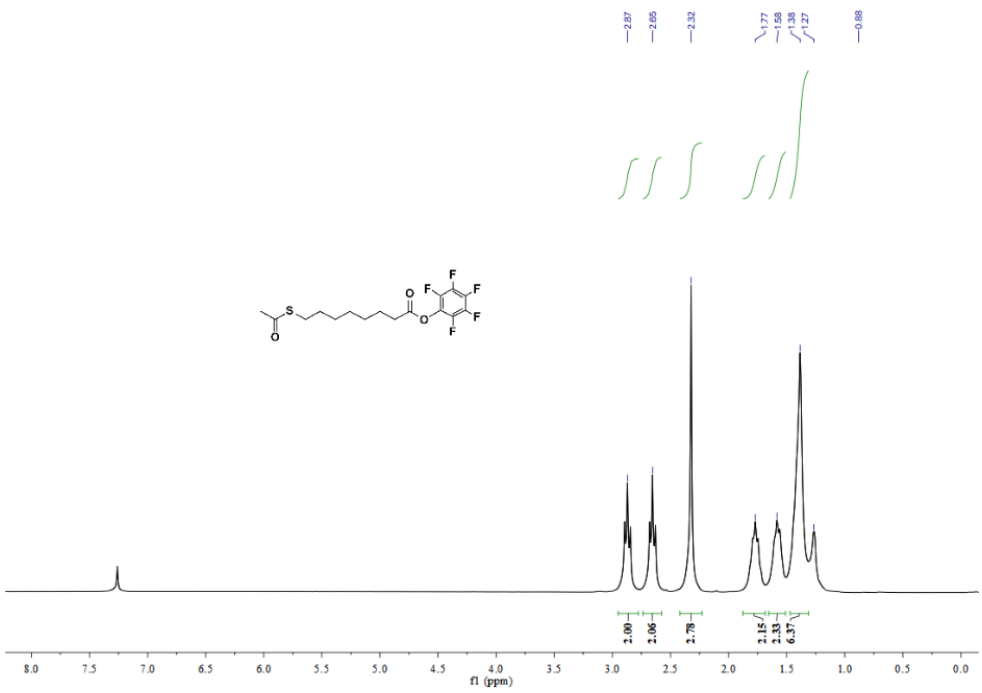

Figure A5. ^{1}H NMR spectrum of compound C5.

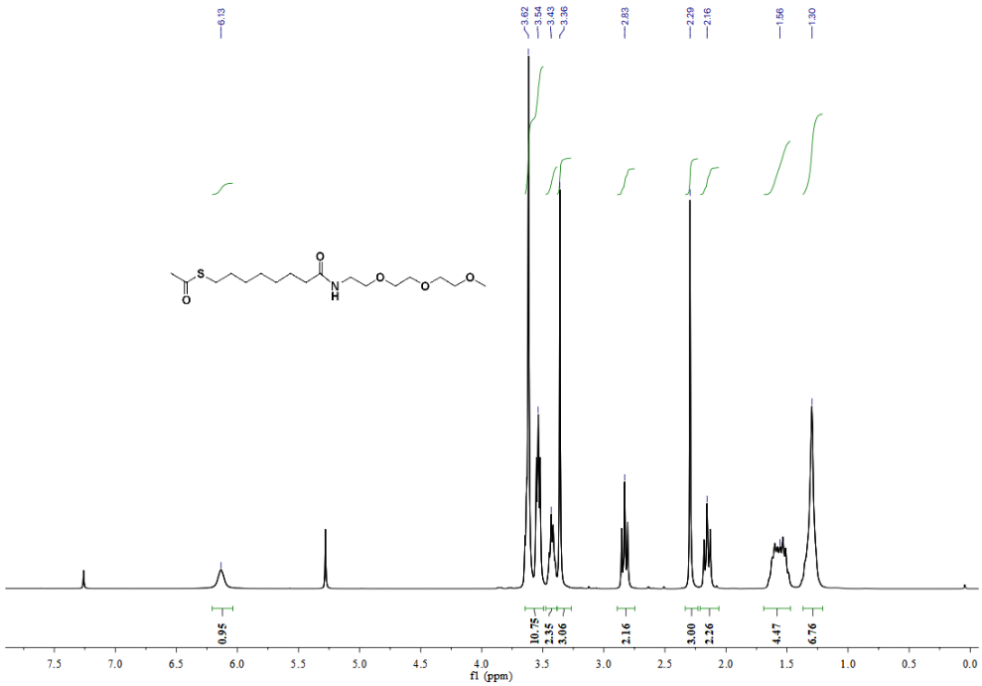

Figure A6. ^{1}H NMR spectrum of compound C6.

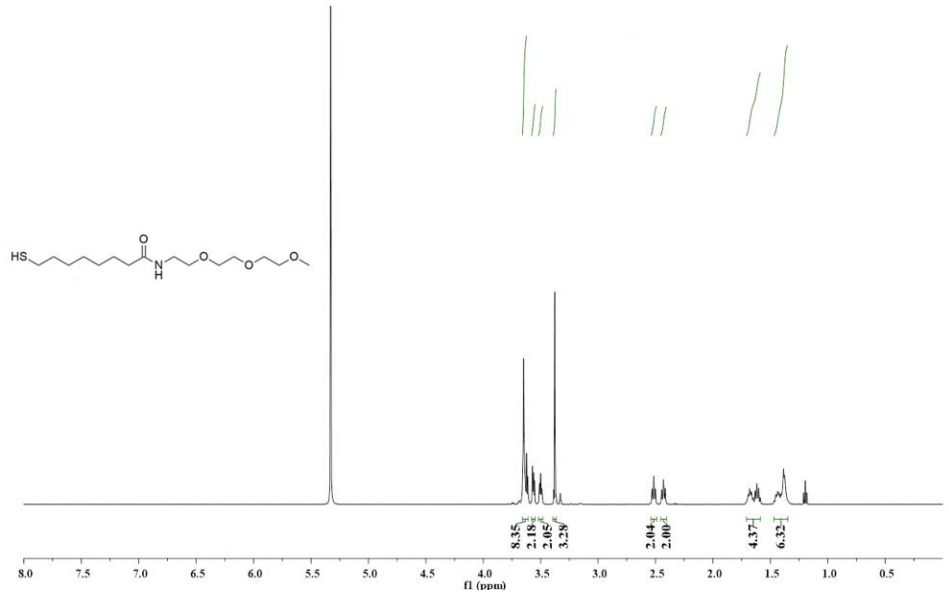

Figure A7. ^{1}H NMR spectrum of **thiol 1**.

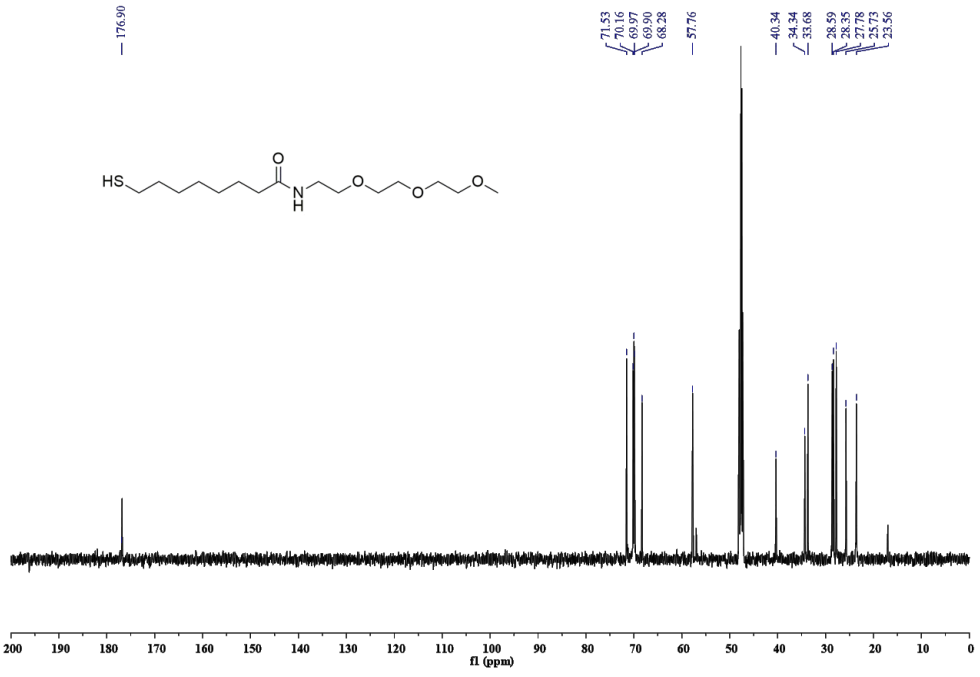

Figure A8. ^{13}C NMR spectrum of **thiol 1**.

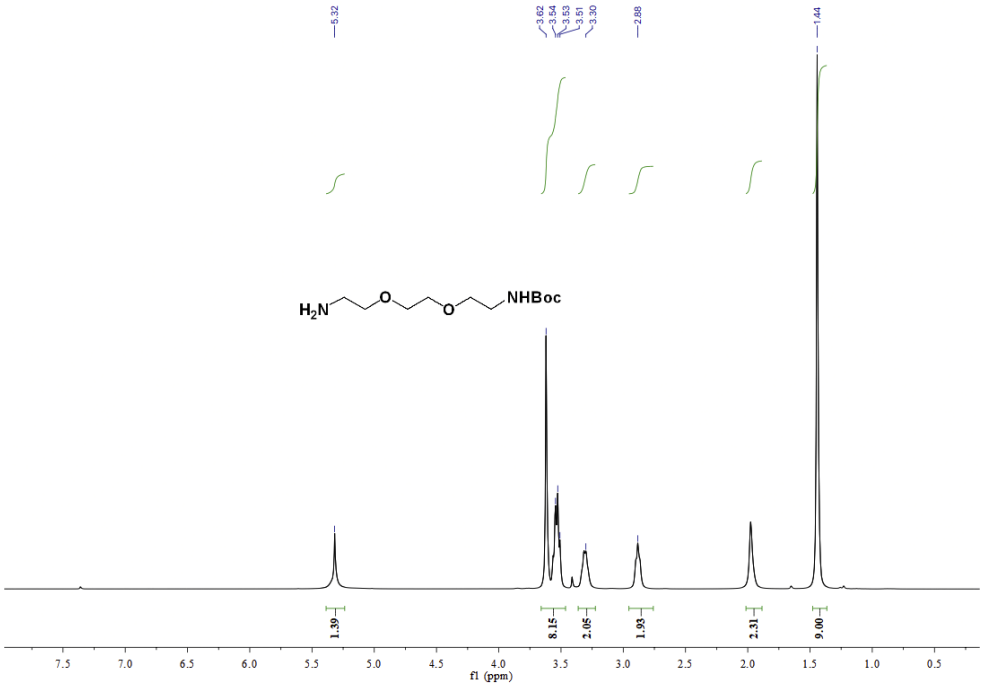

Figure A9. ^{1}H NMR spectrum of **C7**.

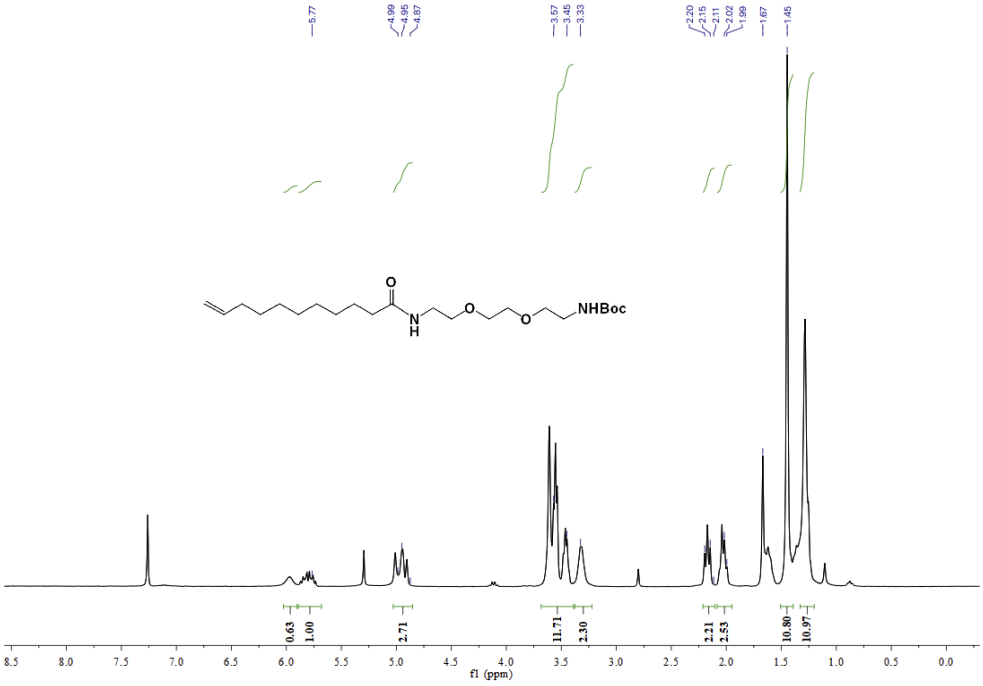

Figure A10. ^{1}H NMR spectrum of **C8**.

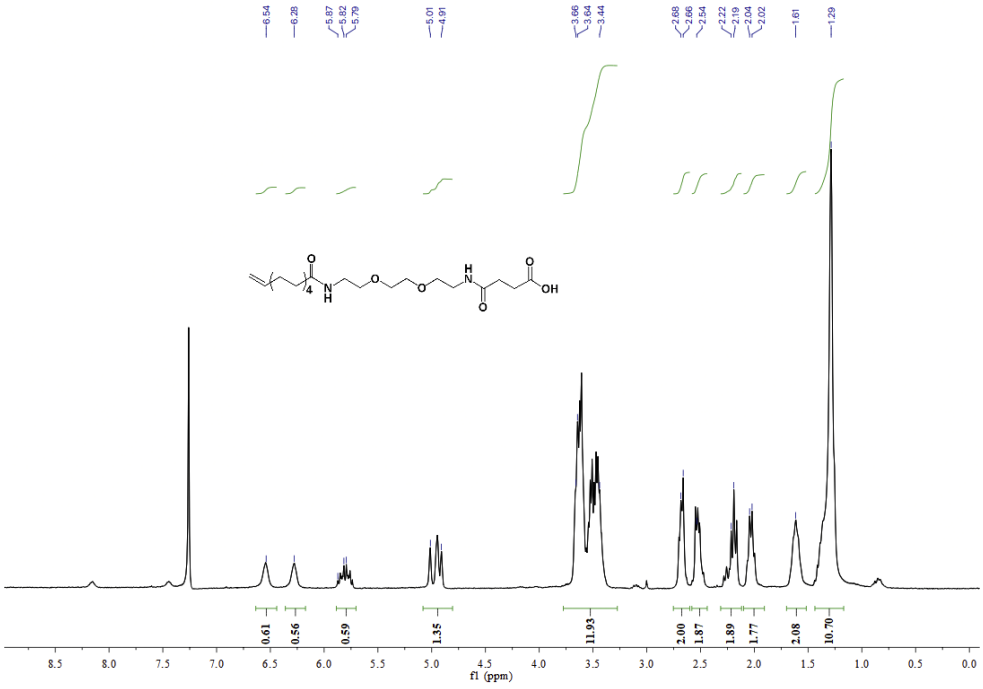

Figure A11. ^{1}H NMR spectrum of **C9**.

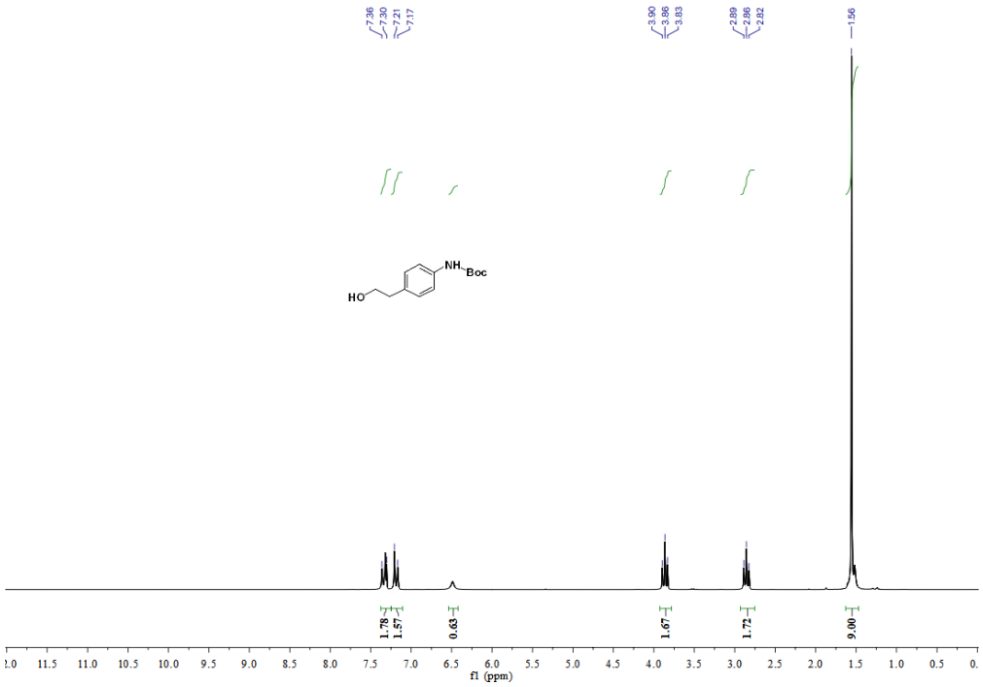

Figure A12. ^{1}H NMR spectrum of **C10**.

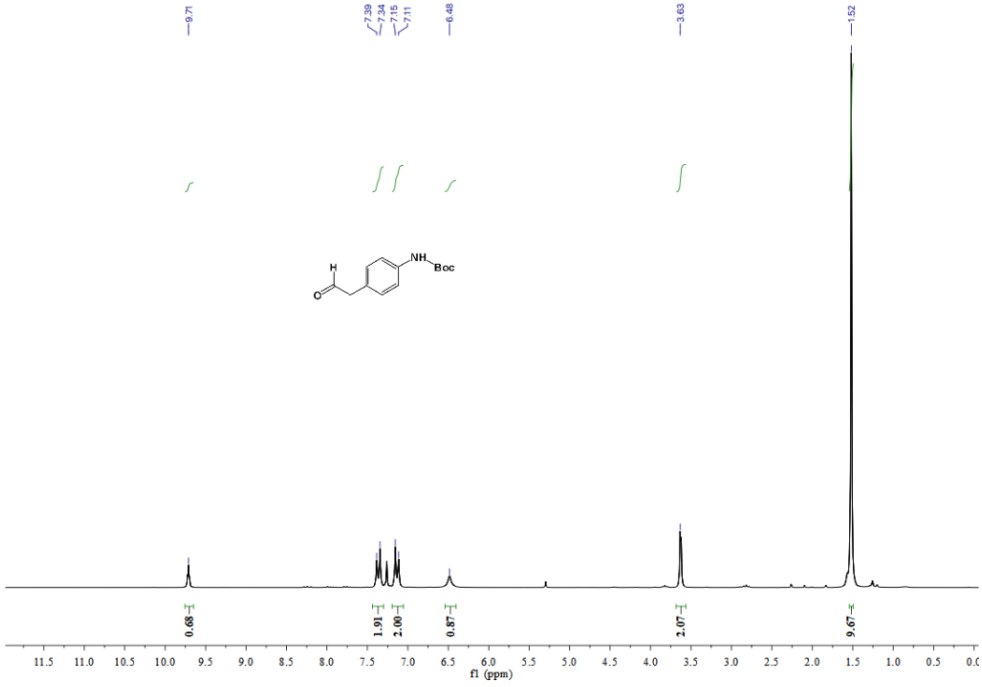

Figure A13. ^{1}H NMR spectrum of **C11**.

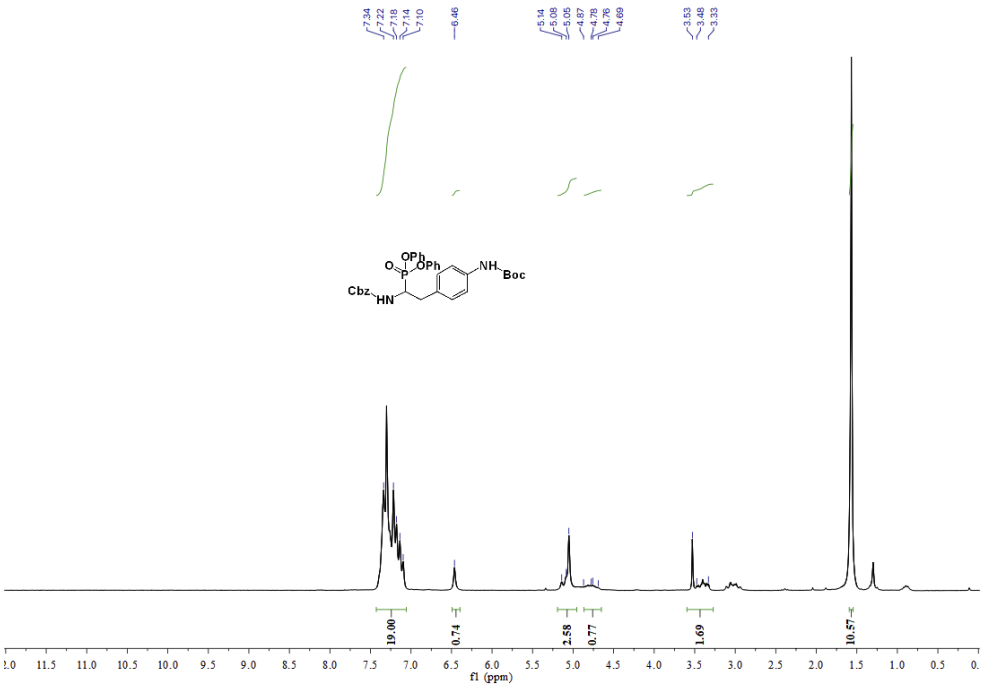

Figure A14. ^{1}H NMR spectrum of **C12**.

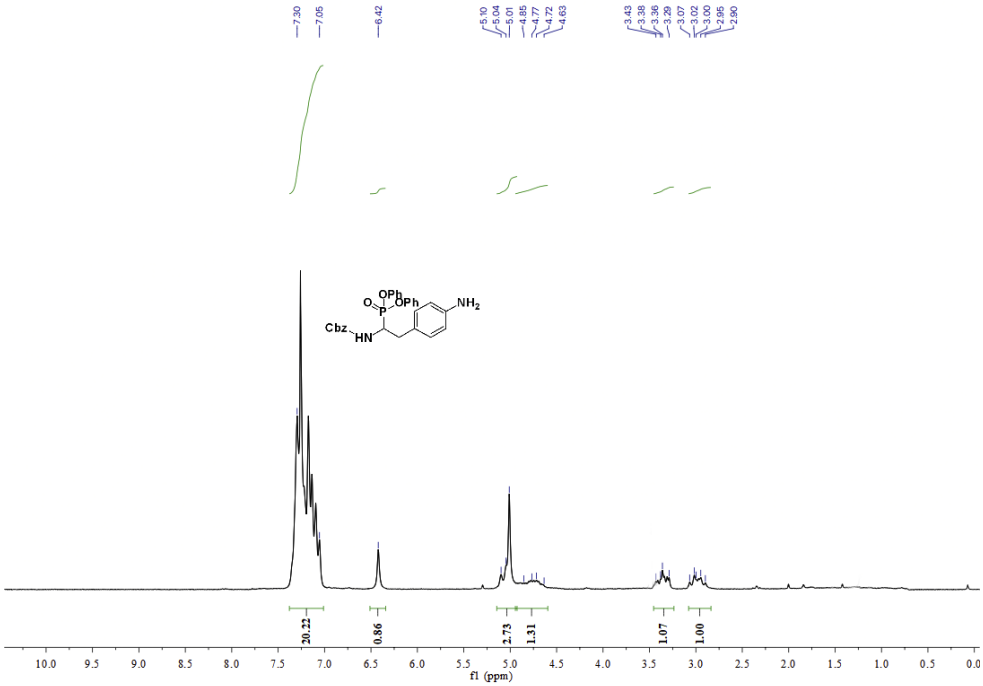

Figure A15. ^{1}H NMR spectrum of **C13**.

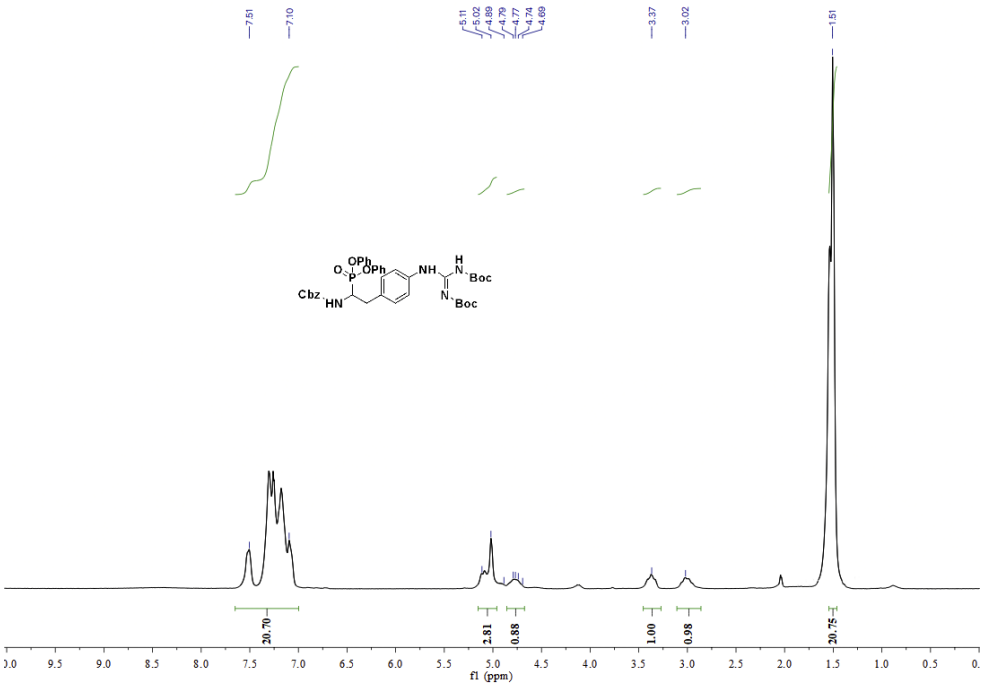

Figure A16. ^{1}H NMR spectrum of **C14**.

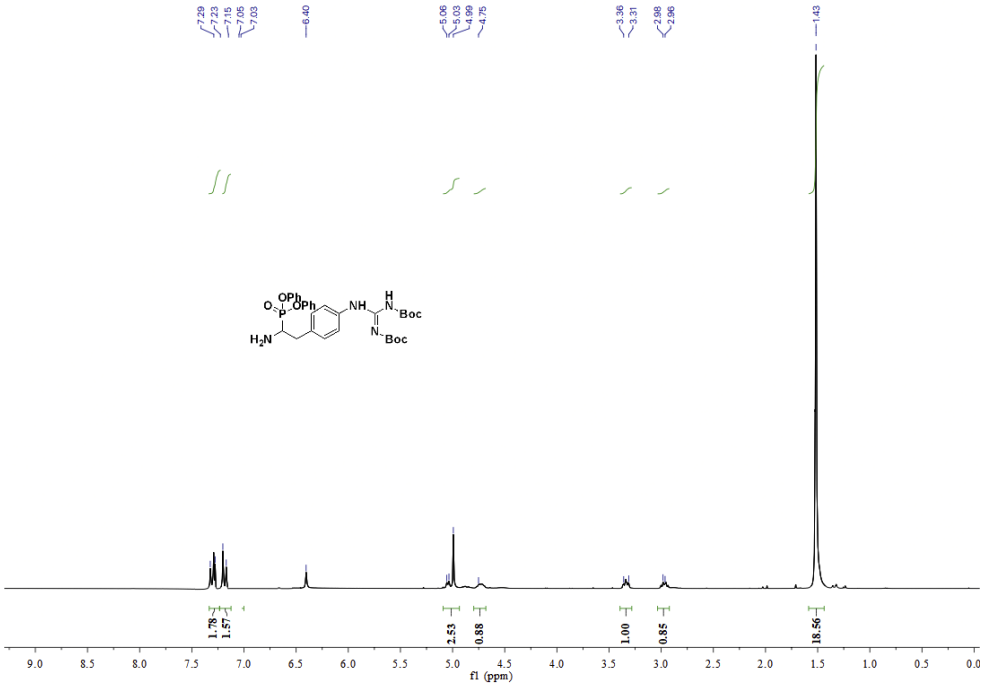

Figure A17. ^{1}H NMR spectrum of **C15**.

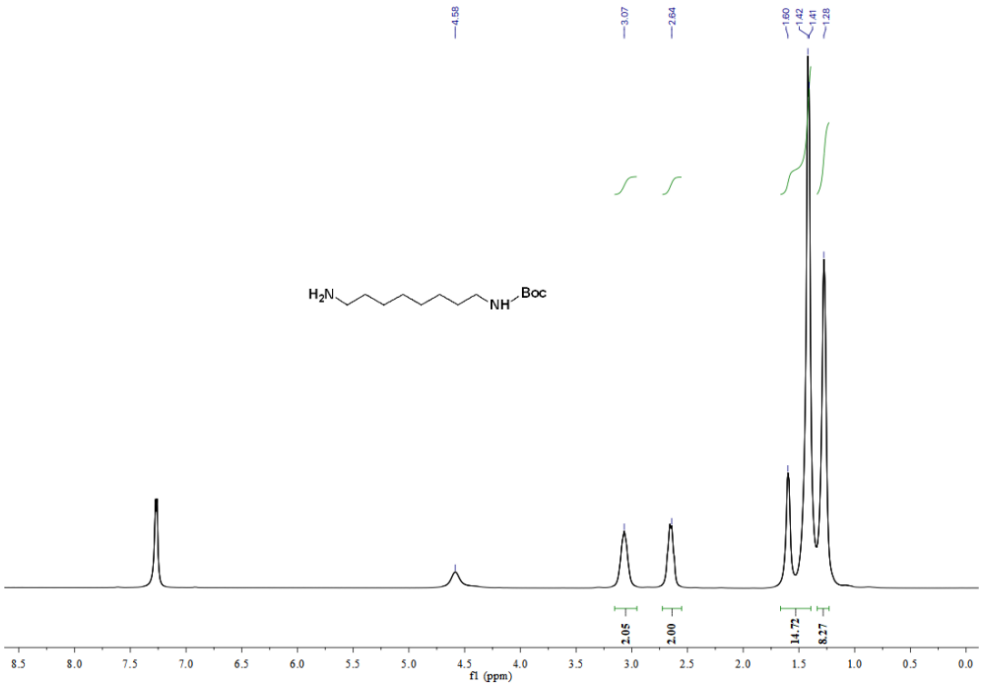

Figure A18. ^{1}H NMR spectrum of **C24**.

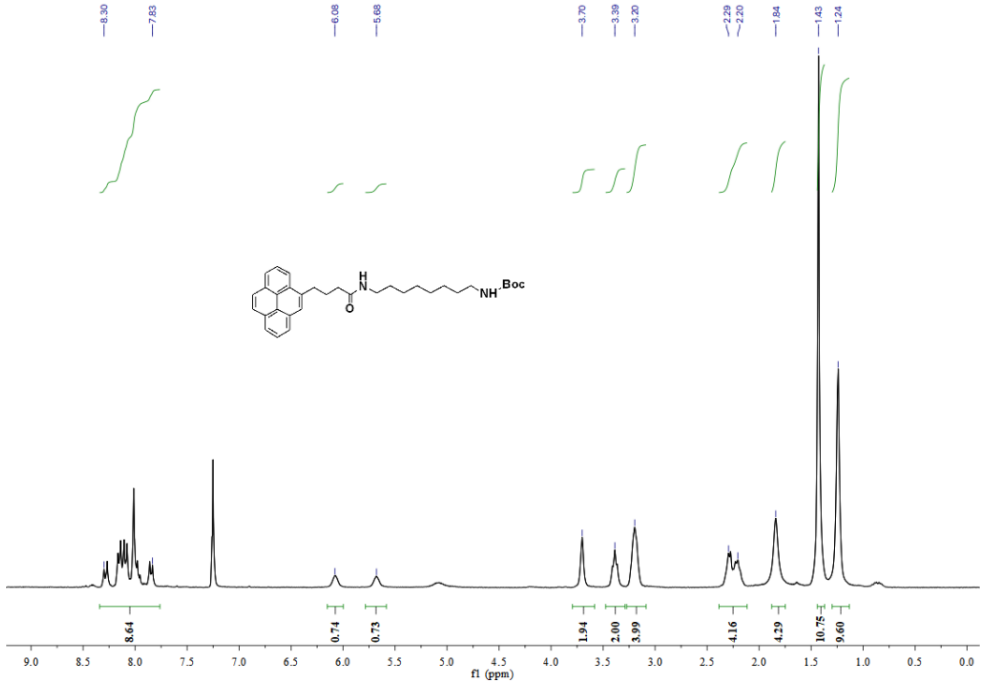

Figure A19. ^{1}H NMR spectrum of **C25**.

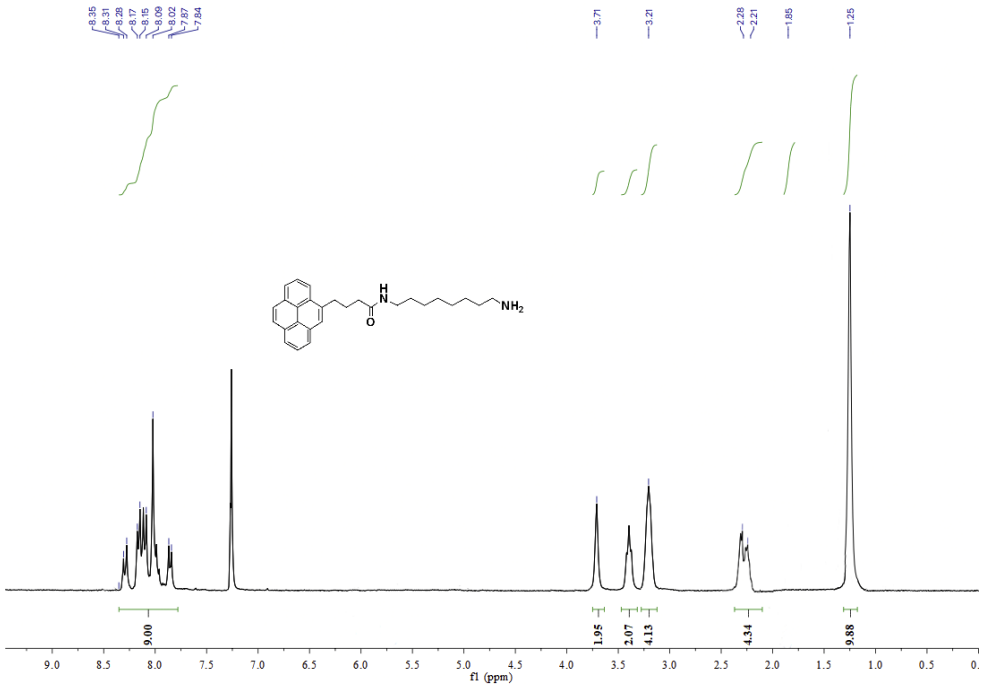

Figure A20. ^{1}H NMR spectrum of **C26** (Indicator 1).

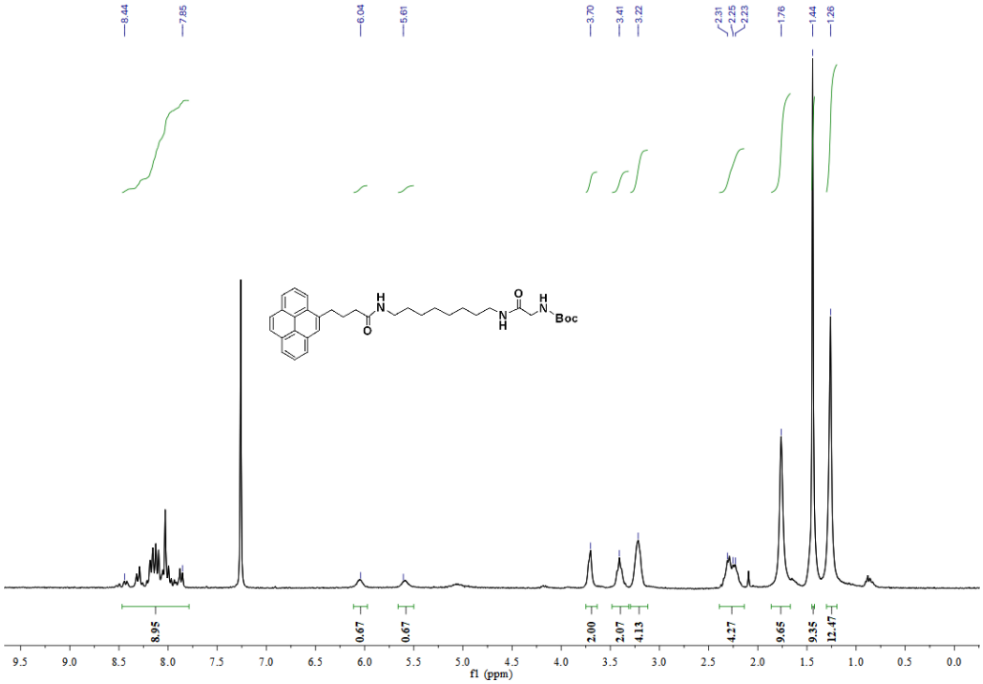

Figure A21. ^{1}H NMR spectrum of **C27**.

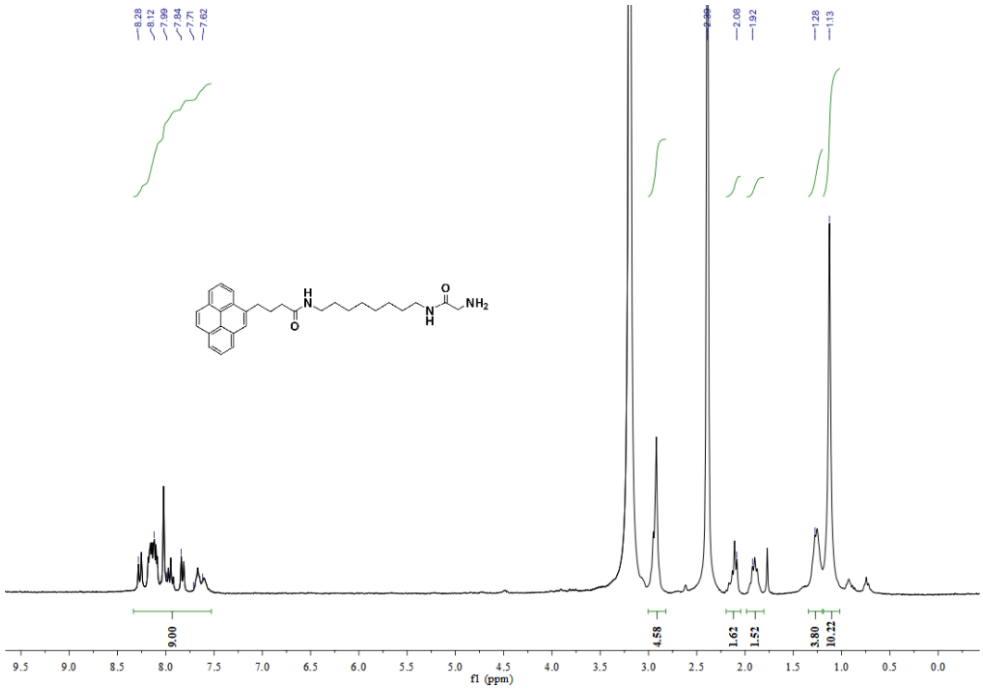

Figure A22. ^{1}H NMR spectrum of **C28** (Indicator 2).

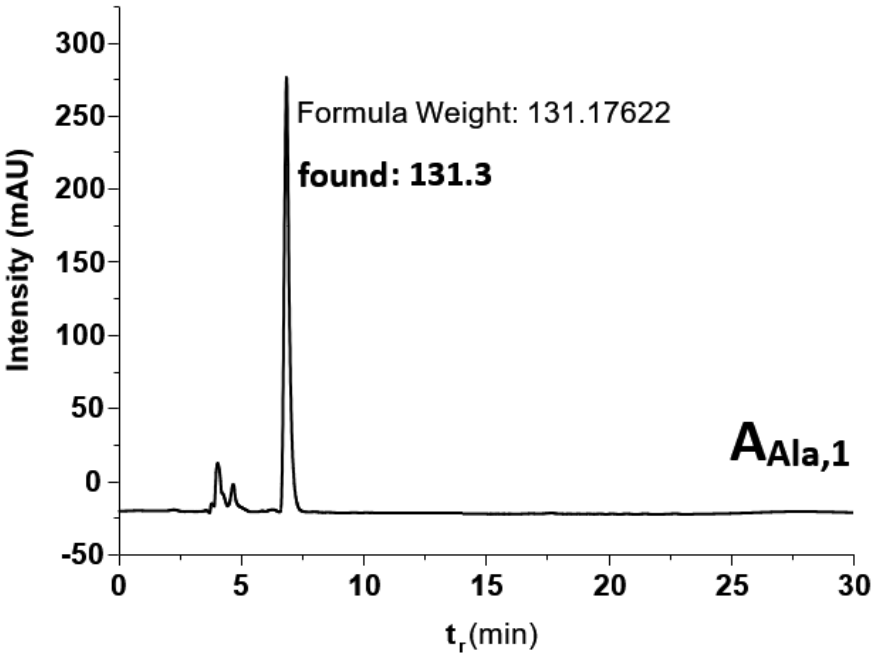

Figure A23. HPLC-MS chromatograms of the $\mathbf{A_{Ala,1}}$.

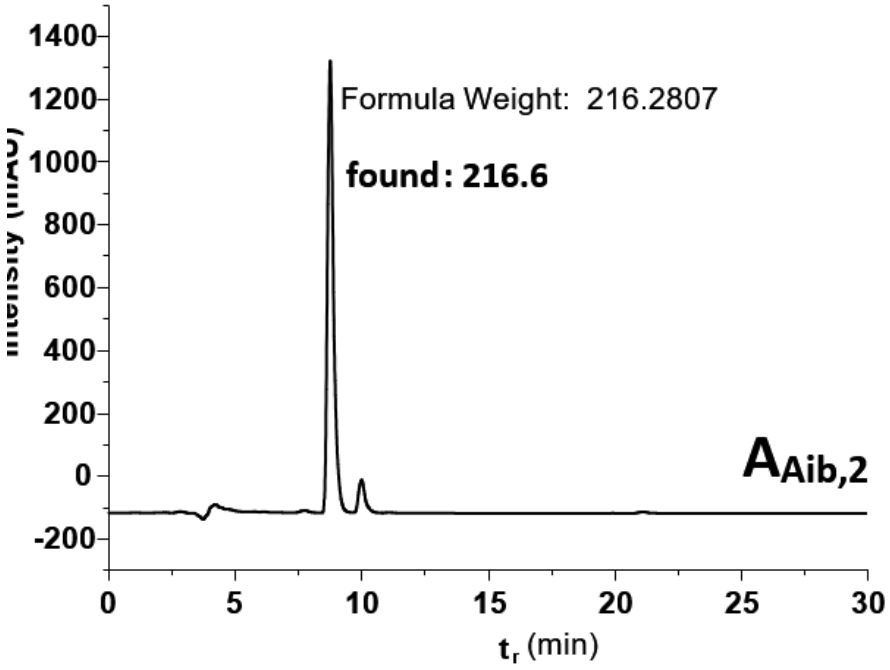

Figure A24. HPLC-MS chromatograms of the $\mathbf{A_{Aib,2}}$.

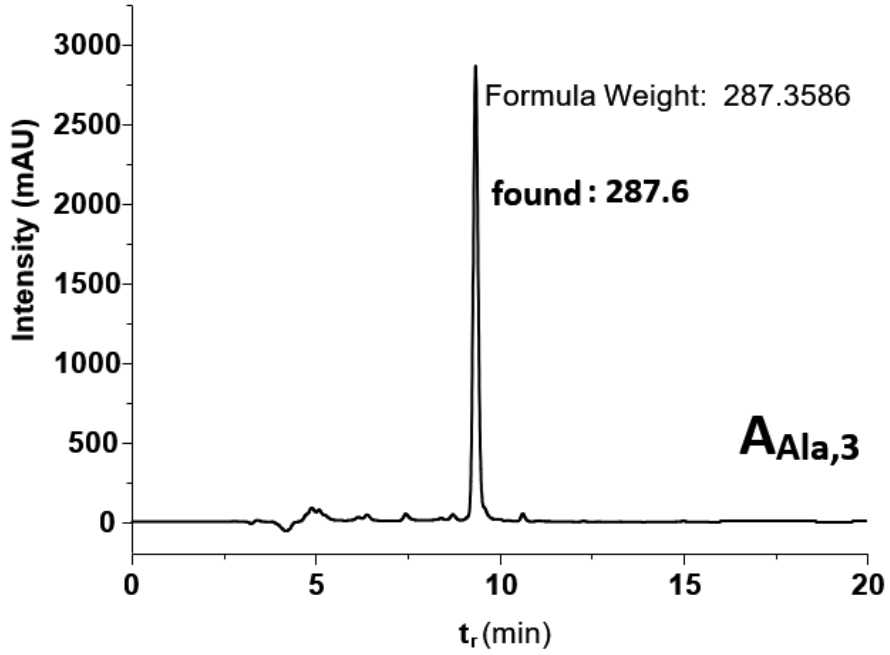

Figure A25. HPLC-MS chromatograms of the $\mathbf{A_{Ala,3}}$.

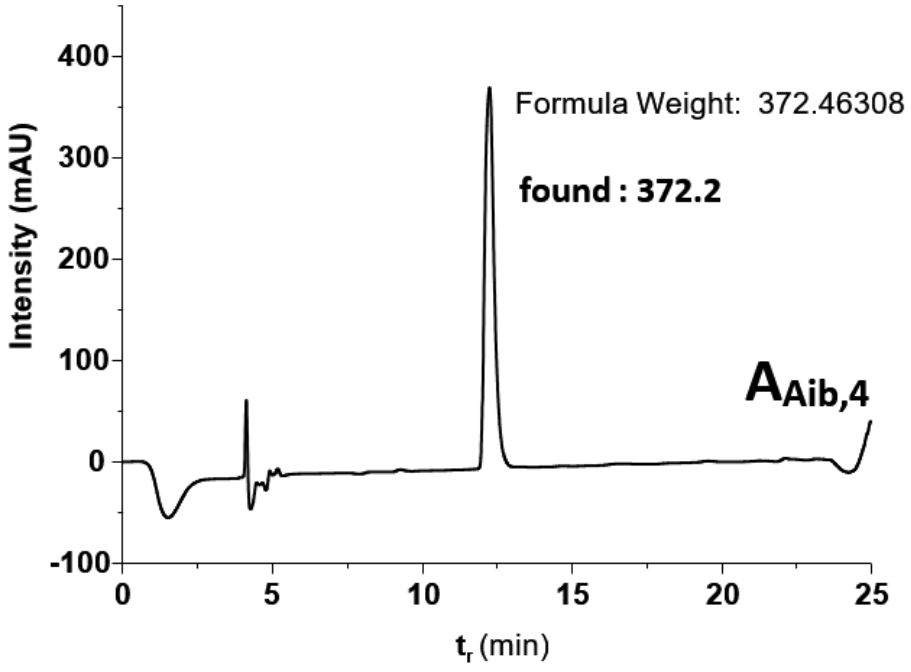

Figure A26. HPLC-MS chromatograms of the $\mathbf{A_{Aib,4}}$.

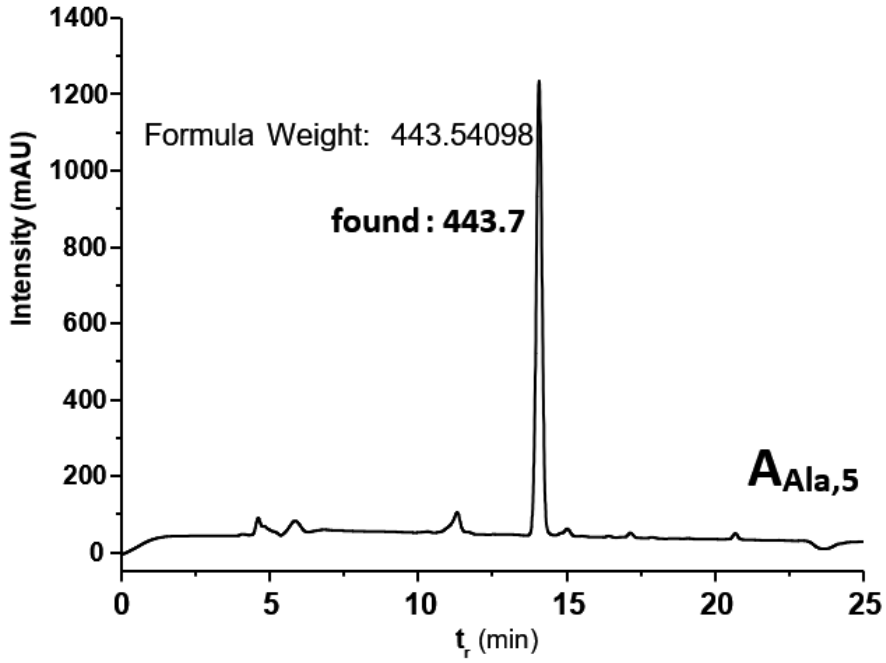

Figure A27. HPLC-MS chromatograms of the $\mathbf{A_{Ala,5}}$.

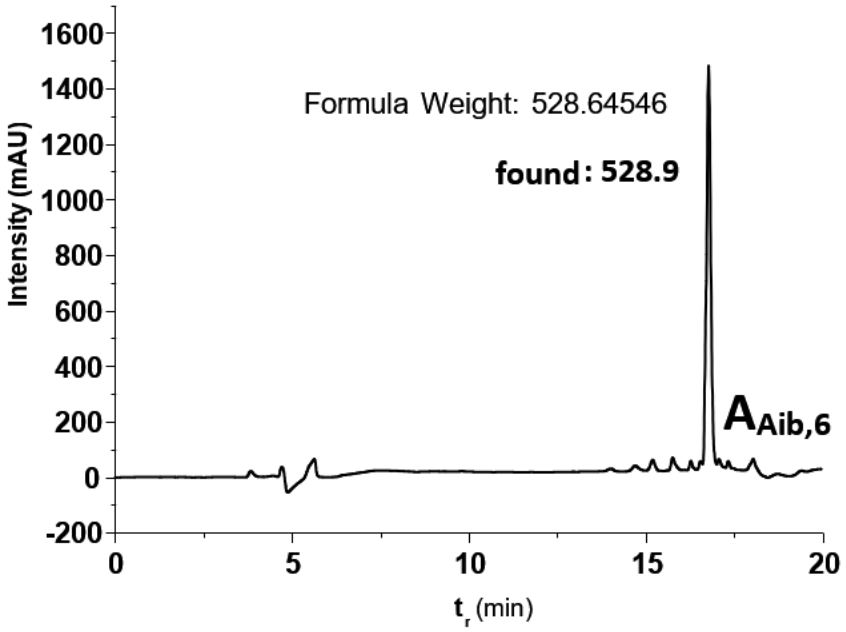

Figure A28. HPLC-MS chromatograms of the $\mathbf{A_{Aib,6}}$.

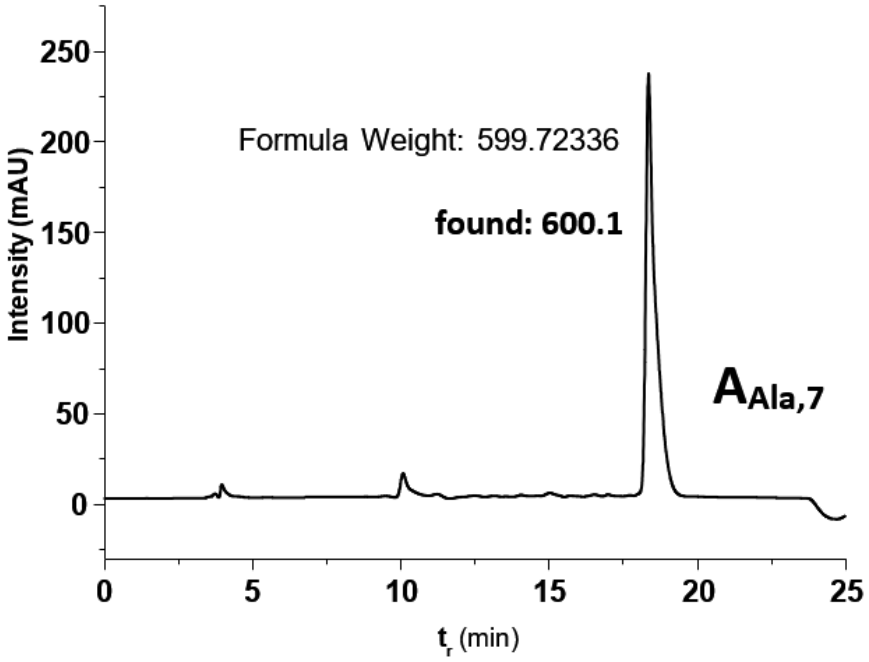

Figure A29. HPLC-MS chromatograms of the $\mathbf{A_{Ala,7}}$.

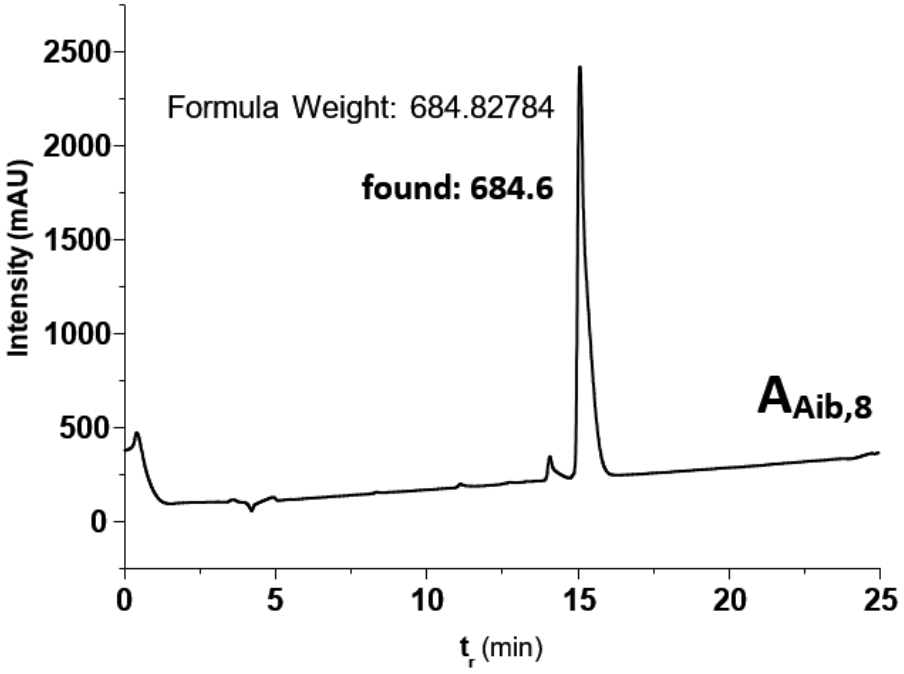

Figure A30. HPLC-MS chromatograms of the $\mathbf{A_{Aib,8}}$.

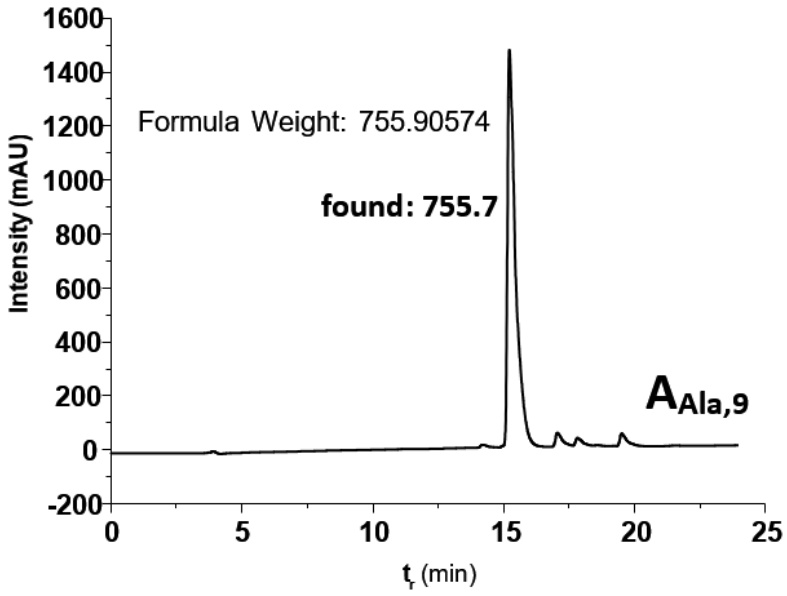

Figure A31. HPLC-MS chromatograms of the $\mathbf{A_{Ala,9}}$.

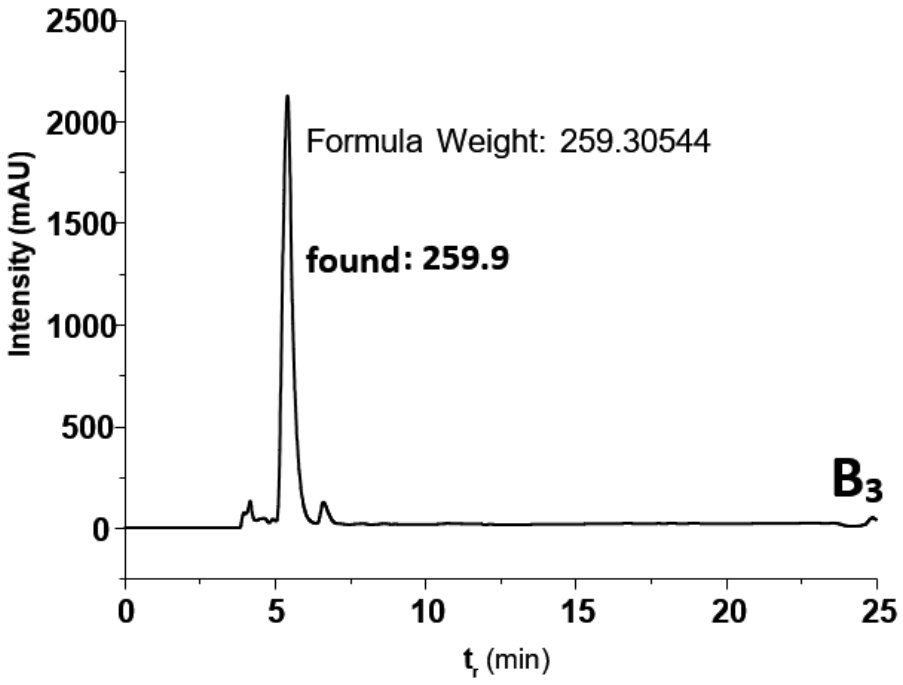

Figure A32. HPLC-MS chromatograms of the $\mathbf{B_3}$.

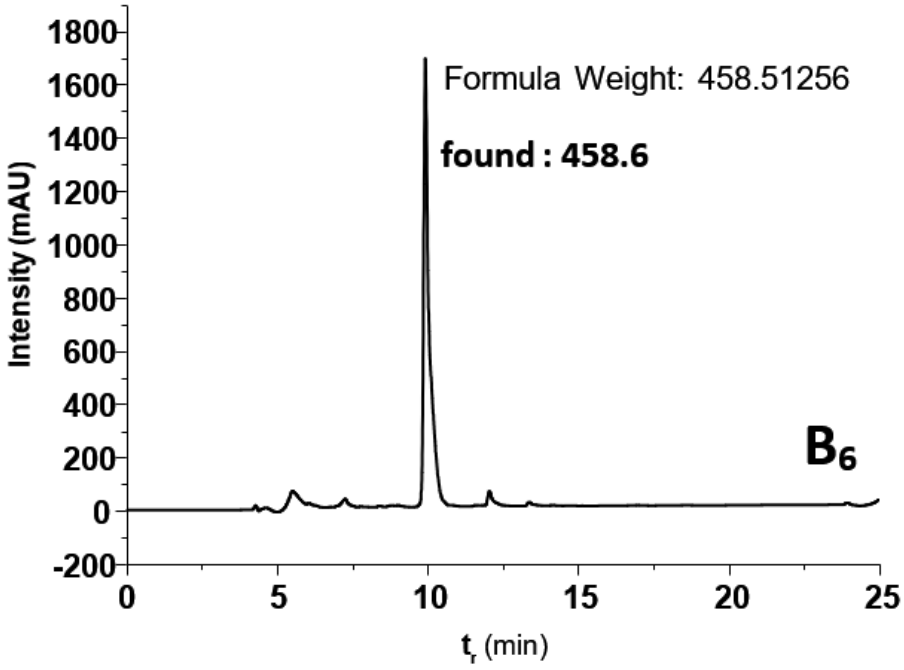

Figure A33. HPLC-MS chromatograms of the **B6**.

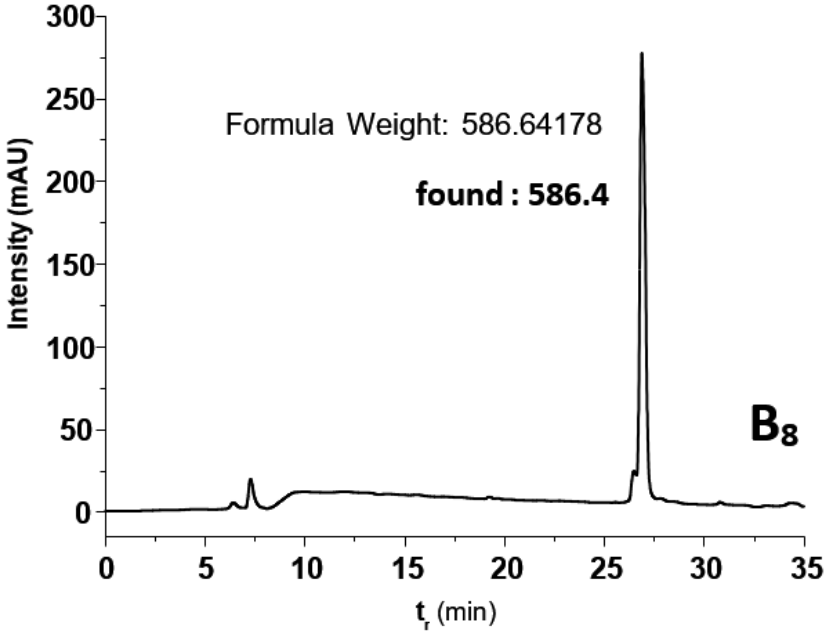

Figure A34. HPLC-MS chromatograms of the **B8**.

References

1. S. K. Ghosh and T. Pal, *Chem. Rev.*, **2007**, 107, 4797-4862.
2. K. Saha, S. S. Agasti, C. Kim, X. N. Li and V. M. Rotello, *Chem. Rev.*, **2012**, 112, 2739-2779.
3. M. C. Daniel and D. Astruc, *Chem. Rev.*, **2004**, 104, 293-346.
4. S. Eustis and M. A. El-Sayed, *Chem. Soc. Rev.*, **2006**, 35, 209-217.
5. C. Burda, X. B. Chen, R. Narayanan and M. A. El-Sayed, *Chem. Rev.*, **2005**, 105, 1025-1102.
6. L. M. Liz-Marzan, *Langmuir*, **2006**, 22, 32-41.
7. A. Heuer-Jungemann, N. Feliu, I. Bakaimi, M. Hamaly, A. Alkilany, I. Chakraborty, A. Masood, M. F. Casula, A. Kostopoulou, E. Oh, K. Susumu, M. H. Stewart, I. L. Medintz, E. Stratakis, W. J. Parak and A. G. Kanaras, *Chem. Rev.*, **2019**, 119, 4819-4880.
8. C. M. Cobley, J. Y. Chen, E. C. Cho, L. V. Wang and Y. N. Xia, *Chem. Soc. Rev.*, **2011**, 40, 44-56.
9. E. C. Dreaden, A. M. Alkilany, X. H. Huang, C. J. Murphy and M. A. El-Sayed, *Chem. Soc. Rev.*, **2012**, 41, 2740-2779.
10. A. Kyrychenko, G. V. Karpushina, D. Syechkarev, D. Kolodezny, S. I. Bogatyrenko, A. P. Kryshtal and A. O. Doroshenko, *J. Phys. Chem. C*, **2012**, 116, 21059-21068.
11. C. W. Chu, J. S. Na and G. N. Parsons, *J. Am. Chem. Soc.*, **2007**, 129, 2287-2296.
12. K. H. Su, Q. H. Wei, X. Zhang, J. J. Mock, D. R. Smith and S. Schultz, *Nano Lett.*, **2003**, 3, 1087-1090.
13. P. C. S. John Turkevhich, James Hillier, *Discussions of the Faraday Society*, **1951**, 11, 55-75.
14. P. C. S. John Turkevich, J. Hillier, *J. Phys. Chem.*, **1953**, 57, 670-673.
15. M. Wuithschick, A. Birnbaum, S. Witte, M. Sztucki, U. Vainio, N. Pinna, K. Rademann, F. Emmerling, R. Kraehnert and J. Polte, *ACS Nano*, **2015**, 9, 7052-7071.
16. G. Frens, *Nature Physical Science*, **1973**, 241, 20-22.
17. F. Kettemann, A. Birnbaum, S. Witte, M. Wuithschick, N. Pinna, R. Kraehnert, K. Rademann and J. Polte, *Chem. Mater.*, **2016**, 28, 4072-4081.
18. H. B. Xia, S. O. Bai, J. Hartmann and D. Y. Wang, *Langmuir*, **2010**, 26, 3585-3589.
19. H. B. Xia, Y. J. Xiahou, P. N. Zhang, W. C. Ding and D. Y. Wang, *Langmuir*, **2016**, 32, 5870-5880.
20. N. E. Larm, J. B. Essner, K. Pokpas, J. A. Canon, N. Jahed, E. I. Iwuoha and G. A. Baker, *J. Phys. Chem. C*, **2018**, 122, 5105-5118.
21. M. Brust, M. Walker, D. Bethell, D. J. Schiffrin and R. Whyman, *Journal of the Chemical Society-Chemical Communications*, **1994**, DOI: 10.1039/c39940000801, 801-802.
22. R. Sardar, A. M. Funston, P. Mulvaney and R. W. Murray, *Langmuir*, **2009**, 25, 13840-13851.
23. A. C. Templeton, M. P. Wuelfing and R. W. Murray, *Acc. Chem. Res.*, **2000**, 33, 27-36.
24. R. C. Jin, *Nanoscale*, **2010**, 2, 343-362.
25. Y. Negishi, Y. Takasugi, S. Sato, H. Yao, K. Kimura and T. Tsukuda, *J. Phys. Chem. B*, **2006**, 110, 12218-12221.
26. S. R. K. Perala and S. Kumar, *Langmuir*, **2013**, 29, 14756-14762.

27. Y. Li, O. Zaluzhna, B. L. Xu, Y. Gao, J. M. Modest and Y. Y. J. Tong, *J. Am. Chem. Soc.*, **2012**, 134, 6498-6498.
28. P. J. G. Goulet and R. B. Lennox, *J. Am. Chem. Soc.*, **2010**, 132, 9582-9584.
29. M. P. Rowe, K. E. Plass, K. Kim, C. Kurdak, E. T. Zellers and A. J. Matzger, *Chem. Mater.*, **2004**, 16, 3513-3517.
30. O. Zaluzhna, Y. Li, C. Zangmeister, T. C. Allison and Y. J. Tong, *Chem. Commun.*, **2012**, 48, 362-364.
31. F. Manea, C. Bindoli, S. Polizzi, L. Lay and P. Scrimin, *Langmuir*, **2008**, 24, 4120-4124.
32. M. Faraday, *Philos. Trans. R. Soc. London, Ser. A*, **1857**, 147, 145-181.
33. G. Mie, *Ann. Phys.*, **1908**, 330, 377-445.
34. X. H. Huang, S. Neretina and M. A. El-Sayed, *Adv. Mater.*, **2009**, 21, 4880-4910.
35. R. H. Ritchie, *Current Contents/Engineering Technology & Applied Sciences*, **1985**, 18-18.
36. P. K. Jain, X. H. Huang, I. H. El-Sayed and M. A. El-Sayed, *Acc. Chem. Res.*, **2008**, 41, 1578-1586.
37. J. N. Anker, W. P. Hall, O. Lyandres, N. C. Shah, J. Zhao and R. P. Van Duyne, *Nat. Mater.*, **2008**, 7, 442-453.
38. S. Peiris, J. McMurtrie and H. Y. Zhu, *Catalysis Science & Technology*, **2016**, 6, 320-338.
39. K. L. Kelly, E. Coronado, L. L. Zhao and G. C. Schatz, *J. Phys. Chem. B*, **2003**, 107, 668-677.
40. K. S. Lee and M. A. El-Sayed, *J. Phys. Chem. B*, **2006**, 110, 19220-19225.
41. I. Zoric, M. Zach, B. Kasemo and C. Langhammer, *ACS Nano*, **2011**, 5, 2535-2546.
42. K. Sokolowska, E. Hulkko, L. Lehtovaara and T. Lahtinen, *J. Phys. Chem. C*, **2018**, 122, 12524-12533.
43. S. Mann, W. Shenton, M. Li, S. Connolly and D. Fitzmaurice, *Adv. Mater.*, **2000**, 12, 147-150.
44. N. L. Rosi and C. A. Mirkin, *Chem. Rev.*, **2005**, 105, 1547-1562.
45. V. Chegel, O. Rachkov, A. Lopatynskyi, S. Ishihara, I. Yanchuk, Y. Nemoto, J. P. Hill and K. Ariga, *J. Phys. Chem. C*, **2012**, 116, 2683-2690.
46. Z. Y. Zhong, S. Patskovskyy, P. Bouvrette, J. H. T. Luong and A. Gedanken, *J. Phys. Chem. B*, **2004**, 108, 4046-4052.
47. M. S. Han, A. K. R. Lytton-Jean, B. K. Oh, J. Heo and C. A. Mirkin, *Angew. Chem., Int. Ed.*, **2006**, 45, 1807-1810.
48. A. G. Brolo, *Nat. Photonics*, **2012**, 6, 709-713.
49. H. K. Hunt and A. M. Armani, *Nanoscale*, **2010**, 2, 1544-1559.
50. A. Kapur, F. Aldeek, X. Ji, M. Safi, W. T. Wang, A. Del Cid, O. Steinbock and H. Mattoussi, *Bioconjugate Chem.*, **2017**, 28, 678-687.
51. P. K. Jain, I. H. El-Sayed and M. A. El-Sayed, *Nano Today*, **2007**, 2, 18-29.
52. C. C. Huang and H. T. Chang, *Anal. Chem.*, **2006**, 78, 8332-8338.
53. C. S. Yun, A. Javier, T. Jennings, M. Fisher, S. Hira, S. Peterson, B. Hopkins, N. O. Reich and G. F. Strouse, *J. Am. Chem. Soc.*, **2005**, 127, 3115-3119.
54. S. Y. Lim, J. H. Kim, J. S. Lee and C. B. Park, *Langmuir*, **2009**, 25, 13302-13305.

55. P. V. Kamat, S. Barazzouk and S. Hotchandani, *Angew. Chem., Int. Ed.*, **2002**, 41, 2764.
56. K. G. Thomas and P. V. Kamat, *Acc. Chem. Res.*, **2003**, 36, 888-898.
57. L. You, D. J. Zha and E. V. Anslyn, *Chem. Rev.*, **2015**, 115, 7840-7892.
58. B. T. Nguyen and E. V. Anslyn, *Coord. Chem. Rev.*, **2006**, 250, 3118-3127.
59. K. Das, S. Sarkar and P. K. Das, *ACS Appl. Mater. Interfaces*, **2016**, 8, 25691-25701.
60. D. B. Liu, S. J. Wang, M. Swierczewska, X. L. Huang, A. A. Bhirde, J. S. Sun, Z. Wang, M. Yang, X. Y. Jiang and X. Y. Chen, *ACS Nano*, **2012**, 6, 10999-11008.
61. A. P. Umali, E. V. Anslyn, A. T. Wright, C. R. Blieden, C. K. Smith, T. A. Tian, J. A. Truong, C. E. Crumm, J. E. Garcia, S. Lee, M. Mosier and C. P. Nguyen, *J. Chem. Educ.*, **2010**, 87, 832-835.
62. L. H. Guo, Y. Xu, A. R. Ferhan, G. N. Chen and D. H. Kim, *J. Am. Chem. Soc.*, **2013**, 135, 12338-12345.
63. H. P. Jiao, J. Chen, W. Y. Li, F. Y. Wang, H. P. Zhou, Y. X. Li and C. Yu, *ACS Appl. Mater. Interfaces.*, **2014**, 6, 1979-1985.
64. A. T. Liu and J. M. Berlin, *Langmuir*, **2017**, 33, 14358-14365.
65. A. Abbas, R. Kattumenu, L. M. Tian and S. Singamaneni, *Langmuir*, **2013**, 29, 56-64.
66. V. S. Godakhindi, P. Y. Kang, M. Serre, N. A. Revuru, J. M. H. Zou, M. R. Roner, R. Levitz, J. S. Kahn, J. Randrianalisoa and Z. P. Qin, *Acs Sensors*, **2017**, 2, 1627-1636.
67. A. Martinez and P. Scrimin, *Biopolymers*, **2018**, 109.
68. L. Guerrini and D. Graham, *Chem. Soc. Rev.*, **2012**, 41, 7085-7107.
69. P. Hazarika, F. Kukolka and C. M. Niemeyer, *Angew. Chem., Int. Ed.*, **2006**, 45, 6827-6830.
70. K. Aslan, C. C. Luhrs and V. H. Perez-Luna, *J. Phys. Chem. B*, **2004**, 108, 15631-15639.
71. G. M. Whitesides and B. Grzybowski, *Science*, **2002**, 295, 2418-2421.
72. M. Grzelczak, J. Vermant, E. M. Furst and L. M. Liz-Marzan, *ACS Nano*, **2010**, 4, 3591-3605.
73. D. Luo, C. Yan and T. Wang, *Small*, **2015**, 11, 5984-6008.
74. M. A. Boles, M. Engel and D. V. Talapin, *Chem. Rev.*, **2016**, 116, 11220-11289.
75. H. Yao and S. Yaomura, *Langmuir*, **2013**, 29, 6444-6451.
76. W. Huang, G. Masuda, S. Maeda, H. Tanaka and T. Ogawa, *Chem. Eur. J*, **2006**, 12, 607-619.
77. H. Hakkinen, *Nature Chem.*, **2012**, 4, 443-455.
78. M. Brust, D. Bethell, D. J. Schiffrin and C. J. Kiely, *Adv. Mater. (Weinheim, Ger.*, **1995**, 7, 795-&.
79. S. Nayak, N. Horst, H. H. Zhang, W. J. Wang, S. Mallapragada, A. Travesset and D. Vaknin, *Particle & Particle Systems Characterization*, **2018**, 35.
80. G. Zotti, B. Vercelli and A. Berlin, *Chem. Mater.*, **2008**, 20, 397-412.
81. A. C. Templeton, F. P. Zamborini, W. P. Wuelfing and R. W. Murray, *Langmuir*, **2000**, 16, 6682-6688.
82. J. M. de la Fuente, A. G. Barrientos, T. C. Rojas, J. Rojo, J. Canada, A. Fernandez and S. Penades, *Angew. Chem., Int. Ed.*, **2001**, 40, 2258.
83. C. Guarise, L. Pasquato and P. Scrimin, *Langmuir*, **2005**, 21, 5537-5541.

84. C. Guarise, L. Pasquato, V. De Filippis and P. Scrimin, *Proc. Natl. Acad. Sci. U. S. A.*, **2006**, 103, 3978-3982.
85. A. Laromaine, L. L. Koh, M. Murugesan, R. V. Ulijn and M. M. Stevens, *J. Am. Chem. Soc.*, **2007**, 129, 4156.
86. N. Seiler, J. G. Delcros and J. P. Moulinoux, *Int. J. Biochem. Cell Biol.*, **1996**, 28, 843-861.
87. H. M. Zakaria, A. Shah, M. Konieczny, J. A. Hoffmann, A. J. Nijdam and M. E. Reeves, *Langmuir*, **2013**, 29, 7661-7673.
88. S. Mandal, S. Phadtare and M. Sastry, *Current Applied Physics*, **2005**, 5, 118-127.
89. P. R. Selvakannan, P. S. Kumar, A. S. More, R. D. Shingte, P. P. Wadgaonkar and M. Sastry, *Langmuir*, **2004**, 20, 295-298.
90. D. V. Leff, L. Brandt and J. R. Heath, *Langmuir*, **1996**, 12, 4723-4730.
91. N. Jornet-Martinez, M. Gonzalez-Bejar, Y. Moliner-Martinez, P. Campins-Falco and J. Perez-Prieto, *Anal. Chem.*, **2014**, 86, 1347-1351.
92. H. Y. Huang, W. F. Chen and P. L. Kuo, *J. Phys. Chem. B*, **2005**, 109, 24288-24294.
93. D. Aili, K. Enander, L. Baltzer and B. Liedberg, *Nano Lett.*, **2008**, 8, 2473-2478.
94. L. Xu, Y. Guo, R. G. Xie, J. Q. Zhuang, W. S. Yang and T. J. Li, *Nanotechnology*, **2002**, 13, 725-728.
95. M. Nilam, A. Hennig, W. M. Nau and K. I. Assaf, *Anal. Methods,*, **2017**, 9, 2784-2787.
96. H. H. Deng, X. Q. Shi, H. P. Peng, Q. Q. Zhuang, Y. Yang, A. L. Liu, X. H. Xia and W. Chen, *ACS Appl. Mater. Interfaces*, **2018**, 10, 5358-5364.
97. P. K. Harimech, S. R. Gerrard, A. H. El-Sagheer, T. Brown and A. G. Kanaras, *J. Am. Chem. Soc.*, **2015**, 137, 9242-9245.
98. B. P. Wu, F. Zou, X. X. Wang, K. Koh, K. M. Wang and H. X. Chen, *Anal. Methods,*, **2017**, 9, 2153-2158.
99. Y. Chen, L. Chen, Y. Wu and J. W. Di, *Microchem. J.*, **2019**, 147, 955-961.
100. H. C. Su, B. Sun, L. J. Chen, Z. N. Xu and S. Y. Ai, *Anal. Methods,*, **2012**, 4, 3981-3986.
101. A. Kassam, G. Bremner, B. Clark, G. Ulibarri and R. B. Lennox, *J. Am. Chem. Soc.*, **2006**, 128, 3476-3477.
102. M. Mahmoudi, I. Lynch, M. R. Ejtehadi, M. P. Monopoli, F. B. Bombelli and S. Laurent, *Chem. Rev.*, **2011**, 111, 5610-5637.
103. R. Guo, Y. Song, G. L. Wang and R. W. Murray, *J. Am. Chem. Soc.*, **2005**, 127, 2752-2757.
104. R. L. Donkers, Y. Song and R. W. Murray, *Langmuir*, **2004**, 20, 4703-4707.
105. M. J. Hostetler, A. C. Templeton and R. W. Murray, *Langmuir*, **1999**, 15, 3782-3789.
106. A. Caragheorgheopol and V. Chechik, *Phys. Chem. Chem. Phys.*, **2008**, 10, 5029-5041.
107. Y. C. Yeh, B. Creran and V. M. Rotello, *Nanoscale*, **2012**, 4, 1871-1880.
108. M. Montalti, L. Prodi, N. Zaccheroni, R. Baxter, G. Teobaldi and F. Zerbetto, *Langmuir*, **2003**, 19, 5172-5174.
109. S. Perumal, A. Hofmann, N. Scholz, E. Ruhl and C. Graf, *Langmuir*, **2011**, 27, 4456-4464.

110. P. Ionita, A. Caragheorgheopol, B. C. Gilbert and V. Chechik, *J. Am. Chem. Soc.*, **2002**, 124, 9048-9049.
111. O. Vilanova, J. J. Mittag, P. M. Kelly, S. Milani, K. A. Dawson, J. O. Radler and G. Franzese, *ACS Nano*, **2016**, 10, 10842-10850.
112. Y. K. Duan, Y. Liu, W. Shen and W. W. Zhong, *Anal. Chem.*, **2017**, 89, 12160-12167.
113. S. H. D. Lacerda, J. J. Park, C. Meuse, D. Pristinski, M. L. Becker, A. Karim and J. F. Douglas, *ACS Nano*, **2010**, 4, 365-379.
114. L. W. Li, Q. X. Mu, B. Zhang and B. Yan, *Analyst*, **2010**, 135, 1519-1530.
115. X. N. Zhang, J. T. Zhang, F. Zhang and S. N. Yu, *Nanoscale*, **2017**, 9, 4787-4792.
116. O. R. Miranda, H. T. Chen, C. C. You, D. E. Mortenson, X. C. Yang, U. H. F. Bunz and V. M. Rotello, *J. Am. Chem. Soc.*, **2010**, 132, 5285-5289.
117. M. Zheng and X. Y. Huang, *J. Am. Chem. Soc.*, **2004**, 126, 12047-12054.
118. G. C. Adam, E. J. Sorensen and B. F. Cravatt, *Mol. Cell. Proteomics*, **2002**, 1, 781-790.
119. L. I. Willems, H. S. Overkleeft and S. I. van Kasteren, *Bioconjugate Chem.*, **2014**, 25, 1181-1191.
120. A. W. Scott, V. Garimella, C. M. Calabrese and C. A. Mirkin, *Bioconjugate Chem.*, **2017**, 28, 203-211.
121. A. Gupta, D. F. Moyano, A. Parnsubsakul, A. Papadopoulos, L. S. Wang, R. F. Landis, R. Das and V. M. Rotello, *ACS Appl. Mater. Interfaces*, **2016**, 8, 14096-14101.
122. I. Olmedo, E. Araya, F. Sanz, E. Medina, J. Arbiol, P. Toledo, A. Alvarez-Lueje, E. Giralt and M. J. Kogan, *Bioconjugate Chem.*, **2008**, 19, 1154-1163.
123. M. De, S. Rana, H. Akpinar, O. R. Miranda, R. R. Arvizo, U. H. F. Bunz and V. M. Rotello, *Nature Chem.*, **2009**, 1, 461-465.
124. H. Al-Johani, E. Abou-Hamad, A. Jedidi, C. M. Widdifield, J. Viger-Gravel, S. S. Sangaru, D. Gajan, D. H. Anjum, S. Ould-Chikh, M. N. Hedhili, A. Gurinov, M. J. Kelly, M. El Eter, L. Cavallo, L. Emsley and J. M. Basset, *Nature Chem.*, **2017**, 9, 890-895.
125. X. G. Han, J. Goebl, Z. D. Lu and Y. D. Yin, *Langmuir*, **2011**, 27, 5282-5289.
126. L. A. K. V. E. Bel'skii, K. A. Derstuganova, A. B. Teitel'baum, B. E. Ivanov, *Russ Chem Bull.*, **1981**, 30, 736-738.
127. J. A. Olmos-Asar, M. Luduena and M. M. Mariscal, *Phys. Chem. Chem. Phys.*, **2014**, 16, 15979-15987.
128. E. Pensa, E. Cortes, G. Corthey, P. Carro, C. Vericat, M. H. Fonticelli, G. Benitez, A. A. Rubert and R. C. Salvarezza, *Acc. Chem. Res.*, **2012**, 45, 1183-1192.
129. A. Hofmann, P. Schmiel, B. Stein and C. Graf, *Langmuir*, **2011**, 27, 15165-15175.
130. P. D. Howes, R. Chandrawati and M. M. Stevens, *Science*, **2014**, 346, 53.
131. M. Doyen, J. Goole, K. Bartik and G. Bruylants, *J. Colloid Interface Sci.*, **2016**, 464, 160-166.
132. M. Sethi and M. R. Knecht, *ACS Appl. Mater. Interfaces*, **2009**, 1, 1270-1278.
133. J. M. Scholtz and R. L. Baldwin, *Annu. Rev. Biophys. Biomol. Struct.*, **1992**, 21, 95-118.

134. P. Pengo, L. Pasquato, S. Moro, A. Brigo, F. Fogolari, Q. B. Broxterman, B. Kaptein and P. Scrimin, *Angew. Chem., Int. Ed.*, **2003**, 42, 3388-3392.
135. M. Bellanda, S. Mammi, S. Geremia, N. Demitri, L. Randaccio, Q. B. Broxterman, B. Kaptein, P. Pengo, L. Pasquato and P. Scrimin, *Chem. Eur. J*, **2007**, 13, 407-416.
136. T. Burgi, *Nanoscale*, **2015**, 7, 15553-15567.
137. G. L. Millhauser, *Biochemistry*, **1995**, 34, 3873-3877.
138. J. Venkatraman, S. C. Shankaramma and P. Balaram, *Chem. Rev.*, **2001**, 101, 3131-3152.
139. E. Longo, A. Moretto, F. Formaggio and C. Toniolo, *Chirality*, **2011**, 23, 756-760.
140. I. Maffucci, S. Pellegrino, J. Clayden and A. Contini, *J. Phys. Chem. B*, **2015**, 119, 1350-1361.
141. E. Longo, A. Orlandin, F. Mancin, P. Scrimin and A. Moretto, *ACS Nano*, **2013**, 7, 9933-9939.
142. I. Hussain, Z. X. Wang, A. I. Cooper and M. Brust, *Langmuir*, **2006**, 22, 2938-2941.
143. D. Van Haute, J. M. Longmate and J. M. Berlin, *Adv. Mater.*, **2015**, 27, 5158-5164.
144. F. della Sala and E. R. Kay, *Angew. Chem., Int. Ed.*, **2015**, 54, 4187-4191.
145. J. D. Augspurger, V. A. Bindra, H. A. Scheraga and A. Kuki, *Biochemistry*, **1995**, 34, 2566-2576.
146. C. Toniolo, A. Polese, F. Formaggio, M. Crisma and J. Kamphuis, *J. Am. Chem. Soc.*, **1996**, 118, 2744-2745.
147. F. Formaggio, M. Crisma, P. Rossi, P. Scrimin, B. Kaptein, Q. B. Broxterman, J. Kamphuis and C. Toniolo, *Chem. Eur. J*, **2000**, 6, 4498-4504.
148. C. Toniolo, F. Formaggio, S. Tognon, Q. B. Broxterman, B. Kaptein, R. Huang, V. Setnicka, T. A. Keiderling, I. H. McColl, L. Hecht and L. D. Barron, *Biopolymers*, **2004**, 75, 32-45.
149. F. Formaggio, C. Peggion, M. Crisma, B. Kaptein, Q. B. Broxterman, J. P. Mazaleyrat, M. Wakselman and C. Toniolo, *Chirality*, **2004**, 16, 388-397.
150. C. Zhang, J. H. Lu, F. L. Tian, L. D. Li, Y. Q. Hou, Y. Y. Wang, L. D. Sun, X. H. Shi and H. Lu, *Nano Research*, **2019**, 12, 889-896.
151. A. Verma, H. Nakade, J. M. Simard and V. M. Rotello, *J. Am. Chem. Soc.*, **2004**, 126, 10806-10807.
152. M. G. Ryadnov, B. Ceyhan, C. M. Niemeyer and D. N. Woolfson, *J. Am. Chem. Soc.*, **2003**, 125, 9388-9394.
153. M. M. Stevens, N. T. Flynn, C. Wang, D. A. Tirrell and R. Langer, *Adv. Mater.*, **2004**, 16, 915-918.
154. D. Aili, K. Enander, J. Rydberg, I. Lundstrom, L. Baltzer and B. Liedberg, *J. Am. Chem. Soc.*, **2006**, 128, 2194-2195.
155. R. Chandrawati and M. M. Stevens, *Chem. Commun. (Cambridge, U. K.)*, **2014**, 50, 5431-5434.
156. C. D'Andrea, B. Fazio, P. G. Gucciardi, M. C. Giordano, C. Martella, D. Chiappe, A. Toma, F. B. de Mongeot, F. Tantussi, P. Vasanthakumar, F. Fuso and M. Allegrini, *J. Phys. Chem. C*, **2014**, 118, 8571-8580.
157. A. Poletti, G. Fracasso, G. Conti, R. Pilot and V. Amendola, *Nanoscale*, **2015**, 7, 13702-13714.
158. T. H. Chen, M. Pourmand, A. Feizpour, B. Cushman and B. M. Reinhard, *Journal of Physical Chemistry Letters*, **2013**, 4, 2147-2152.

159. C. Ciraci, R. T. Hill, J. J. Mock, Y. Urzhumov, A. I. Fernandez-Dominguez, S. A. Maier, J. B. Pendry, A. Chilkoti and D. R. Smith, *Science*, **2012**, 337, 1072-1074.

160. J. Perez-Juste, I. Pastoriza-Santos, L. M. Liz-Marzan and P. Mulvaney, *Coord. Chem. Rev.*, **2005**, 249, 1870-1901.

161. L. J. E. Anderson, C. M. Payne, Y. R. Zhen, P. Nordlander and J. H. Hafner, *Nano Lett.*, **2011**, 11, 5034-5037.

162. X. Hong, C. L. Tan, J. Z. Chen, Z. C. Xu and H. Zhang, *Nano Research*, **2015**, 8, 40-55.

163. N. Pazos-Perez, D. Baranov, S. Irsen, M. Hilgendorff, L. M. Liz-Marzan and M. Giersig, *Langmuir*, **2008**, 24, 9855-9860.

164. C. Zhu, H. C. Peng, J. Zeng, J. Y. Liu, Z. Z. Gu and Y. N. Xia, *J. Am. Chem. Soc.*, **2012**, 134, 20234-20237.

165. S. T. Kim, K. Saha, C. Kim and V. M. Rotello, *Acc. Chem. Res.*, **2013**, 46, 681-691.

166. W. J. Luo, C. F. Zhu, S. Su, D. Li, Y. He, Q. Huang and C. H. Fan, *ACS Nano*, **2010**, 4, 7451-7458.

167. F. Zhang, Y. Zhou, Y. Chen, Z. W. Shi, Y. W. Tang and T. H. Lu, *J. Colloid Interface Sci.*, **2010**, 351, 421-426.

168. M. Comotti, C. Della Pina, R. Matarrese and M. Rossi, *Angew. Chem., Int. Ed.*, **2004**, 43, 5812-5815.

169. P. Beltrame, M. Comotti, C. Della Pina and M. Rossi, *Applied Catalysis a-General*, **2006**, 297, 1-7.

170. N. J. Lang, B. W. Liu and J. W. Liu, *J. Colloid Interface Sci.*, **2014**, 428, 78-83.

171. A. Dutta, S. Das, A. Paul and A. Chattopadhyay, *Journal of Nanoparticle Research*, **2015**, 17.

172. A. Dutta, A. Paul and A. Chattopadhyay, *Rsc Advances*, **2016**, 6, 82138-82149.

173. A. Kumar, S. Mandal, P. R. Selvakannan, R. Pasricha, A. B. Mandale and M. Sastry, *Langmuir*, **2003**, 19, 6277-6282.

174. M. J. Richardson, J. H. Johnston and T. Borrmann, *Eur. J. Inorg. Chem.*, **2006**, DOI: 10.1002/ejic.200600154, 2618-2623.

175. B. R. Panda and A. Chattopadhyay, *J. Nanosci. Nanotechnol.*, **2007**, 7, 1911-1915.

176. M. Zayats, R. Baron, I. Popov and I. Willner, *Nano Lett.*, **2005**, 5, 21-25.

177. B. Basnar, Y. Weizmann, Z. Cheglakov and I. Willner, *Adv. Mater. (Weinheim, Ger.)*, **2006**, 18, 713.

178. J. Polte, *CrystEngComm*, **2015**, 17, 6809-6830.

179. Y. Lu, J. Y. Huang, C. Wang, S. H. Sun and J. Lou, *Nat. Nanotechnol.*, **2010**, 5, 218-224.

180. Z. Y. Huo, C. K. Tsung, W. Y. Huang, X. F. Zhang and P. D. Yang, *Nano Lett.*, **2008**, 8, 2041-2044.

181. K. Liu, Y. H. Zheng, X. Lu, T. Thai, N. A. Lee, U. Bach and J. J. Gooding, *Langmuir*, **2015**, 31, 4973-4980.

182. C. K. Tsung, X. S. Kou, Q. H. Shi, J. P. Zhang, M. H. Yeung, J. F. Wang and G. D. Stucky, *J. Am. Chem. Soc.*, **2006**, 128, 5352-5353.

183. T. Dvir, B. P. Timko, M. D. Brigham, S. R. Naik, S. S. Karajanagi, O. Levy, H. W. Jin, K. K. Parker, R. Langer and D. S. Kohane, *Nat. Nanotechnol.*, **2011**, 6, 720-725.

184. N. N. Mahmoud, A. M. Alkilany, E. A. Khalil and A. G. Al-Bakri, *International Journal of Nanomedicine*, **2017**, 12, 7311-7322.
185. J. A. T. K. Strimbu, *Curr. Opin. HIV AIDS*, **2010**, 5, 463-466.
186. H. J. Issaq, Z. Xiao and T. D. Veenstra, *Chem. Rev.*, **2007**, 107, 3601-3620.
187. D. Leung, C. Hardouin, D. L. Boger and B. F. Cravatt, *Nat. Biotechnol.*, **2003**, 21, 687-691.
188. R. E. Moellering and B. F. Cravatt, *Chem. Biol.*, **2012**, 19, 11-22.
189. M. J. Evans and B. F. Cravatt, *Chem. Rev.*, **2006**, 106, 3279-3301.
190. B. F. C. A. E. Speers, *Curr Protoc Chem Biol.*, **2009**, 1, 29-41.
191. H. P. Erickson, *Biological Procedures Online*, **2009**, 11, 32-51.
192. U. Kreibig and L. Genzel, *Surf. Sci.*, **1985**, 156, 678-700.
193. K. Dano, N. Behrendt, G. Hoyer-Hansen, M. Johnsen, L. R. Lund, M. Ploug and J. Romer, *Thromb. Haemostasis*, **2005**, 93, 676-681.
194. M. Lee, R. Fridman and S. Mobashery, *Chem. Soc. Rev.*, **2004**, 33, 401-409.
195. M. J. Duffy, *Curr. Pharm. Des.*, **2004**, 10, 39-49.
196. R. L. Mackman, B. A. Katz, J. G. Breitenbucher, H. C. Hui, E. Verner, C. Luong, L. Liu and P. A. Sprengeler, *J. Med. Chem.*, **2001**, 44, 3856-3871.
197. T. W. Rockway, V. Nienaber and V. L. Giranda, *Curr. Pharm. Des.*, **2002**, 8, 2541-2558.
198. A. Schweinitz, T. Steinmetzer, I. J. Banke, M. J. E. Arlt, A. Sturzebecher, O. Schuster, A. Geissler, H. Giersiefen, E. Zeslawska, U. Jacob, A. Kruger and J. Sturzebecher, *J. Biol. Chem.*, **2004**, 279, 33613-33622.
199. J. Joossens, P. Van der Veken, G. Surpateanu, A. M. Lambeir, I. El-Sayed, O. M. Ali, K. Augustyns and A. Haemers, *J. Med. Chem.*, **2006**, 49, 5785-5793.
200. A. Belyaev, X. M. Zhang, K. Augustyns, A. M. Lambeir, I. De Meester, I. Vedernikova, S. Scharpe and A. Haemers, *J. Med. Chem.*, **1999**, 42, 1041-1052.
201. J. Oleksyszyn, B. Boduszek, C. M. Kam and J. C. Powers, *J. Med. Chem.*, **1994**, 37, 226-231.
202. K. Jiang, D. A. Smith and A. Pinchuk, *J. Phys. Chem. C*, **2013**, 117, 27073-27080.
203. W. Haiss, N. T. K. Thanh, J. Aveyard and D. G. Fernig, *Anal. Chem.*, **2007**, 79, 4215-4221.
204. D. V. Leff, P. C. Ohara, J. R. Heath and W. M. Gelbart, *J. Phys. Chem.*, **1995**, 99, 7036-7041.
205. P. Pengo, S. Polizzi, M. Battagliarin, L. Pasquato and P. Scrimin, *J. Mater. Chem.*, **2003**, 13, 2471-2478.